TÉCNICO LISBOA

Optical Neurostimulation Spine Endoprosthesis

Ricardo Morgado Marques

Thesis to obtain the Master of Science Degree in

Mechanical Engineering

Supervisors: Prof. Jorge Manuel Mateus Martins
Prof. Federico Herrera

Examination Committee

Chairperson: Prof. Paulo Jorge Coelho Ramalho Oliveira
Supervisor: Prof. Jorge Manuel Mateus Martins
Member of the Committee: Inv. Abel González Oliva
Prof. João Miguel Raposo Sanches

November 2019

To my parents,
without whom none of it would be possible.

Acknowledgments

I would first like to thank my supervisors Prof. Jorge Martins and Prof. Federico Herrera for the advice and guidance throughout this dissertation. I would like to thank Abel Oliva and Luís Marques for their time and precious expert support.

A special thanks to Ricardo, Fernanda and Cristina for being incredibly patient with me in the lab. Also, I would like to thank my colleagues from IST for the endless conversations, particularly to Rui for his neverending help, especially in troubled times.

Finally, I would like to express my very profound gratitude to my parents Lucília and Filipe for the unconditional support and for always having my back, at all moments. Thank you to the friends I met throughout these years for the good times we had. In particular, my housemates, who became a ”second family” to me.

And last but not least, to my lovely Ada. Thank you.

Resumo

A optogenética tem demonstrado potencial na satisfação de necessidades clínicas na esfera da medicina terapêutica e regenerativa. Embora, na última década, tenhamos assistido a um considerável progesso na área, possibilitando o controlo optogenético através de dispositivos implantáveis em ensaios *in vivo*, existe ainda uma enorme margem de melhoramento no que diz respeito a este tipo de aparelhos. Esta tese foca-se no devenvolvimento de uma endoprótese biomédica que, colocada na coluna vertebral, é capaz de provocar estimulação ótica em determinadas células alvo.

O dispositivo médico implatável provoca estimulação ótica através de canais LED e utiliza electrónica programável para controlar as propriedades da luz, tais como o comprimento de onda, potência luminosa e ciclo de pulsos. O aparelho apresentado é alimentado através de indução magnética e o seu sistema de transferência de energia, sem fios, foi projetado seguindo um processo de otimização. Tendo como o objectivo maximizar a eficiência do seu desempenho, foi possível obter um rendimento de 74.3% através de um fantoma de tecido corporal. Com o propósito de se observar alterações ao nível da fluorescência, foram executadas experiências *in vitro*. Tais observações tornaram possível concluir que uma irradiância de 3.33 mm/mW^2 é suficiente para atingir o nível máximo de fluorescência de uma dada célula, o que poderá implicar a sua capacidade máxima de gerar radicais de oxigénio. Várias estruturas de modelos paramétricos foram testadas, sendo possível concluir-se que um modelo de segunda ordem (com dois pólos e um zero) será o mais adequado para representar uma célula transfectada com miniSOG.

Os procedimentos utilizados neste trabalho funcionam como prova de conceito e representam um ponto de partida para desenvolvimento adicional de neuroestimuladores ópticos.

Palavras-chave: Optogenética, Neuroestimulação óptica, miniSOG, Medicina terapeutica e regenerativa, Dispositivo implantável

Abstract

Optogenetic technologies offer an innovative and promising approach for addressing unmet clinical needs in the sphere of therapeutic and regenerative medicine. Although major breakthroughs have been made on this technology during the last decade to enable optogenetic control in normal and disease states using implantable devices, there is much potential for further improvements concerning these tools. This thesis focuses on the development of a biomedical spine endoprosthesis capable to delivering optimized optical stimulation to optogenetically targeted cells.

The neurostimulation endoprosthesis performs optical cell stimulation through LED channels and relies on programmable electronics to control light properties, such as wavelength, power density and pulse cycle. The purposed device is powered through inductive energy transfer and its wireless power transfer system was designed following an optimization process. Aiming to maximize its performance, it was possible to reach an efficiency value of 74.3% through a body tissue phantom. In order to observe cell response to blue illumination, *In vitro* experiments with miniSOG-targeted cells were conducted. These observations revealed that a light power density $3.33mm/mW^2$ is sufficient to elevate the fluorescence level to its maximum value, which might imply its maximum capability of generating single oxygen. After testing a number of parametric model structures on the observed behaviour of a few cells upon blue illumination, a second order model suited the general miniSOG-targeted cell system satisfactorily.

The research and experiments performed in this work hold a ”proof-of-concept” utility and serve as starting point for further development of the presented technologies.

Keywords: Optogenetics, Optical Neurostimulation, miniSOG, Therapeutic and Regenerative Medicine, Implantable Device

Contents

List of Tables

List of Figures

Nomenclature

Acronyms

ADC	Analog Digital Converter
LED	Light Emitting Diode
ofMRI	Optogenetic Functional Magnetic resonance Imaging
PID	Proportional-Integral-Derivative
PNS	Peripheral Nervous System
PoC	Proof of Concept
PTE	Power Transfer Efficiency
PV	Process Variable
PWM	Pulse Width Modulation
SAR	Specific Absorption Rate
SISO	Single-Input-Single-Output
SMD	Surface Mounted Device
SP	Setpoint
VSD	Voltage-Sensitive Dye
WPT	Wireless Power Transfer

Greek Symbols

δ	Skin depth
μ	Permeability of free space
ω	Angular Frequency
ρ	Resistivity
σ	Conductivity

Roman Symbols

$\mathbf{C}$	Capacitance
$\mathbf{E_e}$	Irradiance
$\mathbf{I_e}$	Radiant Intensity
$\mathbf{I_v}$	Luminous Intensity
$\mathbf{k}$	Coupling Coefficient
$\mathbf{M}$	Mutual Inductance
$\mathbf{N}$	Number of Turns
$\mathbf{p}$	Pitch value
$\mathbf{Q}$	Quality Factor
$\mathbf{Rx}$	Receiver Coil
$\mathbf{Tx}$	Transmitter
$\mathbf{X_C}$	Reactance of Capacitor
$\mathbf{Z}$	Impedance

Chapter 1

Introduction

The peripheral nervous system (PNS) and spinal cord play a vital role in how information is communicated throughout the human body [1]. They branch out from the brain and extend to the various parts of the body, being responsible for transiting and gathering information. The spinal cord is responsible for the connection between the brain and the PNS, which includes sensory receptors that help in processing and reacting to changes in the internal and external environment, enabling us to feel sensations such as pain, hunger, temperature changes as well as to control muscles. Damage to the spinal cord and PNS resulting from trauma or disease often leads to debilitating neurological conditions which constitute an economical burden as well as personal and family suffering.

Optogenetics offers the possibility of optically controlling the activity of genetically specified cells [2], by combining light-sensitive proteins with controlled photo-stimulation. These proteins act as ion channels and pumps which can be genetically introduced into neurons, enabling the control of their activity on a millisecond time scale with high spatial resolution. The most common optogenetic proteins are called opsins, which are naturally found in some simple organisms, such as *algae* and *haloarchaea* [3]. NpHR, a functionally distinct class of opsin genes, enables the control of gradients across the cell membrane by transporting chloride ions from the extracellular medium into the cell [4]. On the other hand, MiniSOG, a genetically-encoded photosensitizer, generates sufficient quantity of singlet oxygen inside the cell to effectively cause phototoxic effects that lead to cell death [5].

Due to the opportunities it provides, this technology holds great potential for both studying the nervous system and providing innovative therapeutic and regenerative solutions for injured patients [6]. The integration of optogenetic technologies in living bodies paves the way for achieving the full potential of this technology by manipulating cell activity *in vivo* [7]. For this reason, developing optogenetic systems capable of being incorporated into living creatures is of great importance for both neuroscience and medicine. Cell photostimulation in a living body requires medical implantable devices to carry out effective high-precision light delivery. Simultaneously, supplying power to these devices is also a critical factor determining their reliability. Optimal optical cell stimulation parameters are required so as to obtain precise responses and reduce losses. In parallel to these requirements, the physical characteristics of these endoprosthesis should make them practical and easy-to-carry for the user.

1.1 Significance of this research

Optogenetics has contributed significantly to dissecting human neural circuits. If successfully adapted as a neuroscience technology, the proteins and the methods involved in optogenetics could be immensely significant, since controlling the activity of targeted cell types with high temporal and spatial resolution may offer clarifications on cellular codes shaping the basis of circuit computation and behaviour. Although major breakthroughs have been made on this technology during the last decade, there is still much potential for further discovery.

Central nervous system insults (CNS), such as stroke, Alzheimer disease, Parkinson disease and spinal cord injury represent more than 8 million deaths per year worldwide[1] and at least 1 million of new cases per year of highly disabling pathologies[2]. While most attention has originally focused on the neuronal death that occurs in these insults, current evidence suggests major roles for glial cells in their outcome. Astroglia is the most common type of glial cell in the central nervous system, and it reacts and proliferates in response to these disorders forming the glial scar to close the wound and control the damage. However, damage is contained at the expense of tissue repair and regeneration, as these scars and reactive astrocytes constitute strong physical and chemical barriers preventing tissue regeneration. Optogenetic technologies may become an important component of regenerative medicine, allowing a fine control of astroglia to retain their protective role while promoting neurogenesis and CNS repair. Proteins such as rhodopsins and miniSOG may prove to be important tools for controlling cell behaviour and killing specific cells, respectively. An analysis of living miniSOG-targeted cells behaviour upon light activation is carried out in this thesis, taking a step further in the integration of optogenetics functionalities into regenerative medicine.

Strategies to optogenetically control neural targets require a more optimized light delivery system than those used at recent studies and a deeper knowledge on the behaviour of cells upon stimulation. In the present work, observing the cells response to light stimulation, could allow the identification of optimal optical cell stimulation control parameters. Simultaneously, these observations could provide enough information to enable the estimation of a relationship between the input and output of the cell, essential for both understanding the system and providing a basis that precedes control applications.

Beyond fatal disorders characterized by neuronal death and astrogliosis, optogenetics technology may also serve as a therapeutic tool for disabling neurological diseases, such as chronic pain and hypertonia, still without a suitable treatment. Optogenetic modulation of pain and motor circuits may fill this therapeutic gap. This thesis explores different designs and components of a spine endoprosthesis concept, enlarging the considerations which must be taken into account when transferring this technology into the human sphere.

[1] https://www.who.int/mediacentre/factsheet/fs310/en
[2] https://www.who.int/mediacentre/factsheet/fs384/en

1.2 Goal of dissertation

The research presented in this dissertation aims to develop and test an optical neurostimulation endoprosthesis concept, which implements actuation to provide optical stimulation of cells subjected to optogenetic modification. To achieve this objective, several sub-specific goals need to be addressed:

1. Literature research on optogenetic technologies and analysis and selection of methods;
2. Analysis of light requirements and selection channels for cell stimulation;
3. Design and validation of a control system for light delivery;
4. Design and validation of a power supply system capable of delivering energy to device placed inside a body;
5. Testing the devices on optogenetically targeted cells to identify optimal optical cell stimulation parameters and model cell response to light.

1.3 Thesis Outline

The present thesis is organized into five chapters, with each chapter building on the previous one. The remaining chapters include but are not limited to the following content:

Chapter 2 provides insight on optogenetic technologies, giving basic background on the existing methods and tools as well as what has been achieved so far and future promises of this field. This chapter also establishes a bridge between the biological and engineering domains that characterize not only this thesis but also this field of work.

Chapter 3 explains the methods and elements chosen to develop the endoprosthesis device. An initial section lays down the important features and requirements of the implant and paves the way for the following sections which explore the different procedures taken in this research.

Chapter 4 contains the results from the *in vitro* experiments and validation of the various methods used to develop the device. The experimental results are discussed and, if that is the case, compared with simulation data.

Chapter 5 concludes and provides recommendations for future work.

Chapter 2

Optogenetics in Neural Systems

The term ”optogenetic” was first mentioned in a scientific communication in 2006 by Gregor Miller. The definition of the term has been evolving in time alongside with technology itself. The first neurobiological applications limited the usage of the term for a relatively narrow subject: “genetic targeting of specific neurons or proteins with optical technology for imaging or control of the targets within intact, living neural circuits” [8]. In 2010, *Nature Methods* introduced optogenetics as “Method of the Year”. By then, Karl Deisseroth, developer of pioneering optogenetics techniques, defined optogenetics as “the combination of genetic and optical methods to achieve gain or loss-of-function of well-defined events in specific cells of living tissue”. This definition includes the necessity of genetic intervention together with light control, and also defines the output as any detectable change of the living organism.

The possibility to use light for controlling neural activity was proposed for the first time by Francis Crick in 1999 [9]. Soon the first genetic manipulation which led to photosensitizing selected neurons was reported by the laboratory of Gero Miesenböck [10, 11]. Shortly afterwards, modified ion channels were introduced into cell membranes and light was used to alter the ion flow of the cell [12, 13]. The next milestone was set in 2005, through photocontrol of animal behaviour by illumination of a genetically modified group of neurons [14]. The first applications of *channelrhodopsin* as an optogenetic tool were reported in cultured mammalian neuron cells [15] and in *Caenorhabditis elegans* [16]. This approach became routinely applied in various cell types/organisms to induce specific responses and alter the behavioural pattern of the various animals.

Optogenetics relies on: i) light-activated optogenetic actuators (such as opsins, miniSOG and others), which promote inward and outward currents across the cell membrane and other functional responses; ii) strong and specific genetic targeting of actuator expression in the cellular population of interest; and iii) light delivery for optical stimulation with high spatial and temporal resolution. Diverse optogenetic actuators allow versatile control over neural activity. Each tool responds to specific stimulation features, allowing for independent control of each one of them.

2.1 The Microbial Opsin Family of Optogenetic Actuators

The key properties of these microbial optogenetic tools are highly related to their original host organisms. Type I opsins are protein products of microbial opsin genes and are termed rhodopsins when bound to retinal. These proteins differ from their mammalian counterparts (type II opsins) because of their light-sensing properties [2]. The possibility of these proteins acting as light sensor and ion conductors at the same time paved the way for functional optogenetics. Rather than simple photoexcitation or photoinhibition of targeted cells, optogenetics must deliver i) gain-of-function, conferring new or enhanced activity on a protein function or ii) loss-of-function, resulting in a reduction or abolition of a precise event [2]. Optogenetic modulation of activity only occurs in transfected neurons, expressing opsins on their membrane surface. When photo-activated, these opsins function as gates for specific ions leading to either depolarization or hyperpolarization of cells. This creates the opportunity for controlling activation patterns of specific transfected cells through light delivery. Viral vectors, modified to only target certain cell types, are commonly used to transfer genetic material into neurons in vivo. Alternatively, global opsin expression can be accomplished by genetically engineered transgenic animals [6]. On the other hand, various DNA transfection methods are used for achieving the expression of proteins of interest in in vitro cell cultures. (e.g. liposomes or calcium phosphate).

The first identified type I protein was the *haloarchaeal* proton pump *bacteriorhodopsin* (BR; Figure 2.1; [17]). Under low-oxygen conditions, BR is highly expressed in *haloarchaeal* membranes and act as a part of an alternative energy production system, pumping protons from the cytoplasm to the extracellular medium. These proton pumps have also been found in a wide range of marine proteobacteria as well as in other kingdoms of life.

A second class of microbial opsin genes encodes *halorhodopsins* (HR; Figure 2.1), a light-activated chloride pump first discovered in *archaebacteria* [18]. HR operates by pumping chloride ions from the extracellular to the intracellular space. After initial identification of halorhodopsin, other members of this class were also identified, such as a *halorhodopsin* from *Natronomonas pharaonis* (NpHR; [19]). Discovered in 1982, NpHR recently became the most widely used halorhodopsin in optogenetics. Both BR and HR mechanisms result in hyperpolarization and thus inhibition of action potential firing and neuronal activity

Afterwards, a third class of microbial opsin gene, *channelrhodopsin* (ChR; Figure 2.1) was identified by Nagel et al. [20] in 2002. Researchers demonstrated light-activated ion-flux properties for a protein encoded in the genome from the green algae *Chlamydomonas reinhardtii*, similarly to what other researchers had previously achieved regarding HR and BR. Subsequent developments described a second and third *channelrhodopsin* version [16, 21]. In *channelrhodopsins*, the ion-conducting activity is largely dissociated from the photocycle. Here, a cation channel pore is opened, implying that the ion flux becomes dependent on the kinetics of channel closure [22]. In neurons, photocurrent due to ChR activation is dominated by cation flow rather than by the pumping of protons, resulting in depolarization and activation of neurons.

Each type of opsin has unique properties in terms of which ions they gate and what wavelengths

activate them, contributing to a wide range of optogenetic actuators and functionalities available to neuroscientists. These tools are suitable in four major different categories of action [2]: fast excitation; fast inhibition; bistable modulation (which give rise to prolonged photocurrents far outlasting the initiating pulses of light, functioning as a step function); and control of intracellular biochemical signaling in neurons and other cell types. Optogenetic technology started with BRs, HRs and ChRs from various species and, since then, many different versions of these opsins have been developed, which are functional in neurons with a range of distinct and useful intrinsic properties.

There are fundamental differences between pumps and channels. Pumping always takes place against the electrochemical gradient, and slows down when the gradient is high [2]. Therefore, for efficient pumping, it is required not only sufficient light but also suitable ion concentrations, which can be modified within certain limits in a living tissue. These are the main reasons why there are more mutant channels available than modified ion pumps.

Microbial opsins remain remarkable for both i) unitary encoding of light sensation and final effector capability by a single compact gene and ii) virtually zero dark activity, along with millisecond-scale response to well-tolerated wavelengths and intensities of light. These properties have provided motivation and paved the way for investigation of further functionalities and opportunities offered by optogenetic technology.

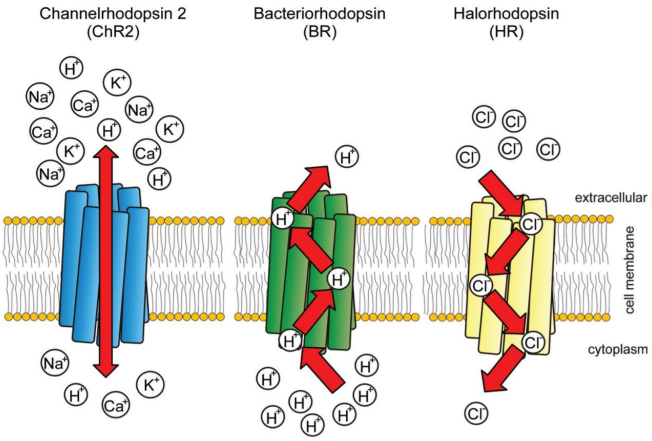

Figure 2.1: Functional features of microbial opsins: i) *channelrhodopsin-2* acts as a light-induced cation channel; ii) *bacteriorhodopsin* functions as a light-induced outward proton pump; ii) *halorhodopsin* functions as a light-induced inward chloride pump. Figure retrieved from [23]

2.2 Therapeutic Advantages of Optogenetics

Optogenetic technology is based on the integration of genetic targeting techniques and optical tools for reversible activation and inhibition of specific populations or single neurons. The modulation of the neuronal activity is a major benefit for studying neuronal circuit dynamics which shape animal behaviour. More broadly, research on therapeutic methods is also expected to benefit from optogenetic techniques.

For the purpose of both understanding the brain's complexity and establishing safe treatment methods, a demand for promoting behavioral research using optogenetic modulation of neuronal activity in appropriate animal models arises. Optogenetic methods may be used to causally probe circuitries un-

derlying complex behavior, as well as to dissect signaling pathways and construct models of psychiatric diseases through gene loss and gain-of-function experiments. New optogenetic research areas such as cellular probing of signaling mechanisms and optical readout of neuronal activity are emerging and may set the stage for precise closed-circuit control and therapeutic intervention in human disease [24].

Functional electrical stimulation (FES) is the current clinical conventional approach used for stimulation to restore function and provide therapy in a wide range of clinical applications, including some symptoms of Parkinson's disease [25] and epilepsy [26]. This technology has been used to regulate respiration, bowel, bladder, and sexual function in spinal cord injury patients, as well as to improve muscle conditioning in patients with muscular degenerative diseases [27, 28]. Products relying on this technology, as the ActiGait (Figure 2.2) which aims to help people suffering from foot paralysis, have been introduced to the market as therapeutic methods.

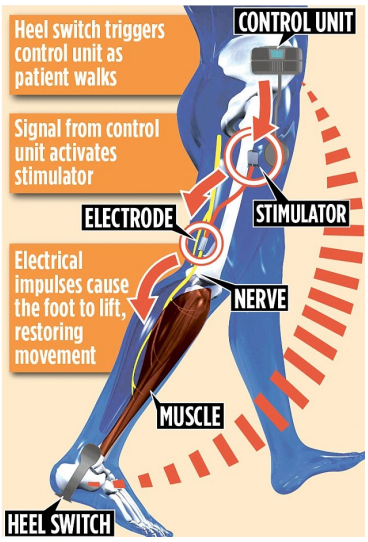

Figure 2.2: ActiGait system. Figure retrieved from www.dailymail.co.uk/health/article-3510771/Walking-thanks-tiny-switch-sock.html.

However, these therapeutic approaches have still have limited rate of success. For example, Deep Brain Stimulation (DBS) uses electrical stimulation to correct dysfunctional neural circuits but it indiscriminately affects both neurons and fibers of passage and it is unable to target specific cell types in the highly heterogeneous Brain [29], creating uncertainty regarding the predicted spatial effect of the method (Figure 2.3). Furthermore, the effects of electrical stimulation are often not clear as whether they cause excitation, inhibition, or both, ending up inconclusive regarding neurological mechanisms that cause or treat the disease. Something similar happens to electrical stimulation applied to muscular degenerative diseases where it performs reverse order recruitment, activating large motor units (large diameter axons innervating large, fast-twitch, oxidative, muscle fibers) before small motor units (small-diameter axons innervating slow, fatigue-resistant muscle fibers). FES tends to provide gross motor control, generally allowing access to only high levels of force output from a muscle. Small, slow twitch fibers, which provide lower magnitudes of force, cannot be selectively recruited, leading to quick fatigue [30]. These limitations create the necessity for more innovative treatment strategies, and optogenetics could be one of them.

In contrast to bulk electric stimulation of tissues, optogenetics provides temporally precise control of

activity in well-defined neuronal populations, using genetically-encodable light-sensitive proteins. Software for real-time detection has been coupled with optogenetic control to reduce seizure duration and severity, by targeting and activating PV-containing hippocampal interneurons [4] with ChR2 or by inhibiting eNpHR-expressing hippocampal excitatory neurons [31]. Researchers have identified two groups of neurons that can be switched on and off to alleviate the movement-related symptoms of Parkinson's disease [32]. The activation of these cells in the basal ganglia relieves symptoms for much longer than current therapies, like DSB and pharmaceuticals. Experiments with open-loop and closed-loop optogenetic stimulation methods have demonstrated increased performance and reduced muscle fatigue as compared to FES of the same nerve. [22, 30].

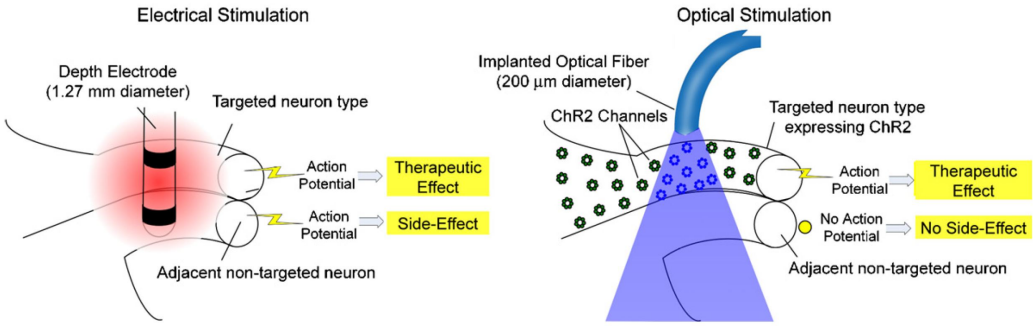

Figure 2.3: Comparing effects of electrical and optogenetic stimulation of neural tissue. (a) Electrical stimulation non-specifically affects all cell types near the electrode. (b) On the other hand, optogenetic stimulation affects only those neurons of a specific type that have been genetically targeted to express the optogenetic actuator. Figure adapted from [33]

2.3 Potential Contribution of Optogenetics for Regenerative Medicine

Astroglial cells are the most common cell type in the human central nervous system (CNS). Here, they play a critical role in neuronal survival, synaptic transmission, and maintenance of the blood-brain barrier in normal conditions [34]. Astroglia react and proliferate in response to most CNS insults, such as stroke, Alzheimers disease, Parkinsons disease and spinal cord injury [34]. These disorders represent more than 8 million deaths per year worldwide and at least 1 million of new cases per year of highly disabling pathologies. In case of injury, reactive astroglia forms the glial scar to close the wound and control the damage. However, reactive astroglia and the glial scar are strong physical and chemical barriers that inhibit neurogenesis, axonal outgrowth and promote further astrogliogenesis and neuroinflammation, preventing tissue regeneration later on [35]. Even though the adult human CNS has neural precursor cells with the potential to produce new neurons and regenerate the tissue after injury, in practice it favours the production of astroglial cells, especially in pathological conditions.

Overcoming the strong pro-gliogenic environment in the adult or injured CNS, which prevents neurogenesis, may be a key factor for achieving successful regeneration in the CNS. Optogenetic technologies may become an important component of regenerative medicine, allowing a fine control of astroglia to retain their protective role through innovative optogenetic tools while promoting neurogenesis and CNS repair. The control of cell behaviour and fate can be achieved by means of light-sensitive effector pro-

teins, such as rhodopsins (as those mentioned in section 2.1 which can be used to control astroglial function) or the mini singlet oxygen generator (miniSOG) protein. MiniSOG is a relatively new fluorescent protein tag that can be used for imaging any protein by means of both fluorescence and electron microscopy, but also for disrupting cell function or killing specific cells [36].

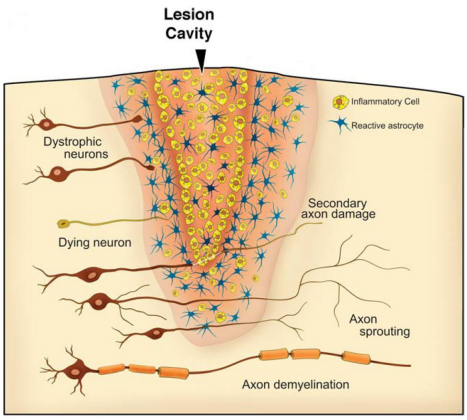

Figure 2.4: Response to injury in the central nervous system. Following trauma, an influx of inflammatory cells and reactive astrocytes causes the lesion cavity to expand, resulting in secondary damage to axons spared by the initial insult, causing demyelination and increasing local concentrations of myelin-associated inhibitors. When combined these factors inhibit regeneration. Figure adapted from [37]

2.4 NpHR as a Tool for Hyperpolarization and Neuronal Activity Inhibition

Channelrhodopsin expression in neuron's axonal surface combined with adequate optical excitation enables precise activation of living circuits, that is to say the creation of action potentials in the targeted region. However, ChR2 can only be used to prompt spiking patterns in neuronal circuits (gain-of-function) and test behavioural responses. Because it cannot cause inhibition of native spiking, examining the physiological function of a specific single or group of cells requires an hyperpolarizing agent.

Hyperpolarization is a change in electric charge distribution in the cell's membrane potential which results in values bellow the resting potential. It is the opposite of a depolarization, during which the membrane potential rapidly shifts from negative to positive. In other terms, hyperpolarization inhibits action potentials by increasing the stimulus required to move the membrane potential to the action potential threshold. It is, in part, caused by the influx of chloride ions (Cl–) through the appropriate channels (Figure 2.1).

Researchers have discovered an hyperpolarizing fast optogenetic tool, the *halorhodopsin* (HR), which causes chloride influx in response to light. However, it showed excessive desensitization [21]. On the other hand, the homologous gene from *Natronomonas pharaonis*, NpHR induces suitably stable outward currents [21]. NpHR is activated when irradiated by yellow light, at a peak wavelength of 590 nm, at which ChR2 shows no response at all, enabling independent activation of ChR2 and NpHR to bidirectionally modulate activity. This chloride pump was shown to be effective in neurons and has been used as a hyperpolarizing tool for induced reversible inhibition of neural activity. Unlike *channelrhodopsins*,

NpHR is a true pump and requires constant light in order to move through its photocycle.

An enhanced version of NpHR, eNpHR displayed increased peak photocurrent in the absence of aggregation or toxicity, and optical inhibition was observed not only *in vitro* but also *in vivo* with thalamic single-unit recording [4] (Figure 2.5). The new enhanced NpHR (eNpHR) allows safe, high-level expression in mammalian neurons, without toxicity and with augmented inhibitory function, correcting a major limiting factor for the application of optogenetic neuron inhibition. Two versions modified for enhanced membrane targeting in mammalian neurons - eNpHR2.0 and eNpHR3.0 have been reported [38], with eNpHR3.0 providing larger photocurrents than eNpHR2.0. *Halorhodopsin* and its enhanced versions have been used in studies ranging across mammalian brain slices [21], freely moving worms [21], cultured neurons [21, 39] and living mammals [40–42].

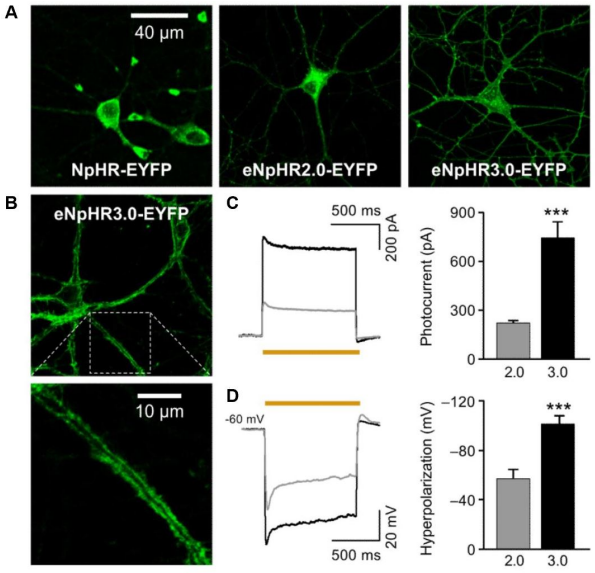

Figure 2.5: (A) NpHR (left) and enhanced versions eNpHR2.0 (middle) and eNpHR3.0 (right) coupled with EYFP for showing expression through fluorescence. (B) Membrane expression enabled in processes for eNpHR3.0 (confocal images showing membrane-localized EYFP fluorescence in the soma (top) and dendrite (bottom)). (C) Photocurrents in cells (left) virally transduced with eNpHR3.0 (black) and eNpHR2.0 (gray). Summary plot (right) showing average photocurrent levels in cells expressing eNpHR3.0 (747.2 93.9 pA) and eNpHR2.0 (214.1 24.7 pA). (E) Voltage traces in cells (left) virally transduced with eNpHR3.0 (black) and eNpHR2.0 (gray). Summary plot (right) showing average hyperpolarization levels in cells expressing eNpHR3.0 (101.0 24.7 mV) and eNpHR2.0 (57.2 6.8 mV). Figure and value adapted from [43].

The magnitude of the photocurrent in a neuron generated by a pulse of light depends on many factors, including the properties of the protein expressed, the intensity and duration of the pulse, the wavelength and the recent history of illumination (recent activity of the opsins channels/pumps and their current state) [15]. In any case, the rate of absorption of photons of a given wavelength is proportional to the number of photons incident per unit of time per unit of area. Therefore, measuring and controlling this parameter is of the highest importance when designing a light delivery system to activate a certain optogenetic actuator. In order to create a simple and practical measuring process for quantifying the photon flux, it is convenient to report the ”light power density” (typically measured in mW/mm^2), as there is a wide variety of light power meters commercially available, which measure total light power (in Watts). Light power density is the photon flux multiplied by the energy of the individual photon, which is inversely proportional to its wavelength.

Light requirements vary among the wide spectrum of optogenetic tools, and the specific properties of the protein actuators must be considered when designing the experiment. For example, optogenetic

inhibition may require continuous light for as long as inhibition is desired, whereas bistable optogenetic control [44] only requires brief light pulses, typically at much lower power. Gradinaru et al. experimented with various hyperpolarizing tools fusing them with enhanced YFP (eYFP), cloned the opsins into an identical lentiviral backbone with the excitatory *CaMKII* promoter and expressed the opsins in cultured neurons. To focus on differences independent of expression, Gradinaru et al. created a categorizing system [38] in which they normalized photocurrents in each cell and used the curve fit to calculate the light power density required to achieve half-maximal activation (EPD50 or effective power density for 50% activation), a measure of sensitivity independent of protein expression. He found light sensitivity of the hyperpolarizing pumps by measuring photocurrents in neurons under a range of light power densities from $0.05mW/mm^2$ to $20mW/mm^2$. As expected, they found out that the most recent version of NpHR (3.0) had much larger operational light sensitivity than the initial ones (1.0). For eNpHR3.0 specifically, EPD50 was quantified as $5.4mW/mm^2$. They also analyzed the temporal precision of hyperpolarizing photocurrents by quantifying on kinetics: τ_{on}, the rate of channel opening and τ_{off}, the rate of channel closure at the beginning and end of the light pulse. They noticed that off kinetics (τ_{off}) and population light sensitivity were inversely correlated for hyperpolarizing optogenetic tools. Although from a molecular perspective light sensitivity only involves the efficiency by which an individual protein is activated by light (intrinsic sensitivity), cells expressing optogenetic protein populations with slower off kinetics will effectively appear more light-sensitive upon prolonged light stimulation. Since many behavioral neuroscience experiments may require prolonged inhibition (on the order of minutes), Gradinaru et al. also studied the stability of the hyperpolarizing photocurrents of the various optogenetic tools. Whereas all pump photocurrents decayed across 60 s of continuous light, eNpHR3.0 currents revealed to be the most persistent of all tools studied.

Light parameters are, therefore, of the highest significance in the optogenetics control context. Studying cell response to controlled light provides significant improvement in optogenetic systems and a step forward in this technology.

2.5 MiniSOG as a Tool for Photo-Inducible Cell Ablation

Tools for selective ablation of cells in a temporally and spatially precise manner could enable to dissect the function of a cell within a complex network such as the nervous system. Genetically encoded cell ablation reagents are highly desirable, as they can be used in combination with a variety of cellular manipulations.

Exogenous photosensitizers have been identified which release reactive oxygen species (ROS) upon light excitation. Photo-inducible cell killing takes advantage of the ability of ROS to potentially damage any macromolecules within the cell by over-oxidation. In other words, when the oxidative stress reaches a certain threshold, cell death occurs [5]. Even though chemically based photosensitizing has been used in photodynamic therapy, they also accumulate in tissues other than cancerous cells, causing nonspecific toxicity. Genetically encoded photosensitizers as the mini singlet oxygen generator (miniSOG) enable a higher level of selectivity.

MiniSOG is a green fluorescent protein engineered from *Arabidopsis phototropin 2* [36]. Upon blue-light illumination (∼450 nm), miniSOG generates a sufficient quantity of singlet oxygen and has been shown to effectively catalyze local polymerization of diaminobenzidine (DAB) into precipitates for imaging using electron microscopy, providing high-resolution images [45]. There is a functional association between fluorescence and the production of singlet oxygen by miniSOG when it is irradiated by light [46]. Previously reported works on photo-inducible cell ablation have used light power density value between 0.5 to $2\ mW/mm^2$ [5, 36, 45] for miniSOG activation. Phototoxic effects caused by miniSOG can be graded by modulating the duration and the intensity of light. Protocols for efficient cell photoablation use light power density levels of $0.5mW/mm^2$ for a prolonged time (30–90 min) that enables ROS-mediated activation of cell death pathways in *C.elegans*. Changing light exposure from continuous to pulsed has also been demonstrated to increase the efficiency of photo-induced cell ablation [5]. This clearly demonstrates that optimization of illumination parameters is important for modeling the effect of miniSOG on cells.

2.6 Light Delivery Constitutes a Challenge for Optogenetics

A key factor for achieving successful photostimulation on targeted opsin-expressing neurons is a practical and effective light delivery during neuronal activity modulation. Light delivery is, therefore, a key challenge in applying optogenetics to understand and control the nervous system of animals.

Initially, the solutions to this problem depended on tethered optical fiber-based systems, in which a fiber optic is inserted inside the brain of the animal subject to study [47–49] (Figure 2.6). This kind of light delivery system takes advantage of the stable nature of the brain-skull interface, allowing for consistent modulation of identified neural populations. This type of system went through a few improvements since its early stages, such as allowing fiber rotation during animal movements, rotary connectors or improving the ease of attachment and detachment [50]. However, tethered systems impose significant constraints on experimental design and interpretation of the results.For example, the subjects of study are physically restrained by an attachment which limits the environments in which optogenetic experiments can be performed. This constraint is especially significant if more than one animal is needed to study social behaviours.

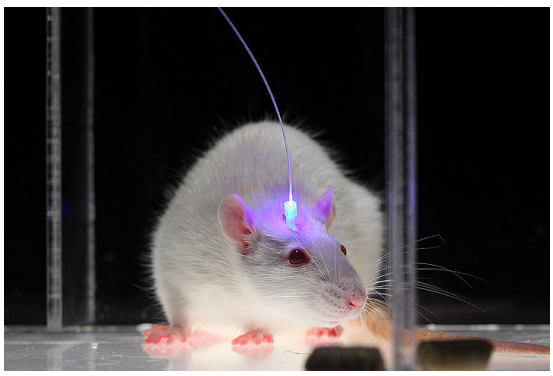

Figure 2.6: Applied tehtered optogenetic system to mouse under study. Figure retrieved from [50]

In order to improve the experimental conditions and reduce the constraints imposed by light-delivery technology, some efforts have been made to eliminate tethers, by introducing both wireless-powered [51–55] and battery-powered head-mounted devices [56, 57]. These devices deliver light to the surface of the brain using light emitting diodes (LED). Deeper brain regions can also be targeted with flexible, injectable LED systems, either battery-powered [58] or wirelessly-power through a head-mountable receiver [59, 60]. Even though the tethering constraints have been solved by the reported solutions, the wireless devices are relatively bulky and heavy. While a mouse head (most used animal in optogenetics experiments with mammals) weighs typically around 2g, these devices weigh is on the range of 0.7-3g. In addition to this, these head-mountable devices come out several millimeters from the skin and cannot be left attached to the animal head for long periods of time. The mass and volume of these devices make their application on the spinal cord and PNS very unlikely. For example, inserting optical fiber in the spinal cord will require severing of white matter tracts which carry high information density and have minimal redundancy. For this reason, in this context, local damage can have important global consequences. Moreover, these devices ultimately influence the behaviour of these animals, constraining their freedom of movement, by, for example, preventing them from entering in small enclosures.

The concept of wireless and battery-less devices, which benefit from power transmission, is becoming more critical in the medical device field due to a variety of problems associated with thermodynamic chemical reactions that occur in batteries such as having a slow recharging rate of several hours, limited charge/discharge cycles, and being a bio-hazard if toxic materials are leaked [61]. Batteries that sustain sufficiently long stimulation periods require bigger dimensions as well as a bigger mass, thus interfering with the subject's freedom of movement. Therefore, it is beneficial to fabricate smaller battery-less micro-devices to power LEDs during photostimulation. Yeh et al. reported the development of a small power receiver (chip area $< 9mm^2$) designed for stimulation of cardiac muscle cells in mice, with a small coil for harvesting energy through electromagnetic (EM) midfield [54]. However, this system transferred power over a small behavioral area with pulse frequencies too variable for being controlled and used for optogenetic stimulation.

Some reported implantable devices take advantage of micro-LEDs inserted into the site of stimulation, instead of relying on optical fibers to deliver light. Optical fibers are typically able to illuminate ventral structures from the fiber tip, whereas micro-LEDs, which can come in a wide range of sizes, have the advantage of complete customization, including the shape and size of the photostimulator. In addition to this micro-LEDs systems are substantially less costly than the ones relying on optical fiber. Because of the low power demands of advanced semiconductor micro-LEDs, radio frequency power harvesting systems make it possible for an optogenetic system to be partially or fully implantable at the site of stimulation. Montgomery et al. reported the development of the first fully internal device [55] for wireless optogenetic stimulation of brain, spinal cord, or peripheral nerve endings (Figure 2.7). This device is smaller and lighter than any previously reported wireless optogenetic systems (10 to 25 mm3 in volume and it weighs 20 to 50 mg depending on the target neural structure), and consists of a power receiving coil, a rectifier circuit, and a micro-LED (Figure 2.7 B). The implant is powered using an aluminum resonant cavity, in which the mouse was cloistered (Figure 2.7 A), coupled to the implant

receiver coil, at an operating frequency of (1.5 GHz). The size, geometry, and resonant frequencies of the implant and cavity were particularly optimized for this animal. Due to its shape and size, the new device was implanted in peripheral location, allowing to expand the range of optogenetic experiments *in vivo* and stimulating targets beyond the brain. Optogenetic stimulation experiments were successful in the brain region, spinal cord and peripheral nerves, for both ChR2 and NpHR protein expression.

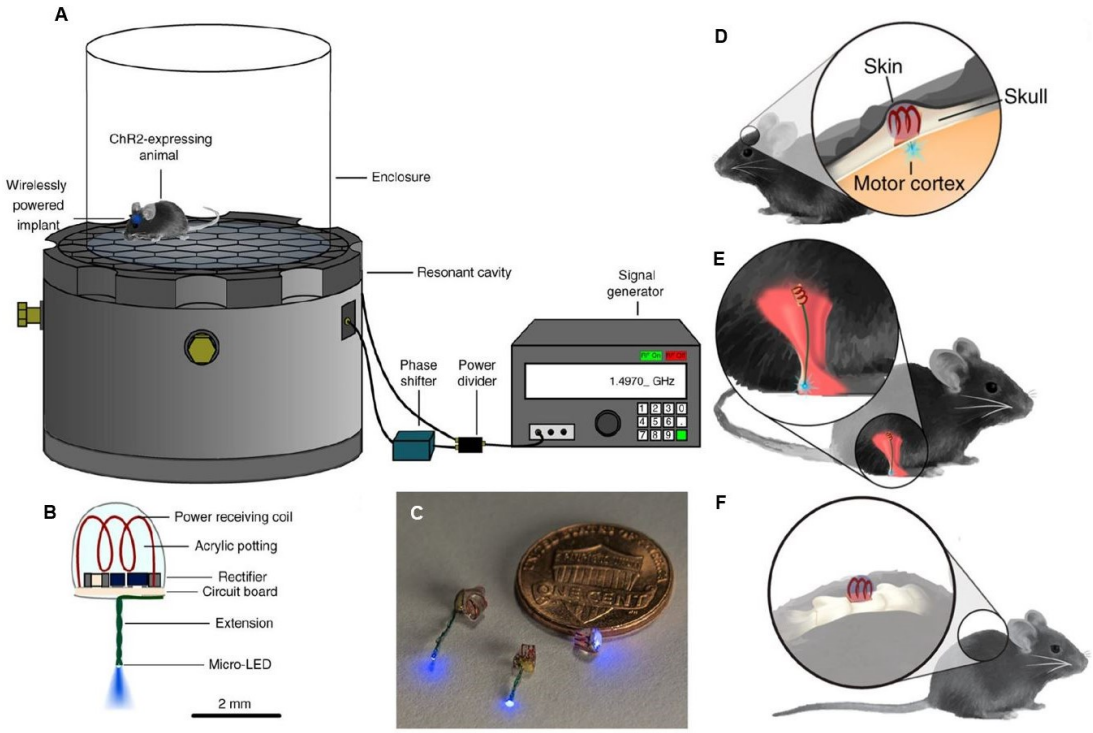

Figure 2.7: Light delivery system developed by Montgomery et al. [55]. (A) Diagram of light-delivery system. (B) Schematic of wireless implant customized for the brain. (C) Size comparison of wireless implants (left to right: peripheral nerve endings, brain, spinal cord) with a US 1-cent coin. Three different positions for stimulation: (D) Stimulation of premotor cortex: positioning of the device: the circuit board and coil are above the skull and below the skin; the LED at the tip of the extension is inserted into the brain directly above motor cortex. (E) Stimulation of nociceptors at the spinal cord: the device is implanted on the right side of the dorsal surface of the vertebra; light is delivered through a drilled hole to L3/L4 of the spinal cord. (E) Stimulation of peripheral nerve endings: positioning of the device: the circuit board and coil are subcutaneous and adjacent to the triceps surae muscles; the micro-LED extension is subcutaneously routed to the heel.

2.7 Multiple Possible Readouts for Neuronal Activity

Optogenetic control has been shown to be compatible with diverse behavioral readouts in a wide range of organisms, from invertebrates such as worms [21] to vertebrates such as fish [62] and mammals [55]. The latest generation of optogenetic technologies enables not only smaller and less bulky devices, but also free behavior in the complete absence of tethered optical devices. Therefore behavioral measures in the setting of optogenetics are relatively straightforward and can be mapped into a wide range of validated animal behavioral measures present in the literature. However, having an expected behavioral response does not necessarily mean that we are activating or inhibiting the circuits of interest, and it is difficult to infer molecular and cellular mechanisms from macroscopic changes. Optogenetic setups where the readout is the actual physiological response of a neuronal circuit enable in-depth studies on the behavior of optogenetic proteins and the molecular mechanisms involved in the

transmission of information. A fully equipped neuroscience optical toolbox should include multiple reliable readout technologies for answering a broad range of experimental questions, *in vitro* and *in vivo*. The three main categories of measuring methods are: electrical, optical, and magnetic resonance.

Simultaneous optical stimulation and electrophysiological recording (patch clamping technique; Figure 2.8) of neuronal activity *in vivo* became possible with integrated sub-millimeter scale optical stimulators (such as fiber optics) and recording electrodes. These breakthroughs enabled measurements of local-circuit responses with high temporal precision that matches the millisecond timescale of opsin-based optical control. Getting this feedback is of high importance not only for experimental reasons but also for eventual optical stimulation, allowing therapeutic stimulation parameters to be rapidly set in patients. One key advantage of optogenetic stimulation is the possibility of simultaneous electrical recording to be carried out. Typically, such simultaneous input/output processing is not possible with integrated electrical stimulation and electrical recording, due to the features which characterize artifacts associated with electrical stimulation. This composes a major limitation in functional neurosurgery and in our understanding of therapeutic brain stimulation modalities such as DBS [63]. The combination between optical stimulation and electrical recording, which is referred to as an ”optrode” (Figure 2.11) allows high temporal precision for electrical assessment of local responses, creating the possibility for locally evoked spikes to be directly visualized. These have ranged from fusion of optical fibers with metallic electrodes [63, 64], to coaxial integrated multi-electrode devices [65], to silicon probes for multi-site recording in awake, behaving animals [66]. However, these methods do not guarantee that recorded spikes are resulting from photosensitive cells, rather than from indirectly recruited cells. Usually this is not a concern, and optrode recordings still provide extremely useful feedback on the activity in the local circuit during control that could never be obtained with electrical stimulation. Electroencephalography is another electrical readout well suited for simultaneous use with optogenetic stimulation [67].

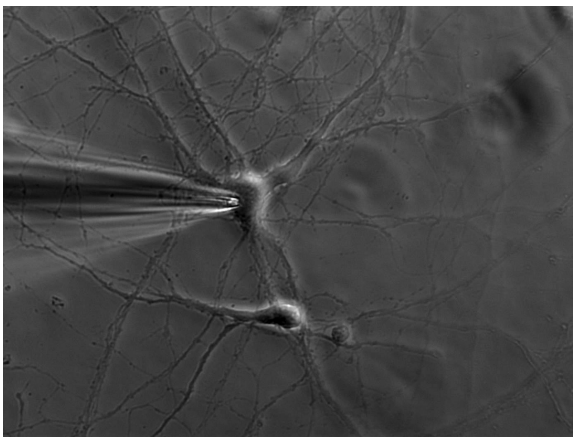

Figure 2.8: Patch clamp attached to the membrane of a cultured murine hippocampal neuron. Figure retrieved from www.leica-microsystems.com/science-lab/the-patch-clamp-technique.

The concept of all-optical control of neural circuits [8] is appealing as it can provide spatial distribution and cell type-specific optical readouts. Dye-based imaging has been conducted in combination with optogenetic control in a number of studies. Zhang et al. [21] used fura-2 in order to evoke ChR2-triggered $[Ca^{2+}]_i$ transients in cells, in a NpHR/ChR2 system, demonstrating that these opsins can be integrated

to achieve multimodal, bidirectional control of neural activity in intact tissue. Also using the fluorescence change of $[Ca^{2+}]$ dye Fluo-5F, Zhang and Oertner [68] compared the peaks of light-evoked and somatic current-evoked action potentials concluding that the ChR2 conductance outlasted and counteracted the repolarizing current. Voltage-Sensitive Dye (VSD) imaging is also an effective alternative for monitoring the electrical activity of large populations of neurons with high temporal resolution. Through high-speed cameras, researchers are able to capture optical changes and measure electrical activity changes in neurons. RH-155 [69], with absorption wavelength of around 700 nm, is a fine example of a VSD which allows all-optical stimulation and imaging as it is sufficiently separated from the excitation peaks of ChR2 and NpHR.

Optogenetic functional magnetic resonance imaging (ofMRI) is a technique which combines the spatial resolution of high-field fMRI (functional magnetic resonance imaging) with the high level of optogenetic stimulation precision. This combination enables cell type-specific mapping of functional neural circuits and their dynamics across the brain. Simply put this non-invasive approach makes it possible to determine brain's global dynamic response to optogenetic stimulation of specific neural circuits through measurement of the blood-oxygen-level-dependent (BOLD) signal [70] (which provides an indirect measurement of neuronal activity). One advantage of this technique over other methods for recording brain activity during stimulation, such as electrophysiology, is the fact that it provides a view of the entire brain at relatively high spatial resolution. This offers the possibility of detecting neuronal activity in response to stimulation at great distances from the site of stimulation without implantation of invasive recording electrodes. Furthermore, ofMRI offers advantages over the more traditional method of performing electrical stimulation during fMRI, as these can recruit different cell types near the electrode and consequently mix up the causal influence of each population. On the other hand, it needs the animals to be quiet, making it difficult to apply this method in social behaviour setups or even single-animal behavioral setups.

2.8 Genetically Targeted Optical Control Of Neural Activity

A fundamental goal in biology is to be able to control defined cells within functioning tissues. Temporal precision of control is important as cells may carry out different computations and deliver different outputs depending on the timing and context of the input signals. This means that changes in context or millisecond-scale shifts in timing may potentially change the magnitude or flip the sign of neuronal action in a circuit [71]. A specific cell type can be controlled by traditional genetics if the proper targeting strategies exist, but these approaches lack the temporal precision needed to control events with relevant behavioural triggering or timing. Additionally, pharmacological control strategies usually lack cell type specificity, temporal precision, or both.

Aiming to enable precise control of specific cell types in animals, researchers have been developing optogenetic technologies, working with properties of light-responsive proteins that transform brief pulses of light into desired precisely timed gain-of-function or loss-of-function of specified events in targeted cells *in vivo*. Zhang et al. [21] explored *halorhodopsins* for temporally precise optical inhibition. NpHR was selected for its step-like and highly stable photo-currents compared with other microbial

generators of inhibitory currents. Afterwards, NpHR–eYFP (using YFP for its fluorescence features) was introduced into cultured rat hippocampal CA3/CA1 neurons. They reported NpHR operating over a range of timescales from short (single-spike precision; Figure 2.9 A) to long periods of time (10 min; Figure 2.9 B). NpHR-mediated inhibition of spike trains was highly stable, remaining effective over many minutes. However there was a slight decrease in efficacy (Figure 2.9 C), with inhibition being more effective early in the light pulse, presumably owing to a slight inactivation of NpHR over time. Researchers suggested a reason for this phenomenon could be accumulation of non-functional NpHRs with a deprotonated Schiff base over long periods of light exposure. They also reported the successful use of NpHR to cancel multiple preselected ChR2-driven spikes (Figure 2.9 D) at identified positions in prolonged spike trains, enabling bidirectional control of neurons on the timescale of milliseconds.

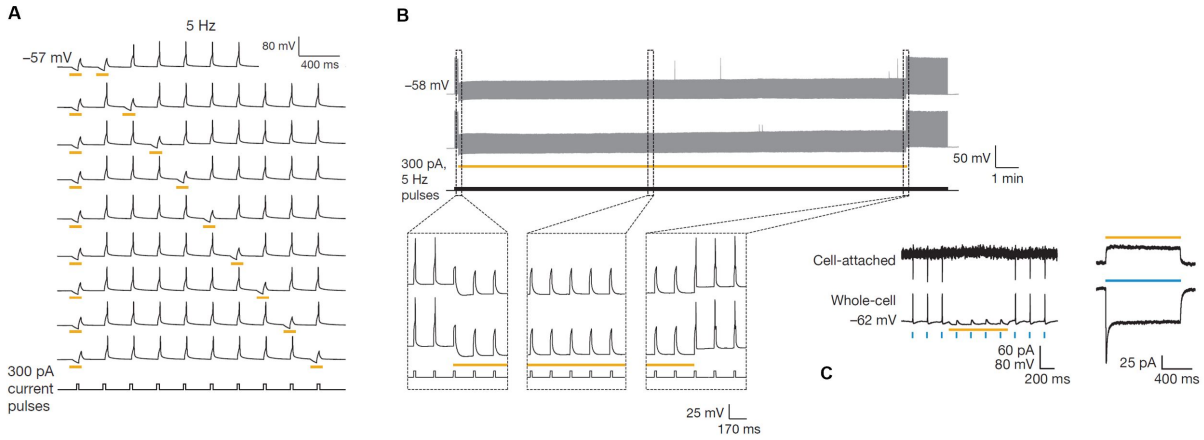

Figure 2.9: Research of Zhang et al. (A) Inhibition of spike pairs at different frequencies. Trains of ten spikes were evoked by 300 pA current injection pulses, and pairs of light pulses with variable temporal separation were used to inhibit the selected spikes. (B) Ten minutes continuous illumination (two successive sweeps) robustly inhibited neuronal spike trains elicited by current pulse injection (300 pA, 5 Hz). Dashed boxes show the inhibition on an expanded timescale. (C) *Left:* Cell-attached and whole-cell recording of neurons expressing NpHR and ChR2 demonstrating action potentials evoked by brief pulses of blue light and simultaneous illumination with yellow light inhibited spike firing. *Right:* Voltage-clamp recording showing independently addressable outward and inward photocurrents in response to yellow and blue light, respectively.

Most published optogenetic experiments in behaving animals can be categorized as open loop systems (Figure 2.10). In these experiments, light stimulus parameters (such as pulse frequency and duration) are selected on the basis of previous literature or direct neural recording, without directly feeding back the measured neural effects of the stimulation online. Optogenetic stimulation of brain, spinal cord and peripheral nerve endings of behaving mice implemented by Montgomery et al. [55] (Figure 2.7) was delivered with parameters based on information from literature and previously recordings of stimulation using ChR2.

In closed-loop optogenetics (Figure 2.10), the control action is a structured light stimulus that is automatically adjusted on the basis of the difference between desired and measured outputs, which may include electrophysiological, optical or behavioral readouts of activity generated by a biological system. Only very few studies have developed closed-loop optogenetic control systems to date.

Sohal et al. [72] used a closed-loop control method based on electrophysiology- dynamic clamp, to control inhibitory *parvalbumin*-positive interneurons through optogenetic stimulation triggered by observed pyramidal neuron spikes, implementing feedback inhibition of activity. Paz et al. [73] developed a closed-loop system to target thalamocortical neurons in injured epileptic cortex of awake rats, causing

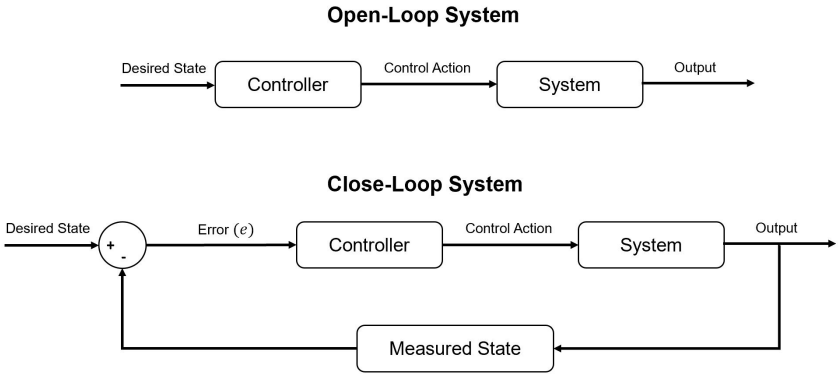

Figure 2.10: Block diagrams representing both open-loop and closed-loop systems.

a successful interruption of seizures identified by EEG (electroencephalography) and behavior. Here, online detection of seizures near the time of outbreak was used to hyperpolarize targeted neurons using eNpHR3.0. This study reports in rats the first evidence that the thalamus is required to maintain cortical seizures and consequently responsible for poststroke epilepsy, pointing out a therapeutic direction for this disease. Afterwards, Krook-Magnuson et al. [74] demonstrated that closed-loop activity modulation of parvalbumin-expressing neurons in the cerebellum caused a decrease in temporal lobe seizure duration. They also developed a closed-loop optogenetic system for hyperpolarization of granule cells in dentate gyrus which efficiently terminated spontaneous temporal lobe seizures and report that excitation of these cells substantially worsened spontaneous seizures [75]. In this work, analysing spontaneous recurrent seizures in individual animals provided features which enabled the construction of a model which characterized the early electrographic signal used to trigger the real-time closed-loop seizure detection software. Similar closed-loop manipulations have been developed to better understand causal roles within the nervous system as new directions into therapeutic methods [76, 77].

The previously mentioned studies used closed-loop optogenetics systems which included hardware to process real-time electrophysiological data online and adjust light parameters following specific control rules. Instead of electrophysiological variables O'Connor et al. [78] measured behavioral traits. This approach was used for stimulating single barrels of somatosensory cortex and use real-time measurements to optogenetically mimic touch-evoked neuronal activity during whisking of mice, aiming to evoke behavior consistent with a feeling of touch in whiskers. Through this experiment, researchers have discovered that instantaneous whisker position was not required for object localization. Srinivasan et al. [22] established a functional optogenetic stimulation system to control ankle joint position in murine models. They used the measurement of joint angle or fascicle length to build a feedback signal. They have developed a 3-phase, photo-kinetic model of the fundamental mechanisms for temporal variations in optogenetically activated neuromusculature through the use of ChR2. These methods and insights could be the beginning of optogenetic neuromuscular therapies and devices for peripheral limb control.

The multiple studies mentioned in this chapter attempted to create a connection between biological applications and the sphere of systems and control theory, similarly to what has been used effectively in the world of engineering for understanding and modulating complex dynamical systems. Along the way

there are multiple technical challenges inherent to optogenetic experimentation.

2.9 Systems Identification for Neuronal Circuits

Following a careful selection of suitable optogenetic actuators and sensors according to the cells of interest, online algorithms are necessary for designing light stimulation based on the observed neural behavior. Neuronal activity is measured by sensors which transfer the information to a controller, where it is used to build an estimation of the current state of the neural system. Algorithms use this estimation to compute a control action intended to achieve a desired activity level. This control action is carried out and the reaction of the system is, once more, recorded by the same sensors, closing the loop.

Neuronal circuits, as neurons themselves, are very complex systems, which are not only nonlinear, non-stationary and different from each other but they also change dynamically, within millisecond timescales. For this reason, successful integration of closed-loop control theory with neuroscience is expected to be a highly interdisciplinary task, regarding not only the optics and physiology involved, but also the computational and anatomical fields [79]. Since closed-loop depends on real time computation, with particular emphasis for systems involving fast dynamics, there is always a computational budget which leads to limitations on model complexity. On the other hand, strong genetic-targeting strategies are necessary for identifying specific cell-type roles in the dynamics of neuronal circuits, as well as for understanding neuronal circuit patterns, which adds computational challenges. Furthermore, safety and physiological constraints are highly important for the functional success of the system.

When considering feedback control methods, a few major distinctions should be considered. This methods can be categorized according to: i) linearity: linear versus nonlinear; ii) time representation: continuous versus discrete, iii) domain representation: frequency versus time [80]. Single-input-single-output systems (SISO) tend to take frequency-domain approaches due to a deeply developed theory on this matte. Proportional-Integral-Derivative (PID) control is predictably the most used in single fiber/microLED-electrode SISO applications [79]. Figure 2.11 illustrates the different approaches mentioned as well as some examples of studies using them.

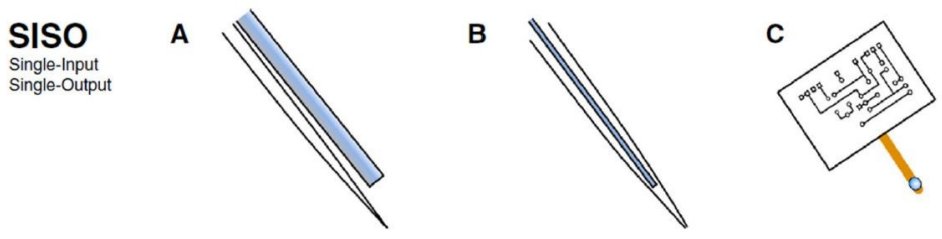

Figure 2.11: Combination Electrical-Optical Devices for Closed-Loop Optogenetic Control. Single-input, single-output (SISO) systems: (A) optrode [63], (B) optopatcher [81], and (C) integrated microLED optrode for chronic implantation [82]. Figure retrieved from [79].

Closed-loop control in optogenetics implicitly requires the existence of a model relating optical inputs to reactions on the neural system, which is used by the controller to choose the optogenetic inputs. For classical systems, this model is called ”input transfer function” [80]. Generally, the experiment starts with the exact knowledge of how stimulus, in this case light inputs, will perturb the system. Previous

work has mapped the stimulus parameters, by varying light intensity and frequency to better understand the relationship between optogenetic stimulation and neuronal reaction of an individual or a group of cells expressing optogenetic actuators. Estimating the relationship between inputs and outputs of a system is known as system identification. Control can be used as a mean for validating the quality of the system identification. However, in some applications, like in prosthetics, the close-loop control performance may prove more important then the quality of the identified model. In a SISO system, it is possible to effectively achieve ”system identification” without directly modelling the system by using a PID controller. In ”black box” modeling, it is assumed that the system is unknown and a its model is achieved by integrating through adjustable parameters aiming to fit the relationship between inputs and outputs. On the other hand, in “white box” modeling there is an accurate physical model of the system. In this case, black box modeling would consist in fitting the relationship between light inputs for optogenetic control and synchronous cell activity measurements. Limited system knowledge and imperfect control may lead to a ”model-free” approach, like PID control system.

Essentially, system identification should be considered both as a tool for understanding the system through reverse engineering. It also provides the basis that precede the control applications, for both basic science purposes (e.g. causal model validation) and practical purposes (e.g. neural prosthetics).

Chapter 3

Methods

3.1 The Optical Endoprosthesis Concept

Achieving practical and effective light delivery on targeted opsin-expressing neurons is a keystone factor for the success of optogenetic modulation of neural activity. Therefore, the evolution of optogenetic technologies is deeply connected to breakthroughs in photostimulation methods and challenges.

In vivo optogenetics experiments relied on tethered optical fiber-based systems [33, 47–49] (Figure 2.6), in which optic fiber fulfills the light delivery function. These systems have been refined over the years, becoming more sophisticated and allowing clearer experimental results (section 2.6). However, these systems have limitations which not only impose significant experimental constrains (section 2.6) but also important barriers regarding the therapeutic use of optogenetics, by limiting the environments and behavioural contexts in which this technology can be applied. Thus, researchers have been moving towards untethered systems, delivering light via wireless powered [51–55] and battery powered head-mounted devices [56, 57], which use light emitting diodes (LEDs). Despite the huge breakthroughs in wireless optogenetic technology, most of the devices available are still relatively bulky, bringing up mass and size-related issues that end up limiting their application (section 2.6). In 2015, in Stanford University, Montgomery et. al reported the development of the first fully internal device [55] for wireless optogenetic stimulation of brain, spinal cord, or peripheral nerve endings (Figure 3.1). Due its small size and weight, this device broadens the potential stimulation targets and allows animals to move freely, within a cage (Figure 2.7), constituting a major advance in the field.

The insertion of optogenetic technologies in a therapeutic and regenerative medicine sphere and its integration within a spinal endoprosthesis requires a high level of sophistication and effectiveness, aiming to enhance the well-being of injured patients. Accordingly, a few key aspects must be considered when designing a system for neurostimulation:

- **Size and Weight** will determine how practical the system becomes when carried by the subject. Bulky devices impose significant physical constraints which, ultimately, will affect the body motion of its carrier and its mobility.
- **Durability and Maintenance** are aspects which will shape the subject's living standards, as these

are parameters that will set the level of intervention after installation.

- **Efficiency** is of major importance for two main reasons. On the one hand, this element determines the level of energy necessary for the proper functioning of the system, which in turn affects the key points mentioned above. On the other hand, the less inefficient, the more energy the system will dissipate, which could mean an increase in temperature and have a direct impact on the tissues around the implant.

- **Safety** is of utmost importance. The subject should never be put in danger due to malfunction or instability of the device or of any components present inside it.

The development of an optogenetics based endoprosthesis for neurostimulation in the human sphere requires the analysis of the technology and resources available as well as their potential to fulfill the mentioned key requisites for therapeutic and regenerative use. This analysis will ultimately bring up the initial concept of an optical spine endoprosthesis - the object of study in this thesis.

The medical endoprosthesis definition provides the starting point of this analysis. The device to be developed should be placed entirely inside the body. From this point of view, tethered systems do not comply with this requirement. Furthermore, these systems are inevitably invasive which, besides reducing the subject's mobility, could become a source of infections and other health problems related to the high level of exposure. Alternatives for tethered systems can be found on the optogenetics technology spectrum, mostly relying either on wireless energy transfer through electromagnetic induction or on battery systems for providing power, and on LEDs for delivering light. As mentioned on section 2.6, battery-powered systems originate potential issues regarding the requirements stated. The risk of leakage of toxic materials compromises the safety of the subject. Furthermore, slow recharging rates and limited charge/discharge cycles also compose an issue regarding the durability and maintenance of the device. Moreover, batteries that sustain sufficiently long stimulation periods require bigger dimensions as well as a bigger mass, elevating the size and weight of the implant. Even though electromagnetic harvesting systems may present lower efficiency levels than battery-based systems, they seem, at this point, to be a more acceptable alternative for the power supply system. Finally, a light delivery system based on LED has size-related advantages due to a lower level of complexity comparing to systems based on optical fiber, considering the latter would be placed entirely inside the subject's body.

The device developed by Montgomery et al. (Figure 3.1) is smaller and lighter than any other previously reported remotely-controlled, wireless optogenetic system. Moreover, the device is relatively versatile regarding the area of the nervous system being stimulated, as the μLED can be positioned as desired at a certain distance from its source of power - the receiving coil which can be positioned near the skin surface. Finally, it also allows the highest level of mobility in *in vivo* experiments reported so far. For these reasons, Montgomery et. al's device satisfies some of the most crucial requirements for the integration of optogenetic neurostimulation in human patients and its features will be used as starting point for developing the concept of an optical neurostimulation spine endoprosthesis.

The purposed implantable medical device consists of three main sections which work together aiming to deliver controlled stimulation to the targeted cells (Figure 3.2). The first section involves the power

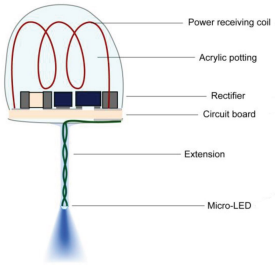

Figure 3.1: Montgomery et. al. wireless implant. Figure adapted from [55]

harvesting and converting system which, as the name points out, is responsible for collecting energy and making it available to be converted into light. This section includes a receiver coil, whose only function is to extract electromagnetic energy. The AC power provided is converted into direct current, ready to feed the second section of the device - the light delivery system. This section responsibility lies in delivering energy to selected cells in the form of photons, by extending the direct current to a μLED implanted at the site of excitation. It also includes a power sensing system aiming to provide feedback on light proprieties (useful for an open-loop system without feedback from cell response) and a sensing system for the purpose of monitoring of cell response to stimulation (useful for a closed-loop system). The feedback provided by the sensing systems is sent to a microcontroller, which works as the ”brain” of the implantable device and computes the necessary control actions for achieving a desired state. Finally, communication must occur between the implantable device and an external unit, enabling monitoring and control of the device. The communication section contains an antenna which could, eventually, be shared for both communications and power transmission.

Additionally, an external unit is essential for the operation of the implantable device. This includes a power source (come type of battery or charged storage) aiming to supply energy to the endoprosthesis, a power transmitter coil, a DC/AC converter for creating alternating current at a selected frequency (enabling the wireless energy transfer through electromagnetic induction), an antenna for communications and a power management, critical in optimizing and conserve the use of power. Figure 3.2 shows the medical device concept in a block diagram.

The optical endoprosthesis concept described and developed in this thesis should be taken as a first-stage prototype, aiming to test certain methods and their application in the context of therapeutics and regenerative medicine based on optogenetics. In engineering and technology, a rough prototype of a new idea is often constructed as a ”Proof of Concept” (PoC). The main purpose of developing a PoC is to demonstrate the functionality of our system and to verify certain methods and ideas that can be achieved during its development and that have practical potential. At an early stage of research, this thesis' primary focus is developing a PoC of an optical spinal endoprosthesis, aiming to identify the technological features necessary for its implementation in the real-world context, as a therapeutic and regenerative solution based on neurostimulation. A well-designed development framework enhances the ability to accomplish a more complete PoC, and therefore a more solid step into the evolution of an integrated working model with the end product as its final goal.

A solid reflection on the purpose of this thesis and the technology under study brings out areas

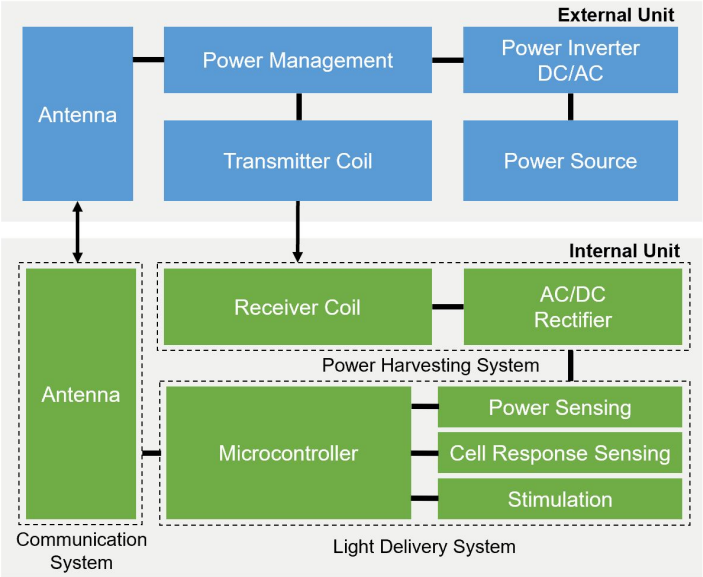

Figure 3.2: Implantable device and external unit.

which are easily identifiable and must be analyzed to create a valuable PoC: i) the design of the light control and delivery system and ii) the development of the energy harvesting and conversion system. Parallel to these, another area must be considered. The prosthesis under development is designed to apply a controlled input into selected cells, and thus generate a desired output. Thus, in order to be able to create an optimized output, there must be a solid understanding of this biological model, whose identification is the focus of the last main area to be explored. The framework for developing the device includes research which can be distributed through three different domains:

- **Light delivery system**, involving the selection and evaluation of LED models suitable for specific optogenetic actuators and the development of a light delivery control system. The former portion includes testing different LEDs and analyzing their inputs and outputs, as well as other relevant features, in order to build a solid understanding of light measurement methods and delivery processes. The latter focuses on regulating light properties, which ultimately condition cell response. This control system is to be implemented using an *Arduino Uno*.

- **Wireless power system**, section responsible for delivering energy to the light delivery system. In addition to the development of a rectifier circuit module, an electromagnetic induction system must be developed. The integration of both elements results in a wireless power system, essential to the endoprosthesis.

- ***In vitro* experiments** with living cells containing the optogenetic actuators, for both verifying the implant concept features and modelling the cell response to light. This phase involves laboratory work regarding the preparation of cells for *in vitro* experiments.

The framework under which this thesis was developed allowed to explore the available equipment in the Lisbon area and highlight essential technological features to be further refined and investigated

in the next stages of this ambitious project. The next chapters will go deeper into the several domains explored in this work.

3.2 Light Delivery System

Adequate light delivery is essential for the success of the optogenetic stimulation of targeted cells. Accordingly, the process of converting energy provided by the power harvesting system into photons as well as the correct regulation of the light supplied to the cells are critical functions of the system to be developed. In addition to these functions, correct localization of the LED at the site of excitation is essential for the success of neural activity modulation. In this chapter, the most crucial elements of the light delivery system are carefully analyzed and selected according to requirements dictated by the biological experiments planned.

3.2.1 Selection and Analysis of LEDs

As the name implies, the output of the optical spinal endoprosthesis object of this study is energy in the form of photons which, under certain conditions, enables cell activation. It has previously been pointed out that a light-emitting-diode (LED) is responsible for generating light and allowing optogenetic control. Therefore, correctly analyzing its main features and selecting the LED is a key factor for an adequate light delivery. As explained previously, as a PoC, the implant is not to be inserted on a living body, as the biological experiments are *in vitro*. For these reason the LED requirements for this optogenetic system are mostly related to the necessary conditions for optogenetic activation, meaning that size will not pose a restriction at this point. Two types of LED were prepared to incorporate the endoprosthesis, in order to activate either NpHR or miniSOG-targeted cells, both valuable tools for therapeutic and regenerative ends.

Light Requirements

An overview of the literature on this theme proved to be useful in collecting information about the operational light sensitivity of the potential optogenetic tools under study. From the different studies on NpHR (section 2.4) and miniSOG (section 2.5), two important parameters were collected: i) the light power density (i.e. amount of energy per unit of area) which the LED must be capable of providing to the cells to observe response, and ii) the light wavelength necessary for activation. The information collected is shown on Table 3.1.

	Activation Wavelength, λ	Light Power Density, mW/mm^2
eNpHR3.0	$589nm$	$5.4mW/mm^2$
miniSOG	$450nm$	$0.5mW/mm^2$

Table 3.1: Light requirements for activation of eNpHR3.0 and miniSOG

LED Selection

After evaluating light requirements, the next step involved obtaining readily available LEDs with these particular features. Using the lowest LED dimensions available would be a step closer to the medical device desired, as the target areas tend to be relatively small. The original strategy involved using similar LED chips to those used by Montgonmery et. al. as their dimensions have proven to be successful inside a living body (Figure 2.7). However, while the size of the LED did not pose a significant constraint for the biological systems we would use in our PoC, smaller LEDs were substantially more expensive. Thus, it was decided that, the size element could be initially sacrificed in the selection of LEDs, at least until we obtained a first impression of the limitations of our experimental setup. At this stage, two different LED models were selected, keeping their power rate and wavelength within an interval of required values. The features of both of them are presented on Table 3.2 and on Figure 3.3. Further, using a soldering iron, 30-gauge wires were soldered to the terminals of the LED, creating an extension which allows to deliver light to target regions. The extension can be bent to any desired angle and shortened to any desired length, depending on the target location of the nervous system.

	Blue	**Yellow**
Model	LD-MVSG	LYT67F
Dominant wavelength	455 nm	590 nm
Forward current (max)	30 mA	50 mA
Forward voltage	2.70 V (min) / 3.40 (max)	1.90 V (min) / 2.50 (max)
Viewing Angle	120°	120°
Package Type	SMD	SMD

Table 3.2: Blue and yellow LED features

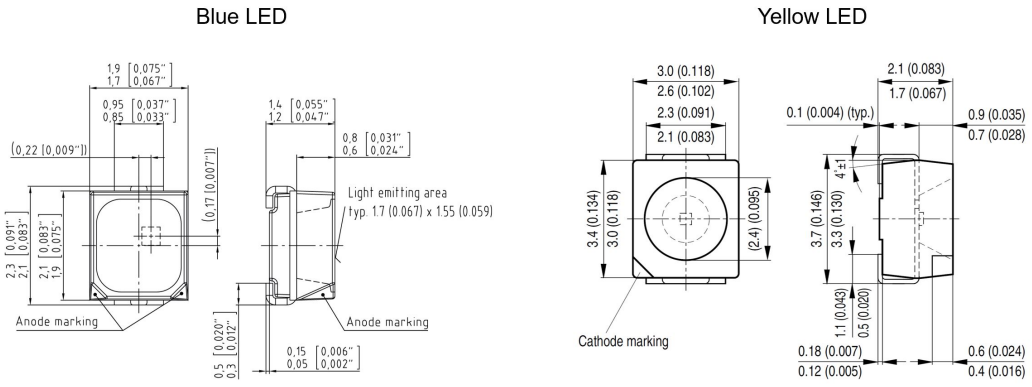

Figure 3.3: *Right:* Dimensional drawing of blue LED. *Left:* Dimensional drawing of yellow LED (dimensions in mm).

Analysis of Light Properties

In order to understand if both LED models satisfied the desired requirements, experiments for testing both their wavelength and irradiance were designed. A starting point for this analysis was to design of an experiment which would allow to quantify precisely the wavelength of the light emitted, a critical factor for the optogenetic modulation of cell activity. The experiment aimed to better understand the impact of the current variation in the wavelength of the light emitted by the LED. For this purpose, a

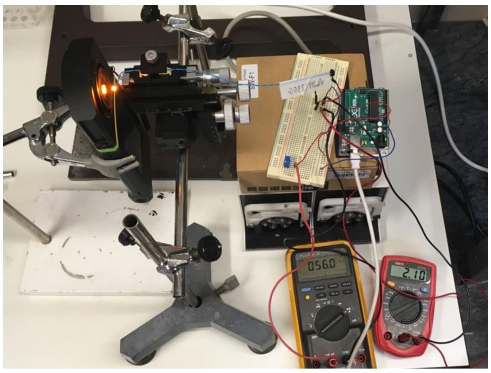

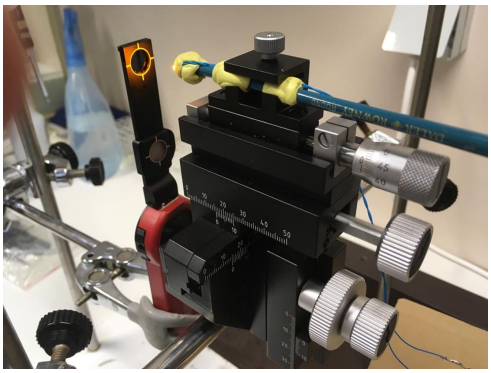

Figure 3.4: *Left:* Experimental set up for measuring LED light wavelength. *Right:* Experimental set up for measuring LED light power.

circuit (Figure 3.5) was developed to feed the LED, using an *Arduino* module as for supplying power. Adjusting the output voltage at the *Arduino* supply pin allowed to control the current supplied to the LED, assuming that the maximum forward current of each model should not be overcome (creating a top limit for the measurements). The measurement of the wavelength was obtained using a spectral color meter (UPRtek PG100N). Current was measured using a multi-meter (A in Figure 3.5). The experiment setup guaranteed that no motion occurred between the meter and the LED (Figure 3.4 *Left*).

Measurements were plotted against the current supplied and revealed an almost linear increase in wavelength as the current value increases for the yellow LED from 588 to 595 nm in the range of current values analyzed (Figure 3.6 *Right*). On the other hand, the wavelength of the light emitted by the blue led was stable up to 18 mA of current but then decreased from 458 to 451 as the current increased up to 30 mA (Figure 3.6 *Left*). These results not only provide precise knowledge of the wavelength at a certain current value, but they also establish known interval of current values to work with during the biological experiments.

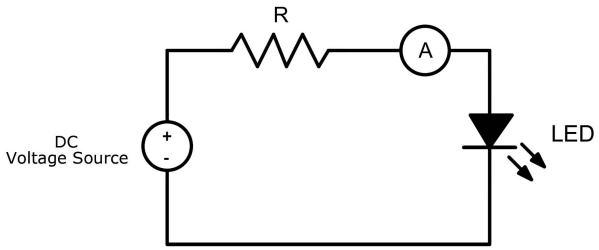

Figure 3.5: Circuit feeding LED for experimental evaluation of wavelength

Following the wavelength experiments, the irradiance power or light power density of the LEDs was put under test. The aim was to quantify the photon flux per unit of area (typically measured in mW/mm^2) that the LED was able to emit at a certain current value fed to it. A similar circuit to the wavelength test (Figure 3.5) was adopted as well as a similar procedure for adjusting the current. A power meter (Thorlabs PM160) was used to measure the light power. The experimental design attempted to guarantee that: i) no motion occurred between the meter and the LED (Figure 3.4 *Right*) and ii) the LED emitting face was attached to the meter, in order to measure the whole amount of photons emitted (considering that the amount of light escaping the meter was insignificant). The values obtained using the power meter (in Watts) were divided by the LED emitting area (LED emitting surface attached to meter surface

- ”zero distance”) to obtain the power density values. The results obtained were plotted against the current fed to the LED. We observed an increase in the current value leads to an almost linear increase in light power density, an outcome observed in both LED models (Figure 3.7).

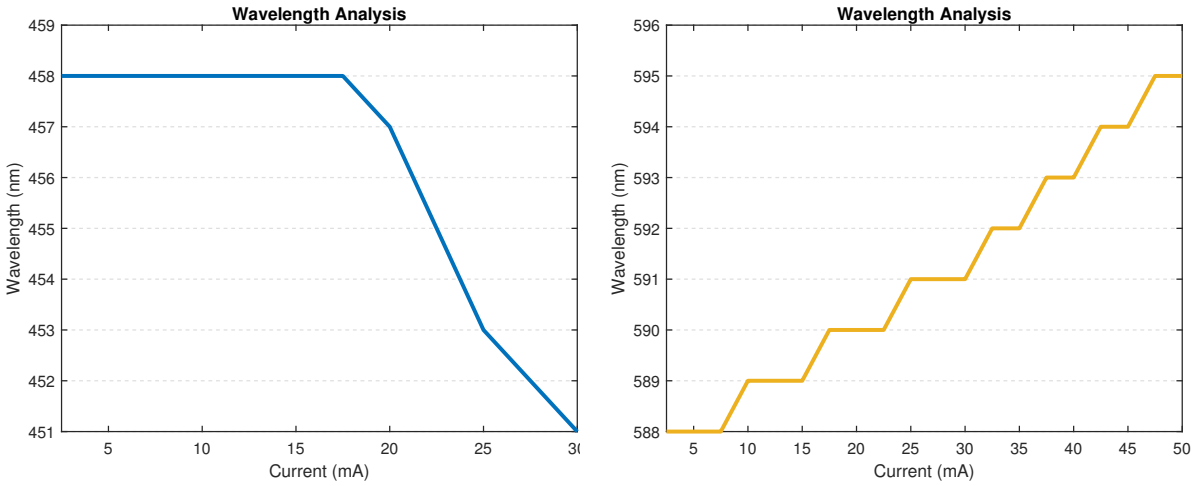

Figure 3.6: Dependence of wavelength on current value for the blue LED (left) and for yellow LED (right).

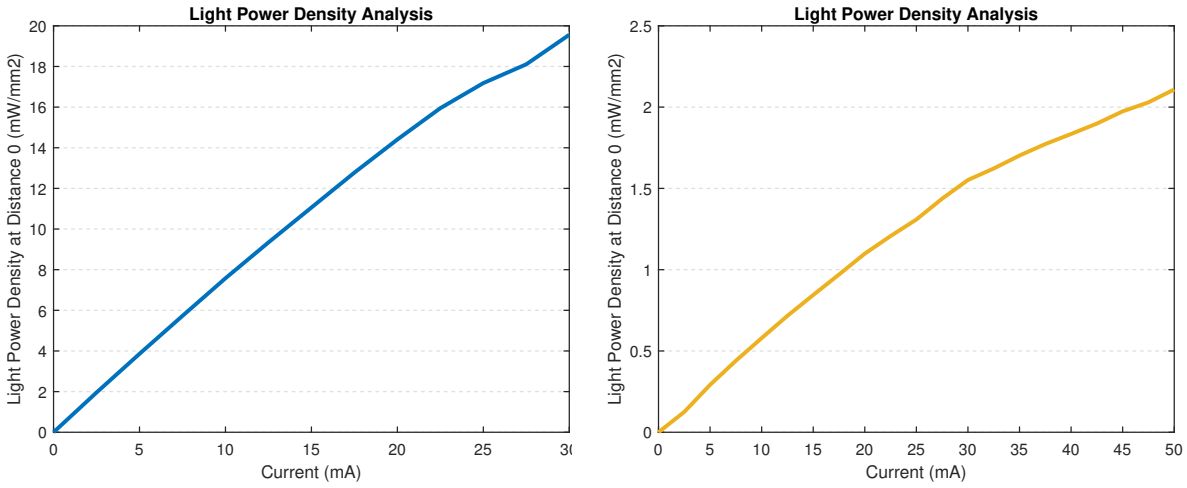

Figure 3.7: Dependence of light power density on current value for the blue LED (left) and for yellow LED (right).

These results provided precise knowledge of the light power density achievable at a certain current value at a surface positioned at the LED emitting face. However, this information is only valid in the event of achieving a complete attachment between the LED surface and the target cells. Though this is the most likely circumstance when placed inside a body, when it comes to the biological experiments carried out in this thesis, a complete attachment is highly unlikely. For that reason, a study of the distance impact on irradiance levels was carried out. The aim is to quantify the change of light power density within a relatively small range of distance. The same circuit from the two previous experiments was used (Figure 3.5). The light power density is assumed to be equivalent to the power measured at the ”zero distance” position divided by the area of the circle defined by the beam angle (Figure 3.8). It is also assumed that the light beam is originated in the intersection point of the *x y z* axis of the LED module (Figure 3.8).

The experiment described is a useful tool for characterizing the light power density dependence

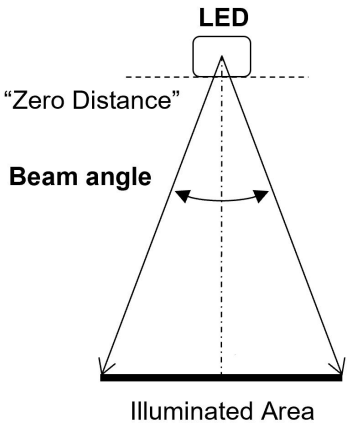

Figure 3.8: Representation of light power density calculation procedure

on distance from the light source and on the current value. The three-dimensional plots of Figure 3.9 show that the amount of energy delivered to the surface illuminated increases as the proximity of the detector to the source of light decreases, for both blue and yellow LEDs. Furthermore, light power density increases with the rise in current supplied to the LED.

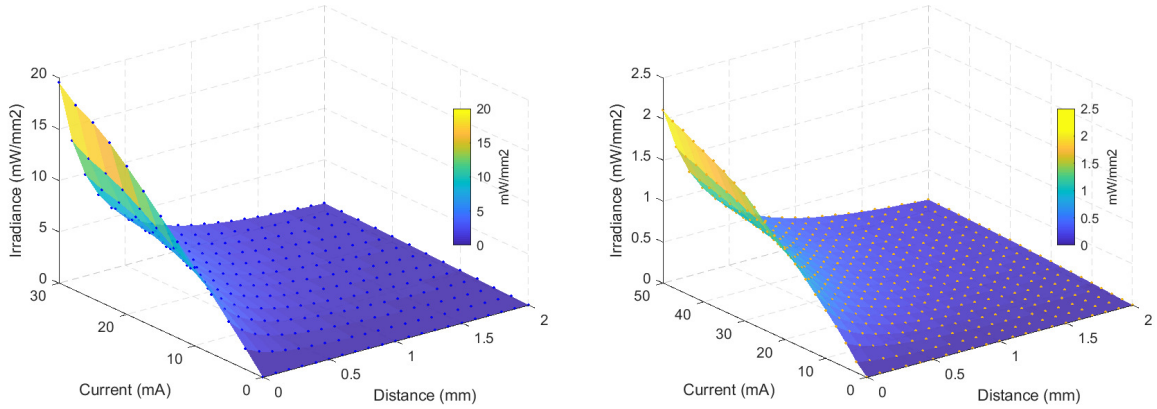

Figure 3.9: Dependence of light power density on current value and distance for the blue LED (left) and for yellow LED (right).

Light Delivery Efficiency

Considering the final purpose of this thesis, i.e. developing an optically-controlled endoprosthesis, the efficiency of the implant sub-systems and of the system as a whole must be analyzed. In this section, the optical excitation system efficiency will be studied, allowing for a clear understanding of the optimal performance parameters of both the LEDs models.

The light delivery efficiency is the energy conversion rate between the power fed to the diode and power effectively delivered to the cells. Thus, the data required for evaluating this parameter was obtained in previous experiments, namely the assessment of the light power density at ”zero distance” from the light source. The light delivery efficiency is the ratio of the measured energy delivered as light at a certain current value over the power supplied to the LED (current value multiplied by voltage across the

diode). The plots presented in Figure 3.21 illustrate the efficiency of both the yellow and blue LEDs.

Both LEDs show a decrease in efficiency as the current value increases. The blue LED shows a considerably higher value of efficiency with respect to the yellow LED. The concept of efficiency implies that the system dissipates some part of the energy in the process of conversion. Moreover, the local temperature of the cells or tissues, in the implant circumstance, could increase at optical stimulation sites because of photon absorption. This temperature increase may result in tissue damage or changes in neural activity that are not optogenetically driven.

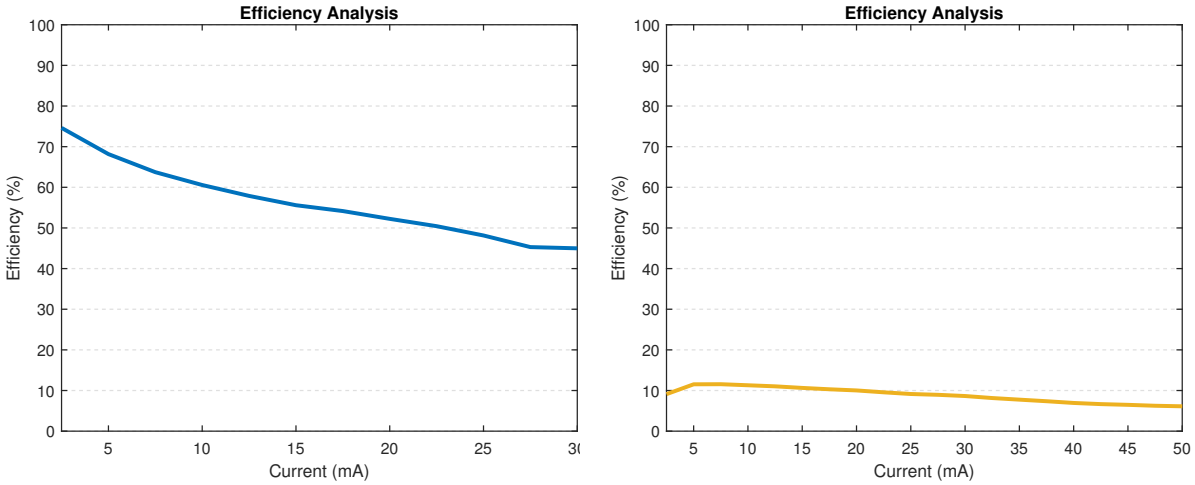

Figure 3.10: Efficiency of the blue LED (left) and yellow LED (right).

Evaluation of LED Models Analysis Outcome

Various requirements of light delivery system have been examined and two different LED models have been analysed. This battery of experiments allowed us to characterize the different sources of light and their capacity for meeting the requirements.

Previously reported experiments in literature (mentioned in section 2.5 and 2.4) have used wavelength values with a margin of 10 nm around the values mentioned in table 3.1. Thus, light wavelength of both models suits their purpose as their a maximum wavelength is within this margin. Although the blue LED selected (for miniSOG) has proven to meet the light power density specifications (2 mW/mm^2), the yellow LED (for NpHR) had a different outcome. The irradiance values obtained for this model are lower than the required ones (Figure 3.7 *Left*), meaning that it does not deliver enough photons to activate the optogenetic tool. By examining the LED datasheet, the maximum luminous intensity is 1400 mcd (1.4 cd). Candelas (cd) are photometric units, meaning they are weighted by a spectral luminous efficiency function, which represents the human eye's sensitivity to the light at a given wavelength. To convert between photometric and radiometric units (based on physical properties), one needs to know the spectral sensitivity factor V(λ), which follows a curve standardized by the CIE (Commission Internationale de l'Eclairage) [83]. Combining these with a photometric conversion factor Km, the radiant intensity (measured in watts per steradian, W/sr) can be obtained following Equation 3.1. Following the relationship between radiant intensity (I_e) and irradiance (E_e), stated in equation 3.2, at a distance

of 0.9 mm from the light source, imposed by the LED module (Figure 3.3 *Right*), the yellow LED light power density obtained is 3.3 mW/mm^2

$$I_e = \frac{I_v}{K_m V(589)} = \frac{1.4}{683 \times 0.757} = 2.7 \times 10^{-3} mW/sr \tag{3.1}$$

$$E_e = \frac{I_e}{d^2} = \frac{2.7 \times 10^{-3}}{0.9 \times 10^{-3}} = 3.3 mW/mm^2 \tag{3.2}$$

The light power density obtained from the datasheet information is relatively close to the one calculated in section 2.6. It is highly likely that the discrepancy between these values was originated in experimental errors of small magnitude. Using Equations 3.1 and 3.2, a required value for luminous intensity can be calculated, based on the optogenetic tool light activation requirements (Section 3.1). The new LED to be selected (positioned 1 mm from the targeted cells) would need a luminous intensity above 2792 mcd. A brief search in the LED models available in market suggests *Broadcom ASMT-SAB4-PW505* (3550 mcd) as a viable option to be acquired and tested in our system, in the event of using NpHR in future biological experiments to achieve and adequate level of light power density. The process followed in this work for analyzing the LED models can be followed for any other selected model and/or optogenetic tool, while taking into account their requirements.

3.2.2 Light Delivery Control System

The optogenetic concept involves neural activity control of cells through the use of light. In the case of the system to be developed in this thesis, this simple definition implies that the output of the LED, as light, is the input of the ultimate system to be controlled - the cells. Therefore, once an appropriate LED have been selected based on its features, manipulation of their activity is essential to the success of the developed optogenetic structure. The activity is measured by sensors, from which information is transferred and used by the controller to estimate the current state of the system. This estimation acts as input to algorithms responsible for determining the necessary control action to achieve a desired activity state. This input leads the control action to be carried out and the reaction of the system is, once more, measured by sensors, closing the loop.

The present section covers the development of the light delivery control system, from laying down the desired variables to be controlled to establishing the equipment and control methods to be used. The presented control system was developed using an *Arduino Uno* for both control and energy supply functions.

Controlled Variables

Correctly identifying the necessary variables of the light delivery system to be controlled is a key factor for achieving a successful manipulation of the output. As stated previously, light wavelength acts as a key to a certain optogenetic actuator and, therefore, it must be maintained inside a specific range of values. Moreover, delivering a known amount of energy to the cells, stated in the light power density

value, is essential to provide specific patterns of cells activity. Thus, controlling these two variables is crucial and sets the starting point of the light delivery control system development.

Following the analysis on the LED models and their output on section 3.2.1, one relevant parameter stands out due to its impact on both light power density and wavelength of light emitted - the current supplied to the LED. By actively controlling the latter the former two can also be regulated. The analysis conducted in section 3.2.1 are useful as guides for setting the parameters for light delivery and cells stimulation. In the event of needing a specific stimulation pattern of a certain irradiance power and light wavelength, the current value should be selected accordingly, by examining the above-mentioned models. Even though the light power density and light wavelength are tightly connected by the current value, as the latter determines the first two, light power density should be the first variable to be set, as the light wavelength excitation for a particular optogenetic tool is not an absolute value but a range of values. Thus, the only assurance required is that the current value results in an adequate wavelength. This matter should be considered during any biological experiments with optogenetically targeted cells.

Once the variable to be controlled is set, i.e the current value, a method for controlling it is required. In order to create a closed-loop system, two more elements are necessary: i) a sensor, responsible for creating a *feedback* and ii) a controller, in charge of comparing it with the current state of the controlled variable and establishing a new adequate input. As the present work follows a "Proof of Concept" strategy, the equipment selection relied on cost-effective alternatives. For this reason and due to its highly functional versatility, the task of controlling the desired variables was assigned to an *Arduino Uno*.

Current Feedback Sensor

Feedback sensors provide the control system with measurements of physical quantities necessary to close control loops. Usually, the performance of such control systems owes much to the quality of the feedback sensor. Therefore, selecting a sensor that provides a responsive, accurate, and low-noise feedback signal is essential to the well-functioning of the closed-loop system.

The INA219 (Figure 3.11) is a highly versatile device able to monitor both DC voltage and current. It is powered by 3 to 5 V and uses I2C protocol to establish the communication with the *Arduino*. The current measurement method used is the high side, where the shunt resistor is placed between the power supply and the load, allowing the device to measure both circulating current and voltage on the load. The INA219 can handle 0 to 26 V and uses a precision amplifier for measuring the voltage across the 0.1 ohm resistor. Since the amplifier maximum input difference is $\pm$ 320 mV this means it can measure up to $\pm$ 3.2 A. With the internal 12 bit ADC, the resolution at $\pm$ 3.2 A range is 0.8 mA. However, since we are measuring current value much below this range and the current variations are relatively small, this resolution is not precise enough to provide an adequate feedback. The INA219 provides an option of changing the internal gain, which, when set to the minimum vale, fixes the maximum current to $\pm$ 400 mA and the resolution is 0.1 mA.

When an electric current flows through the shunt resistor, a voltage following Ohm's law ($U = R \times I$) arises. By measuring the voltage and substitute the values in the equation, the current value is obtained.

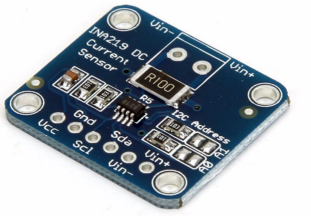

Figure 3.11: INA 219 breakout board.

The PWM Issue

As explained previously, for the purpose of carrying out the biological experiments, in addition to the current-controlling task, the *Arduino* is also responsible for supplying power to the LED circuit. This device, when connected to a computer, is capable of supplying up to 5 V. Thus, the control action carried out by the *Arduino* takes the form of bits, ranging from 0 to 255 which translates into an output voltage.

However, the *Arduino* digital pins either provide 5 V (when turned HIGH) or 0 V (when turned LOW). When a voltage value inside this interval is required, for example for dimming a LED, a technique of switching between the HIGH and LOW states fast enough enables a change in brightness. This technique is known as ”Pulse With Modulation” or PWM and is used by the *Arduino* for creating analog outputs with digital means in some of its pins (3, 5, 6, 9, 10 and 11). In case the output produced is 127 bits, a PWM with 50% duty cycle signal is generated, meaning the signal was high 50% of the time during a period of this signal. Even though the frequency of generated signal for most pins will be about 490Hz, this value can be increased to different values depending on the pin. The 5 and 6 pins can generate signals with a maximum frequency of 62.5kHz, allowing for faster corrections of the output.

When an electric current flows through the INA219 shunt resistor, a voltage following Ohm's law ($U = R \times I$) arises. By measuring the voltage and substituting the values in the equation, the current value is obtained. As Figure 3.12 demonstrates, this measurement is affected by the voltage fluctuation involved in the PWM technique. The sensor captures different frames of the signal period and consequently returns a feedback signal with a large variation, preventing a satisfactory performance of a close-loop system. For this reason, a transformation of the feedback signal must be carried out in order for it to be adequately read by the INA219.

A low pass filter is a circuit designed to reject all unwanted high frequencies of an electrical signal and accept only those signals wanted by the circuit designer. An ideal filter will pass input frequency signals from 0 Hz to its cut-off frequency point (*fc*) while blocking higher frequencies. In low frequency applications (up to 100kHz), passive filters are generally constructed using simple RC (Resistor-Capacitor) networks (Figure 3.13). In the circuit supplying energy to the LED, a passive RC low pass filter is applied in order to transform the PWM into a constant stable signal. Such signal can be appropriately sensed by the current sensor and integrated on a closed-loop. In this case, the priority is to suppress a particular frequency in the stop-band (the PWM signal frequency is 62.5kHz). On the other hand, an increase on the resistor and capacitance values, R and C respectively, contribute to a raise in the impedance, meaning that a less efficient system requires higher power supply (Equations 3.3- 3.5).

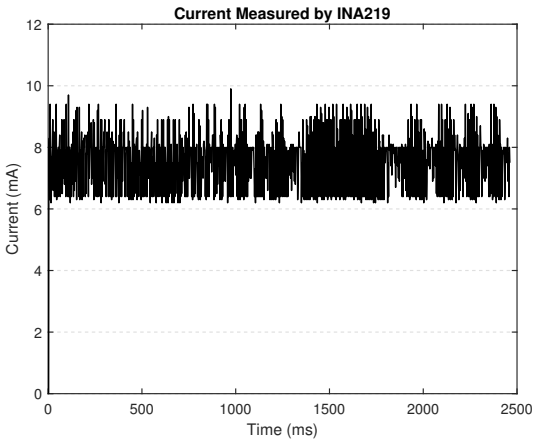

Figure 3.12: Poor INA219 current sensor readings (blue LED with voltage value equivalent to 123 bits).

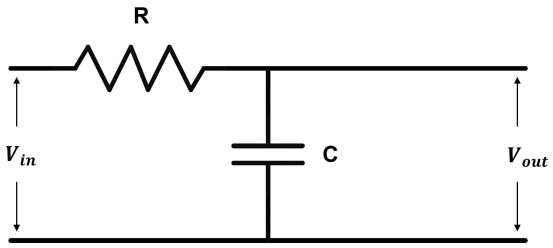

Figure 3.13: *Right:* RC filter circuit; *Left:* Representation RC filter effect and cut-off frequency.

$$Z = \sqrt{R^2 + X_C^2} \tag{3.3}$$

$$X_C = \frac{1}{2\pi f C} \tag{3.4}$$

$$V_{out} = V_{in} \frac{X_C}{Z} \tag{3.5}$$

The RC filter was designed following a ”trial and error” approach. The starting point was to choose a relatively small resistor value, R which has a higher contribution to the impedance value. Once the resistor was put in place in the circuit along with the INA219 and the LED, a stable voltage was supplied by the *Arduino* and the current flowing through the LED was observed. At this point, the capacitance value, C, was increased until the point where the variance was no longer significant and the signal was considered stable enough to be integrated in the control system. The final resistor and capacitance values are 3.3 Ω and 10 μF, respectively. The magnitude bode plot in figure 3.14 shows the frequency response of the RC filter to be nearly flat for low frequencies, resulting in a gain of nearly 1, until it reaches frequency values near the cut-off frequency (4.78 KHz). The frequency values above this value become greatly attenuated, i.e. they rapidly decrease. As expected, at 62.5 KHz the output signal is attenuated to 7.9% (Equation 3.6) with a gain of -22.08 dBs. Figure 3.15 illustrates the result signal capture by the INA219, clearly contrasting with Figure 3.12. Once the feedback signal has been carefully transformed and ready to be handled, a control system design is required to regulate light delivery properly.

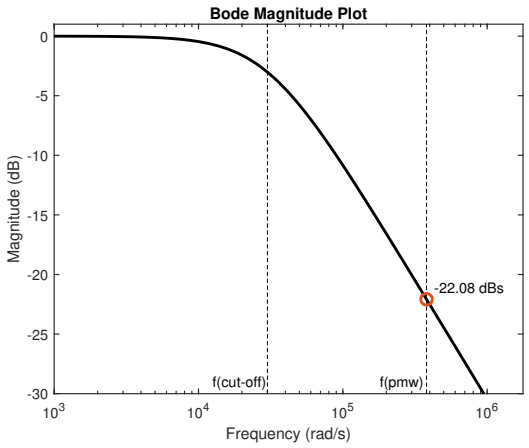

Figure 3.14: Frequency analysis of low-pass filter.

$$Gain = 20\log\frac{V_{out}}{V_{in}} \Leftrightarrow -22.08 = 20\log\frac{V_{out}}{V_{in}} \Leftrightarrow \frac{V_{out}}{V_{in}} = 0.079 \tag{3.6}$$

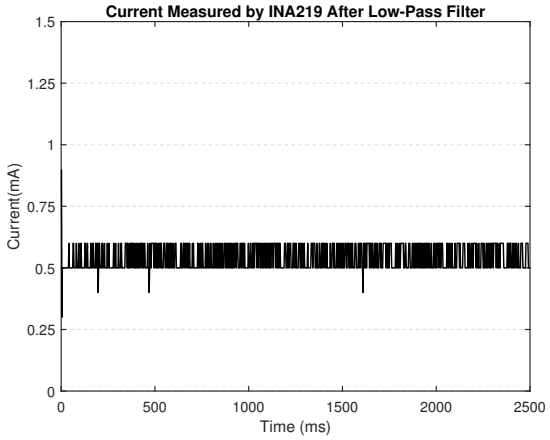

Figure 3.15: INA219 current sensor readings after implementation of RC filter in the circuit (Blue LED with voltage value equivalent to 123 bits)

PI Controller

The *Arduino* carries out the task of controlling the output of the LED. The INA219 sensor measures the current value - process variable (PV), which is compared with the desired state set by the operator setpoint (SP) and the result is analyzed by the controller, generating an adequate control action in the form of input voltage. The feedback line introduces the output of the system into the input. Thus, discrepancies between the PV and SP are measured and introduced to the controller as a new variable - the error, e. This error is the key variable used in a PID (Proportional-Integral-Derivative) controller, a type of compensation that can be applied to a system.

The PID controller consists of three parts which work independently. The proportional part deals with the current value of the error. The gain Kp is multiplied by the error term to generate an output which will work to minimize this error. However, in the case where the proportional action is moving to correct

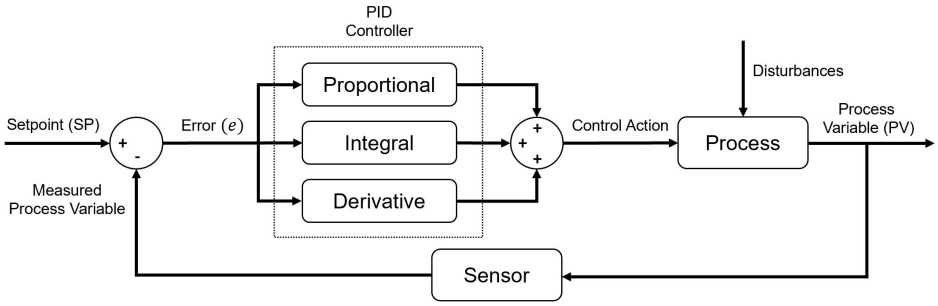

Figure 3.16: Block diagram of a process under PID control.

the error, as the actual value gets closer to the setpoint, the error is decreasing, causing an increasingly weak action of the proportional part. Since the proportional component only acts on the instantaneous error it never reaches the setpoint. This circumstance unfolds the importance of the integral component. This component is responsible for adding the past errors over time and multiplying the result by a Ki gain, helping the controller achieve its setpoint. On the other hand, the derivative component is based on a forward looking approach. It does so by estimating what the output will be from its change rate, resulting in an output multiplied by a Kd gain. In a situation where an actual value is heading towards the setpoint very quickly, the derivative part is implemented to prevent overshoots. The PID control thus considers past, present and future values of the error in assigning its control value (Equation 3.7).

$$u(t) = K_p e(t) + K_i \int_o^t e(t) + K_d \frac{\partial e(t)}{\partial t} \tag{3.7}$$

Despite the fact that the derivative element of the control strategy can improve performance, it only does so in specific situations. The derivative component acts mostly at fast, short-term changes in the process variable, which is very common in a noisy signal. Therefore, this tendency to act quickly ends up acting as a noise amplifier bringing excessive volatility to the system. Careful tuning of P and I gains can achieve much of the same no-overshoot benefit in certain conditions, and this is the main reason why the PI controller is so widespread. At first sight, for the present application, which requires the fastest possible response (light response should keep track of biological response), the derivative element appears to have a negative effect on the system. For that reason, the first approach for designing the controller will rely on a PI structure.

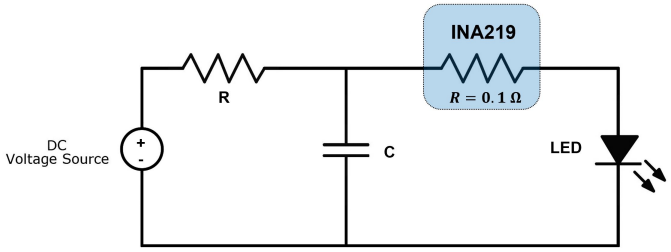

Figure 3.17: Circuit for LED current control using INA219 sensor

At this stage, it is useful to reexamine the components of the light delivery system (Figure 3.17). The

power is supplied by the *Arduino*, which is capable of delivering up to 5V. The resistor and capacitor form a low pass filter, responsible for delivering a stable current signal, which is sensed by the INA219. The INA219 then provides feedback to the *Arduino*. The LED comes after the sensor, and emits photons in charge of activating the optogenetic tool inside the cells. Naturally, the voltage at the LED terminals is an important value to take into consideration, as it is closely related to the current flowing through it. The desired current passing though the INA219 sensor (same as the one feeding the LED) is converted to a desired input voltage (SP) using the sensor resistance value. On the other hand, the voltage drop across the INA219 is proportional to the instantaneous current value and functions as a process variable (PV), playing a key role by completing the feedback system. Thus, the discrepancy between these desired input voltage and actual voltage drop across the INA219 formulates the error, which serves as an input for the PI controller. Finally, in an *Arduino* context, control actions take the form of changes in input bits (from 0 to 255) which are equivalent to changes in supplying voltage value (from 0 to 5V). From PI components from Equation 3.7, a control action (or PI output) for the j^{th} moment can be formulated and put into *Arduino* programming terms, as follows:

$$V_{PV}(bits)_j = I_{measured} * 0.1 * (255/5) \tag{3.8}$$

$$V_{SP}(bits)_j = I_{desired} * 0.1 * (255/5) \tag{3.9}$$

$$error_j(bits) = V_{SPj}(bits) - VPV_j(bits)_j \tag{3.10}$$

$$integral_j(bits) = integral_{j-1} + error_j \tag{3.11}$$

$$output_{(bits)} = K_p * error_j + K_i * integral_j \tag{3.12}$$

$$R_{INA219} = 0.1 \tag{3.13}$$

The following step involves determining the gain values for the PI controller (loop tuning), aiming to achieve a responsive and stable loop with minimal overshoot. These goals, especially the last two , tend to conflict with each other. A compromise between them must be found which acceptably satisfies the process requirements. There is a wide range of methods for loop tuning, some of which are highly sophisticated. Since the present process is relatively simple, the initial approach consisted on manual tuning, while observing the response to a step input, with a defined setpoint. Initially, the Ki gain was set to zero. Then, Kp was slowly increased until the system reaches a point where the output current starts having high amplitude oscillation and eventually settles close the required setpoint and continues to oscillate at a reasonably slow pace between amplitudes close to each other. Secondly, the Ki value was increased until the setpoint is reached and reasonable time response was achieved. The Kp and Ki were set to 1.25 and 80 respectively. After achieving a satisfactory PI controller design, the dynamic behavior of the closed-loop system was tested. The aim here was to vary the setpoint far enough and fast enough so that the dynamic character of the process could be revealed through the response of the measured process variable. For this purpose, the controller was put under a pulse test (Figure 3.18 *Left*). Moreover, the dynamic behavior of the system may differ depending on the operating range, so

several current value setpoints were considered on a step test (Figure 3.18 *Right*). The system has a rise time of 32 ms and a steady-state variance of 0.02.

The INA219 precision has proven to be adequate to provide feedback for the light delivery control system. Combining it with the designed RC filter allowed the feedback signal to be stable enough for the controller to use it properly. Moreover, the PI controller design proved to work successfully without the addition of a derivative component and the manual tuning method achieved satisfactory results.

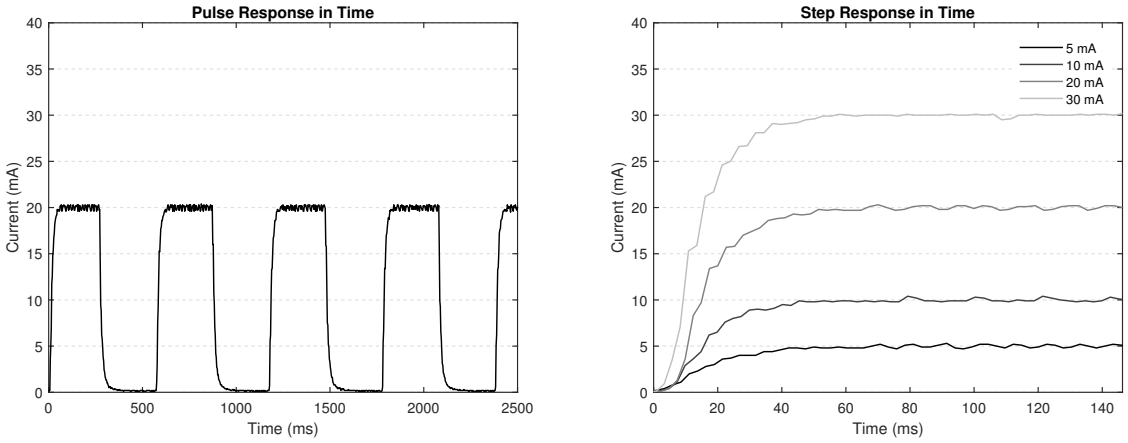

Figure 3.18: *Right:* Step response in time with several current setpoints.*Left:* Pulse response in time for 20 mA setpoint.

3.3 Wireless Power Transfer System

Following the requirements stated on section 3.1 and the growing trends towards wireless-powered solutions for optogenetic systems describe above (section 2.6), the PoC developed in this thesis focuses on formulating methods and further developing already existing solutions for providing power to the light delivery system.

The present section focuses on the study of wireless power transfer including the performance of inductive links at high frequency. A schematic of a purposed wireless power transfer system is provided, and its application on the endoprosthesis is analyzed, tapping the full potential of the system and proving to be a viable option for many low-power devices. Finally, we present and discuss a coil design as well as the simulations and experimental results which constitute the purposed system analysis.

3.3.1 Schematic of The Purposed Wireless Power Transfer System

In implantable biomedical devices, the inductively coupled wireless power transfer scheme is preferred to transcutaneous wires due to a number of advantages, such as miniaturization, robustness, reliability of the operation and ease of implantation.

Progressions in WPT designs are aimed to achieve maximum power transfer efficiency (PTE) through different layers for maintaining reliable operation of the implant. Resonant inductive coupling technique is built on the concept that the resonant objects are able to exchange energy effectively. The WTP system uses a transmitter-receiver (Tx-Rx) coil pair for inductive coupling at a specific resonant frequency, with

each coil being compensated by a capacitor to form a LC tank circuit with the same operating frequency. Therefore, the receiving coil is magnetically coupled to the transmitting coil, increasing the PTE. The Tx module is placed outside of the body while the Rx module is placed in vivo. Additionally, the received power at the Rx coil needs to be rectified in order to be fed to the LED. The rectifier converts the signal received by Rx coil into a DC supply voltage, ready to power the LED. On the way from the external power source to the implanted LED, there are various elements which represent sources of energy loss. Particularly in the WPT system, the transmitting coil, receiver coil and the various body tissue layers have an inherent resistance value which dissipate energy, leading to a decrease in the overall PTE value. The purposed wireless energy transfer system is developed based on a structure easily described by functional blocks, as shown by the diagram in Figure 3.19.

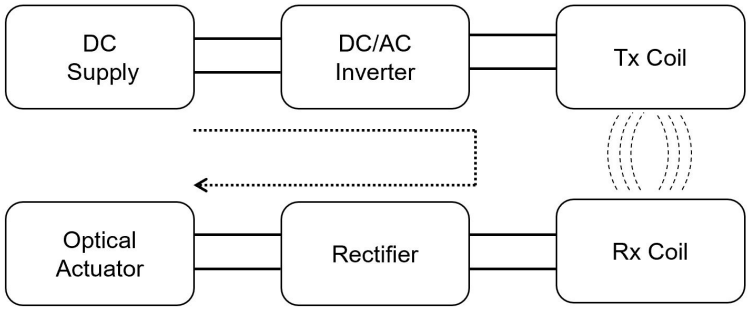

Figure 3.19: Block diagram of a wireless energy transfer system.

Progressing from left to right on the top line of the diagram, the input power to the system is a DC voltage directly from a battery or other DC supply, converted to AC. The transmitter coil uses the AC signal to create a change of magnetic flux which will eventually induce electromotive force to drive the target device. The AC signal received by the Rx is then rectified and fed into the LED. A schematic of a 2-coil WPT system is shown in Figure 3.20. Tx and Rx are the transmitter and receiver coil, respectively. C1 and C2 are the series resonant capacitors for the transmitting coil and receiving coil, respectively.

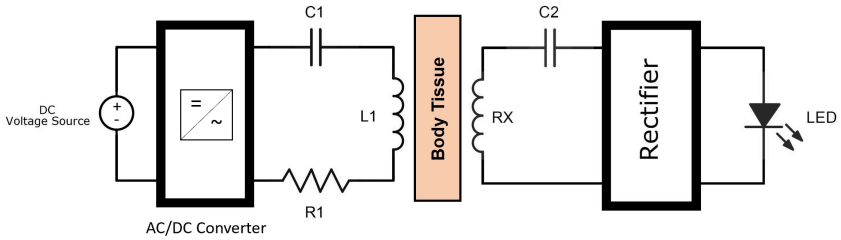

Figure 3.20: Circuit model of 2-coil WPT system.

Increasing the operating frequency to hundreds of MHz or a few GHz, enables the reduction of the diameter of the receiving coil to a few millimeters. For example, the diameter of the receiving coil used by Montgomery et. al. was reduced to 1.6 mm at an operating frequency of 1.5 GHz [55]. However, the high operating frequency proportionally increases the energy absorption in human tissues, causing adverse health issues. The safety limit for electromagnetic absorption in the body is defined as the

specific absorption rate (SAR) averaged over a certain mass of tissue. Excessive SAR can lead to an increase in tissue temperature and subsequent damage. In conductive tissues SAR is proportional to the operating frequency, and for circumstances involving human beings it is recommended to select an operating frequency under 20 MHz [84]. In order to reduce the risk of infection and improve the comfort of the patient, the size of the receiving coil should be minimized. Thus, the flat spiral-shaped coil type (Figure 3.24) is selected as the coil type in this study, due to its compact shape. This enables the whole coil to be attached to the skin surface on both the exterior and the interior of the body.

3.3.2 Rectifier Circuit

The wireless power system is built upon the process of collecting ambient electromagnetic energy which is converted into DC power by the rectifier. The amount of energy harvested is depended on the size of the receiver coil, among other factors. Consequently, a small size coil, implies a small amount of harvested energy.

The voltage multiplier is a type of diode rectifier circuit which can produce an output voltage many times greater than that of the applied input voltage. By using combinations of diodes and capacitors together, this input peak voltage is multiplied to give a DC output equal to a multiple of the peak voltage value of the AC input voltage. Therefore, this type of rectifier circuit enables the decrease in the necessary amount of harvested energy and the consequent decrease of Rx coil size. The device developed by Montgomery et al. included a two-stage voltage doubling circuit using Schottky diodes [55], which, as the name suggests, has a voltage multiplication factor of two. Due to a similarity between desired functionalities and energy-wise requirements, a similar type of rectifier circuit is applied in this study, using Schottky diodes (D1 to D4; 1N5817) and capacitors as shown in Figure 3.21. The first capacitor in series with the receiver coil (1.63 nF) was selected for being in resonance with the coil as explained the next section (3.3.3)

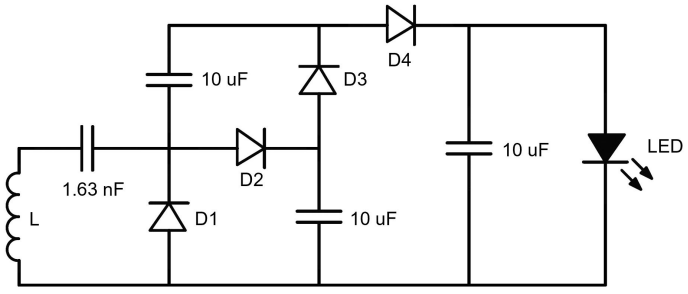

Figure 3.21: Rectifier circuit.

The selection of the components was assisted by a *Simulink* implementation of this circuit with and without LED. A signal generator (SFG-1013) substituted the coil as the AC power supplier, generating an input 3MHz sine wave. Various amplitude values were tested in order to observe the variation in the rectifier output which was equal to the voltage at the LED terminals. The experimental results as well as simulation results with and without LED are shown in Figure 3.22.

The use of a capacitor with a much smaller capacitance than the rest (1.63 nF $<<$ 10 uF) reduces

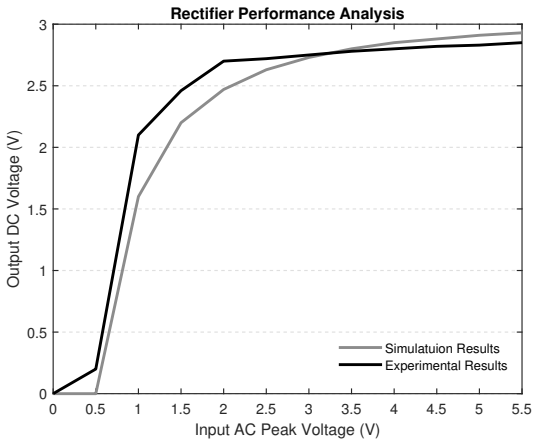

Figure 3.22: Experimental and simulation results of two-stage rectifier

the voltage multiplying capability of the two-stage rectifier. However, the developed rectifier circuit successfully contributed to a reduction in the amount of necessary harvested energy, generating an output voltage of $\sim 2.5V$ from an $\sim 1.5V$ input. On the other hand, maximizing the power transfer efficiency ensures that the energy harvest for a given receiver coil size is optimized and, therefore, the WPT system is reliable enough.

3.3.3 Resonant WPT System

In order to build up the mathematical model of the WPT system, the schematic diagram of the circuit shown in Figure 3.19 can be simplified to the equivalent simplified model as shown in Figure 3.23, where U is the output voltage signal of the AC/DC inverter. The rectifier and LED are treated as an equivalent load resistance R_L. In this simplified model, R1 and R2 are the parasitic resistance in the primary and secondary sides respectively, consisting of the resistance of the coils and the compensation capacitors. I1 and I2 are the current values for the primary and secondary sides, respectively.

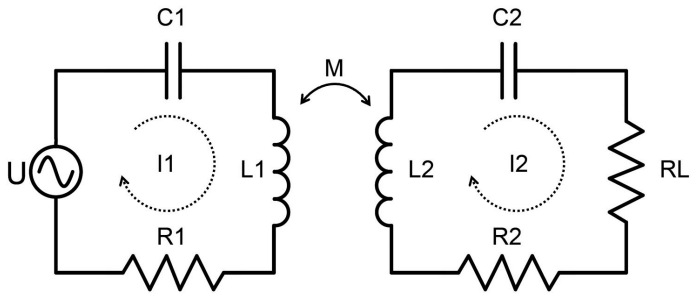

Figure 3.23: Simplified model of the WPT system.

For a resonant WPT system, the compensation capacitance is chosen to resonate with the self-inductance of the coil at a specific resonant angular frequency (ω_r) as Equations 3.14 and 3.15 describe:

$$C_1 = \frac{1}{\omega_r^2 L_1} \tag{3.14}$$

$$C_2 = \frac{1}{\omega_r^2 L_2} \tag{3.15}$$

According to the Kirchhoff voltage law, the WPT system can be expressed in the matrix as follows:

$$\begin{bmatrix} U \\ 0 \end{bmatrix} = \begin{bmatrix} Z_1 & -j\omega_d M \\ j\omega_d M & Z_2 \end{bmatrix} \begin{bmatrix} I_1 \\ I_2 \end{bmatrix} \tag{3.16}$$

where $Z_1 = R_1 + j\omega_d L_1 - j/(\omega_d C_1)$ is the impedance of the primary side, $Z_2 = R_2 + R_L + j\omega_d L_2 - j/(\omega_d C_2)$ is the impedance of the secondary side and ω_d is the driving angular frequency. From matrix 3.16, I_1 and I_2 can be derived as follows:

$$I_1 = \frac{Z_2 U_1}{\omega_d^2 M^2 + Z_1 Z_2} \tag{3.17}$$

$$I_2 = \frac{-j\omega_d M U}{\omega_d^2 M^2 + Z_1 Z_2} \tag{3.18}$$

Under resonant conditions, that is, when the driving frequency equals the resonant frequency ($f_d = f_r$), the impedance of the primary and secondary sides Z_1 and Z_2 are both purely resistant, which means that the currents flowing in the primary side I_1 is in phase U (the imaginary component of the impedance equals zero), and the current flowing in the secondary side I_2 is in phase with the input voltage of the rectifier.

The power transferred from the primary side, the power received by the secondary side (rectifier input power) and the power transfer efficiency (PTE) can be expressed as Equations 3.19 to 3.21, respectively, under resonant conditions:

$$P_{primary} = U_1 I_1 = \frac{U_1^2 (R_2 + R_L)}{\omega_r^2 M^2 + R_1 (R_2 + R_L)} \tag{3.19}$$

$$P_{secondary} = I_2^2 R_L = \frac{w_r^2 M^2 U_1^2 R_L}{(\omega_r^2 M^2 + R_1 (R_2 + R_L))^2} \tag{3.20}$$

$$PTE = \frac{P_{primary}}{P_{secondary}} = \frac{R_L (\omega_r M)^2}{(R_2 + R_L)[R_1 (R_2 + R_L) + (\omega_r M)^2]} \tag{3.21}$$

3.3.4 Optimized Design of Coils

Efficient operation of a wireless power transfer system is a major design challenge. The design of transmitter and receiver coils plays a critical role in WPT systems, and its optimization is crucial to reduce energy losses. The power transfer efficiency is a key performance index and, hence, it is used

as a figure of merit in this optimization process.

Considering Equation 3.21, it is clear that the larger the mutual inductance (M) is, the higher the coil-system efficiency will be. On the other hand, a larger coil parasitic resistance means a lower coil-system efficiency. Thus, the wireless power transfer efficiency can be effectively improved by increasing the mutual inductance with the same coils (or the coupling coefficient, k), decreasing coil parasitic resistance or increasing the self-inductance (increasing coil quality factor, Q) while keeping the same coupling coefficient. This improvement can be achieved by optimizing the design of the transmitter and receiver coils as those coil-system physical parameters are closely related to the structure of the coils. Q_{Rx}, Q_{Tx} and k are subject of optimization in the design process in this chapter, contributing to an improvement at the PTE level.

Coil Parameters

Developing a high performance WPT becomes challenging due to the application of specific design limitations associated with the environment in which the system is to be inserted. In this thesis these constraints are related with coil geometry and overall system size. Operation frequency also constitutes a constraint for designing the WPT system and was set to 3 MHz. Figure 3.24 shows the geometry of the spiral shaped Tx and Rx coils.

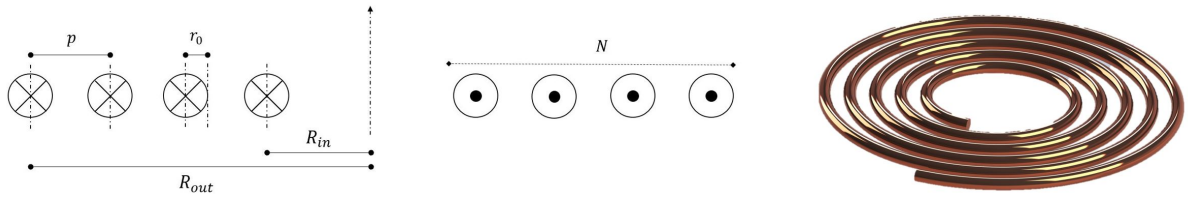

Figure 3.24: Left: design parameters of planar spiral coil (section view). Right: flat spiral coil.

R_{out} is the outer radius, r_o is the wire radius p is the pitch, and N is the number of turns. The separation distance between Tx and Rx is defined by d. Coils are assumed to be perfectly aligned. Design constraints for the WPT system are shown in Table 3.3.

Parameter	Value (mm)
Rx outer radius, $R_{Rx_{out}}$	20
Tx maximum outer radius, , $R_{Tx_{out}max}$	30
Rx wire radius, r_{Rx_0}	0.25
Tx wire radius, r_{Tx_0}	0.25
Distance between Rx and Tx, d	10

Table 3.3: Rx and Tx coil geometry constraints.

Inductance

The self-inductance for flat, spiral coils is shown in equation 3.22. L is derived from a modification of Wheeler's formula for a single-layer helical coil, while accounting for the conversion from inches to meters ($39.37\frac{in}{m}$) and μH to H [85].

$$L = \frac{N^2(2R_{out} - Np)^2}{16R_{out} + 28Np} \times \frac{39.37}{10^6} \tag{3.22}$$

The inductance expression is validated in prior work for a wide variety of coils and found to be accurate for most geometries, excepting when the coil has very few turns and when the pitch is very large relative to the wire diameter ($p >> 2r_o$).

AC Resistance

For spiral coils, the parameter that contributes most to fluctuations in total resistance R_{AC} is the pitch p. Because of the proximity effect, R_{AC} is inversely proportional to p, and this effect is nonlinear. For tightly wound coils, accurate expressions for R_{prox} are complex and can be difficult to calculate. However, Zeng et. al. [84] observed that R_{prox} has little variation when the pitch value is greater than 2.5 times the wire diameter and can be expressed by equation 3.25. In addition to this, under high frequencies, the current is confined to the surface of the wire, causing the skin effect. It is observed that the current density is rationally symmetric. With a sufficiently high operating frequency and the radius of the wire, r_0, being larger than the skin depth, δ, the representation of R_{AC}, is given as follows:

$$R_{AC} = l(R_{skin} + R_{prox}) \tag{3.23}$$

$$R_{skin} = R_{DC}(\frac{1}{4} + \frac{r_0}{2\delta} + \frac{3}{32}\frac{\delta}{r_0}) \tag{3.24}$$

$$R_{prox} = \frac{2}{\pi 2r_0\sqrt{1 - (2r_0/p)^2}}\sqrt{\pi\mu_0 f\rho} \tag{3.25}$$

$$R_{DC} = \frac{1}{\sigma\pi r_0^2} \tag{3.26}$$

$$l = \pi N(R_{out} + R_{in}) \tag{3.27}$$

where l is the length of the wire used for the circular flat spiral coil,f is the operating frequency μ_0 is the permeability of free space, ρ is the resistivity and σ is the conductivity of the conductor, and r_0 is the radius of the wire, respectively.

Quality Factor

The quality factor is determined by the coil inductance (L), AC resistance (R_{AC}) and operating angular frequency ω as equation 3.28 describes.

$$Q = \frac{wL}{R_{AC}} \tag{3.28}$$

Mutual Inductance and Coupling Coefficient

The amount of magnetic flux generated by the Tx coil which passes through the Rx coil determines M. Typically M depends on the geometries of each coil, the distance between them, and their relative orientation. For perfectly aligned coils, mutual inductance and coupling coefficient, k can be calculated as follows:

$$m_{i,j} = \left(\frac{4R_{TXi}R_{RXj}}{(R_{TXi} + R_{RXj})^2 + d^2} \right)^{\frac{1}{2}} \tag{3.29}$$

$$G(m_{i,j}) = \left(\frac{2}{m_{i,j}} - m_{i,j} \right) K(m_{i,j}) - \frac{2}{m_{i,j}} E(m_{i,j}) \tag{3.30}$$

$$M_{i,j} = \mu_0 \sqrt{R_{TXi}R_{RXj}} G(m_{i,j}) \tag{3.31}$$

M_{ij} is the mutual inductance between i^{th} Tx loop with R_{txi} radius and j^{th} Rx loop with R_{rxj} radius. The distance between i^{th} and j^{th} loops is d (constant for all loops). Total number of turns in Tx and Rx coils are N_{tx} and N_{rx}. $K(m)$ and $E(m)$ are complete elliptic integrals of first and second order respectively. The coupling coefficient, k, can be determined by the total mutual inductance (M), T_x coil inductance (Ltx) and Rx coil inductance (L_{rx}) as follows:

$$M = \sum_{i=1}^{N_{Tx}} \sum_{j=1}^{N_{Rx}} M_{i,j} \tag{3.32}$$

$$k = \frac{M}{\sqrt{L_{Tx}L_{Rx}}} \tag{3.33}$$

Optimization Process

As stated previously, coil geometry is subject to optimization, aiming to achieve a maximum value of power transfer efficiency, and considering a few constraints presented on Table 3.3.

The starting point of the optimization process is determining the design constraints, which were already summarized in section 3.3.4. The second step consists in designing the Rx coil for a maximum value of Q_{Rx}. Here L_{Rx} is calculated as in equation 3.22 and the combination of N_{Rx} and p_{Rx} offering the highest value of Q_{Rx} is selected, as presented in expression 3.34 and 3.35.

$$N_{Rx} = N_{Rx}[max(Q_{Rx})] \tag{3.34}$$

$$p_{Rx} = p_{Rx}[max(Q_{Rx})] \tag{3.35}$$

The next step involves estimating the performance of the system including a transmitter coil with a given value of $R_{out_{Tx}}$. Repeating the process indicated in equation 3.34 and 3.35, the combination of N_{tx} and p_{tx} offering the highest value of Q_{Tx} is selected (equations 3.36 and 3.37). The calculated

geometry parameters are then used to calculate the coupling coefficient, k, as in Equations 3.32 adn 3.33 . Q_{Rx}, Q_{Tx}, k are used to calculate the PTE value, following Expression 3.21.

$$N_{Tx_{[Rout]}} = N_{Tx_{[Rout]}}[max(Q_{Tx})] \tag{3.36}$$

$$p_{Tx_{[Rout]}} = p_{Tx_{[Rout]}}[max(Q_{Tx})] \tag{3.37}$$

Finally, the value $R_{out_{Tx}}$ is substituted and the process is repeated until the maximum value of $R_{out_{Tx}}$ is achieved. This enables the observation of the evolution of the PTE value when increasing the $R_{out_{Tx}}$. The best $R_{out_{Tx}}$ is selected based on the PTE value it offers (Expression 3.38 and Equation 3.21). Consequently, a Tx geometry corresponding to the best $R_{out_{Tx}}$ is chosen.

$$R_{out_{Tx}} = R_{out_{Tx}}[max(PTE)] \tag{3.38}$$

The overall optimization process can be summarized as illustrated in the flow chart in Figure 3.25.

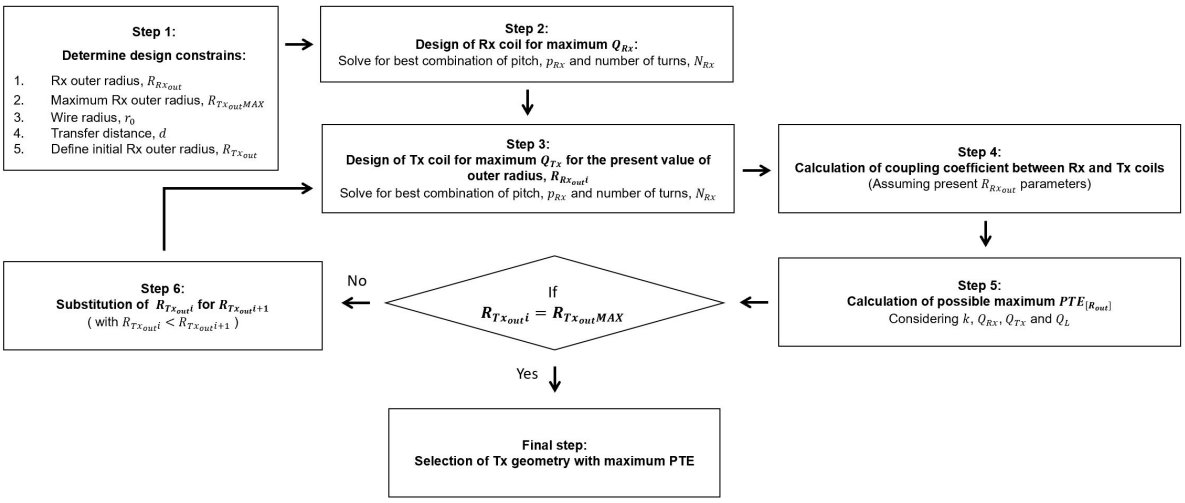

Figure 3.25: Design steps for purposed WTP system.

3.3.5 Experimental Setup for WPT System Validation

For the purpose of experimentally verifying the developed wireless power transfer system, a 3D printed structure (Figure 3.26) was designed so as to guarantee the alignment and desired distance between coils. This device also allows the setting of any desired distance and can be used for further experimental tests with different parameters. The face of each plate contains a bas-relief of the coil geometry guaranteeing the desired pitch value, number of turns and outer radius.

The experimental set-up is shown in Figure 3.26. The circuit presented in Figure 3.27 was used to evaluate the performance of the WPT system. A signal generator (SFG-1013) is used as a power supply to the primary circuit and the voltage across the load resistor is measured using an oscilloscope

(TDS5034B). The plates holding the coils were set 10 mm apart (section 3.3.4). Following Equations 3.39 to 3.41, the PTE of the system can be obtained by measuring AC voltage U_{in} (V1), the voltage drop at the primary resistor, U_{R_1} ($R_1 = 3.33$) and the voltage drop at a load resistance, U_L (V2) ($R_L = 100$), as shown in Figure 3.27. This process was repeated for various values of operating frequency with and without a body tissue phantom placed between coils.

$$PTE(\%) = \frac{U_L I_L}{U_{in} I_{in}} \tag{3.39}$$

$$I_L = \frac{U_L}{R_L} \tag{3.40}$$

$$I_{in} = \frac{U_{R_1}}{R_1} \tag{3.41}$$

Figure 3.26: *Left:* 3D printed coil holding structure. *Right:* Experimental set-up.

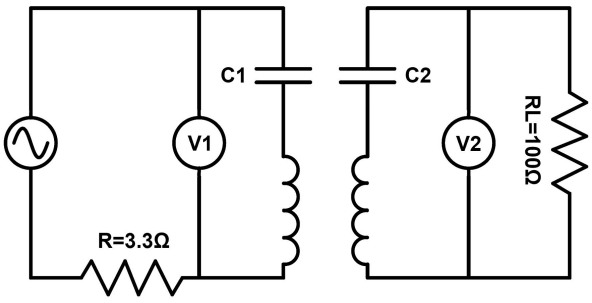

Figure 3.27: Circuit used to evaluate performance of wireless power transfer system.

3.4 In Vitro Experiments

After developing a functional light delivery system and a wireless power transfer system capable of supplying the necessary energy for guaranteeing the operational success of the optical endoprosthesis, a Proof-of-Concept workflow demands an experimental stage which, in the present work, translates into *in vitro* experiments with cells containing optogenetic actuators. These experiments aim at verifying the implant concept features and observing cell response to light. This project stage involved laboratory

work regarding the preparation of cells for the experiments as well as adaptation of the methods for achieving cell response to light. The following section explores the methods involving laboratory work. The purposed *in vitro* experiments explored the behaviour of HeLa cells, transfected with a miniSOG plasmid in order to express this functional optogenetic protein. Cell observation was undertaken with a Leica DMI6000B microscope.

3.4.1 Transfection Procedure

Transfection is the process of artificially introducing nucleic acids into eukaryotic cells (which possess a membrane-bound nucleus). The ultimate goal of transfection in this work is to deliver nucleic acids into living cells so as to achieve protein expression using their own machinery. This can be achieved, among other methods, by using chemical transfection reagents in which reagents rely on electrostatic interactions to bind with nucleic acids and to target cell membranes.

jetPRIME® is a cationic polymer-based molecule which forms positively charged complexes with plasmid DNA. The polymer-DNA complexes penetrate the cell through endocytosis. Plasmid DNA is then released from the endosomes in the cytosol via the proton sponge mechanism. Subsequent nuclear import of plasmid DNA is mainly achieved once the nuclear envelope disappears during mitosis [86] (Figure 3.28).

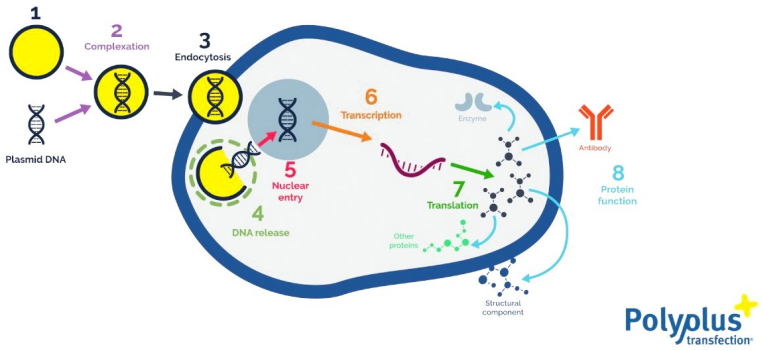

Figure 3.28: Illustration of chemical transfection process using jetPrime®. Figure retrieved from [86]

In the present work, the transfection process was applied to HeLa cells using jetPRIME® reagent. The transfection followed the protocol recommended by manufactures (Figure 3.28), with a ratio of $1\mu g$ of miniSOG plasmid per $3\mu L$ of jetPRIME® reagent and $300\mu L$ of jetPRIME® buffer. The mixture was added to HeLa cell cultures on $35mm$ glass-bottom dishes.

3.4.2 Photo Illumination

LED Positioning Issue

Twenty-four hours after transfection, cells were exposed to the blue light ($6mW/mm^2$ at $450nm$) from the microscope in order to confirm the existence of miniSOG in genetically targeted HeLa cells. After the confirmation was completed, the microscope lamp was turned off so that the only element supplying light to the cells was the blue LED.

The LED setup (section 2.6) was positioned as shown in Figure 3.29. The LED was sealed with a transparent layer of impermeable biocompatible PDMS, enabling the positioning of the LED against the cells at the bottom of the dish and inside the liquid culture medium. The LED was then turned on and the cells were irradiated with its blue light ($2mW/mm^2$ at $450nm$). However, the image captured did not contain green fluorescence from the transfected cells. Instead, the image contained the whole amount of cells in culture, as it happens when the microscope is capturing all transmitted light (Figure 3.30 *Left*).

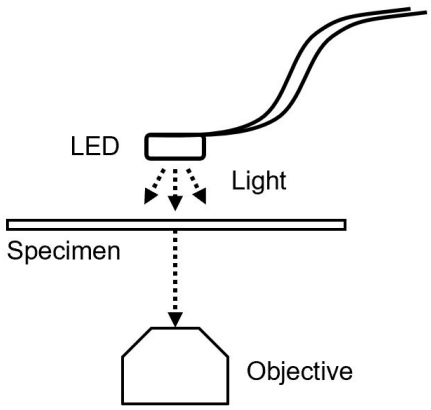

Figure 3.29: LED position in *in vitro experiment*

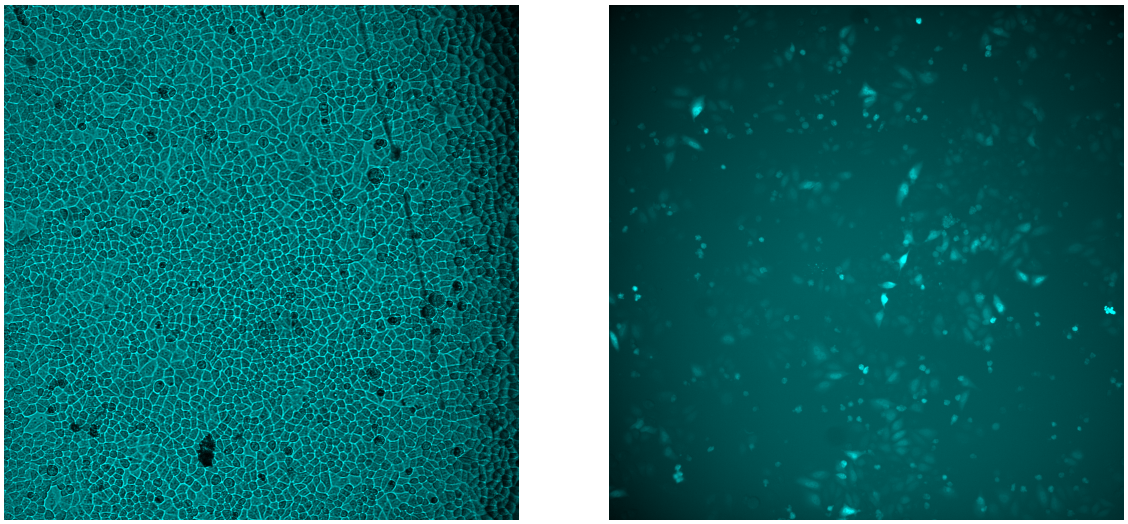

Figure 3.30: *Left:* Transmission light microscopy of HeLa cells, using LED light source. *Right:* Fluorescence light microscopy of HeLa cells, using microscope excitation light (450 nm).

Transmitted light observation is the general term used for the type of microscopy observation where the light is transmitted from a source on the opposite side of the specimen. This illuminates and produces a magnified image of a sample (Figure 3.31 *Left*). On the other hand, when trying to capture fluorescence (which is the case of the present work), a light source positioned on the same side as the objective, excites a fluorescent species in a sample of interest. This fluorescent species in turn emits a lower energy light that produces the magnified image instead of the original light source (Figure 3.31 *Right*). Thus, setting the LED on the opposite side of the objective regarding the specimen, resulted in capturing the transmitted light instead of the desired fluorescence (Figure 3.30 Right). A number of pos-

sible solutions to this issue were tested, including positioning the LED with different angles regarding the dish bottom. However, the transmitted light issue was persistent. For this reason, the microscope excitation light was used in the *in vitro* experiments, using the same light power density and light wavelength values as those provided by the LED system (section 2.6).

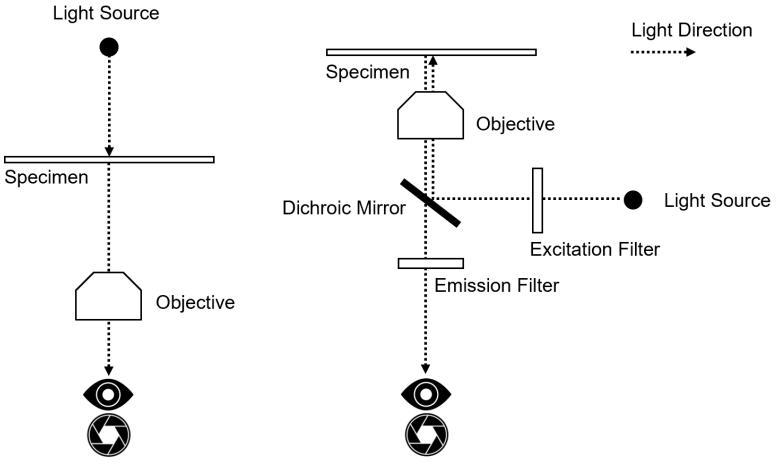

Figure 3.31: *Left:* Illustration of transmitted light microscopy light path; *Right:* Illustration of fluorescence light microscopy light path.

Microscope Light Power Density Mapping

In order to correctly analyze cell behaviour when excited by blue light, it is necessary to quantify light power density of the excitation light emitted by the DMI6000B, and we did it by means of a procedure analogue to that applied to the LED for the purpose of measuring its irradiance dependence on current values. The intensity of excitation light is controllable through the *Leica LAS X* software, with 6 intensity values available: 0%, 10%, 17%, 33%, 55% and 100%. Using the optical power meter PM160 (as in section 2.6), the excitation light power was measured 5 times at the output of the lens for each intensity value and the average was calculated. Afterwards, a paper was placed at the same distance from the objective as the cell culture dish and two points were drawn on opposite sides of the light circle project by the excitation light, for the purpose of measuring its diameter (Figure 3.32 *Left*). After taking 5 measurements, the paper was put under the microscope lens and the distance between corresponding points was measured using *Fiji* software. The resulting values were averaged and used to calculate the projected area, which was later used to calculate the light power density of the excitation light. The values were plotted against the intensity percentage as shown in Figure 3.32 *Right*.

3.4.3 Imaging and Fluorescence Quantification

For fluorescence imaging of HeLa cells, a Leica DMI6000b widefield microscope with a HC PLANAPO 10x, 0.4 NA objective with a sCMOS Hamamatsu Flash4 camera was used. Acquisition of images and adjustment of their brightness and contrast, were performed using *Leica LAS X* software. *Fiji* software was used for analysis and quantification of fluorescence [87]. Cell grey value was divided by the nearby

background grey value and the ratio was used to measure and compare fluorescence gradient values.

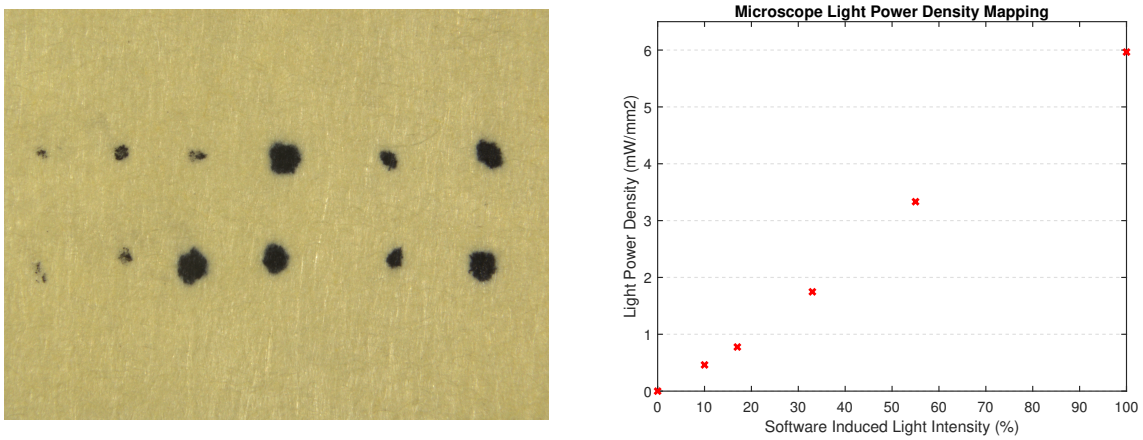

Figure 3.32: *Left:* Microscope observation of points used to measure the diameter of the illuminated circle. *Right:* Microscope excitation light power density mapping

3.4.4 System Identification Models and Evaluation Criteria

A wide variety of parametric model structures, also known as black-box models, provide assistance in modelling an unknown system. These models describe systems in terms of differential equations and transfer functions, providing insight into the system physics and dynamics. The general polynomial model (Equation 3.42; Figure 3.33) provides varying levels of flexibility for modeling the dynamics and noise characteristics.

$$A(z^{-1})y(t) = \frac{B(z^{-1})}{F(z^{-1})}u(t - n_k) + \frac{C(z^{-1})}{D(z^{-1})}e(t) \tag{3.42}$$

Where $u(n)$ and $y(n)$ are the input and output of the system, respectively, $e(n)$ is zero-mean white noise or the disturbance of the system and z^{-1} is a time-shift operator. By setting one or more of A(q), B(q), C(q) or D(q) polynomials equal to 1, it is possible to create different model structures [88]. In order to determine the structure which best models cell response to light, we tested different alternatives and evaluate their performance. ARX, ARMAX and OE and BJ structures were analyzed.

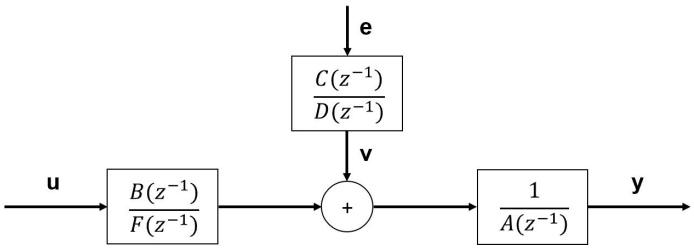

Figure 3.33: General Model Structure

ARX

The autoregressive model with exogenous input (ARX) is the simplest model that incorporates the system input signal and noise. In this model structure, the dynamics of the noise and the system are not independent ($C(z^{-1})$, $D(z^{-1})$ and $F(z^{-1})$ are 1). It is usually represented by $ARX(n_a, n_b, n_k)$, where n_a is the number of poles, n_b is the number of zeros and n_k is the pure time-delay of the system. This structure is represented by the following polynomial equation:

$$y(t) = \frac{B(z^{-1})}{A(z^{-1})}u(t - n_k) + \frac{1}{A(z^{-1})}e(t) \tag{3.43}$$

ARMAX

The autoregressive moving average model (ARMAX) considers that the noise dynamics contains a moving average component in addition to the dynamics of the system ($D(z^{-1})$ and $F(z^{-1})$ are 1). The ARMAX model has more flexibility in the handling of disturbance modeling than the ARX model. It is usually represented by $ARMAX(n_a, n_b, n_c, n_k)$, where n_a is the number of poles, n_b is the number of zeros, n_c is the order of the MA dynamics of the noise and n_k is the pure time-delay of the system. It is given by the following polynomial equation:

$$y(t) = \frac{B(z^{-1})}{A(z^{-1})}u(t - n_k) + \frac{C(z^{-1})}{A(z^{-1})}e(t) \tag{3.44}$$

Output-Error

The OE model describes the system dynamics separately, as no parameters are used for modelling the disturbance ($A(z^{-1})$, $C(z^{-1})$ and $D(z^{-1})$ are 1). This model is usually represented by $OE(n_b, n_f, n_k)$, where n_k is the input delay and n_b and n_f are the order of the respective polynomials in the following equation:

$$y(t) = \frac{B(z^{-1})}{F(z^{-1})}u(t - n_k) + e(t) \tag{3.45}$$

Box-Jenkins Model

The Box-Jenkins model provides a complete characterization with disturbances dynamics separated from system dynamics ($A(z^{-1})$ is 1). It is usually represented by $BJ(n_b, n_c, n_d, n_f, n_k)$, where n_k is the input delay and n_b, n_c and n_f and n_f are the order of the respective polynomials in the following equation:

$$y(t) = \frac{B(z^{-1})}{F(z^{-1})}u(t - n_k) + \frac{C(z^{-1})}{D(z^{-1})}e(t) \tag{3.46}$$

Evaluation Criteria

We used three criteria for comparing the performance of the different structures and selecting the most adequate, before converting it to a transfer function: i) Akaike Information Criterion (AIC), ii) Bayesian Information Criterion (BIC) and iii) Minimum Description Length (MDL). These model selection metrics compare the relative quality of various models by dealing with a trade-off between the predictive accuracy (or goodness of fit) of the models and their number of parameters [89]. There is a general belief that the MDL tends to favor lower number of parameters over accuracy while AIC tends to favor higher accuracy over number of parameters . BIC is similar to AIC, but with a different penalty for the number of parameters, with the penalty being $2n_p$ for AIC and $log(N)n_p$, where N denotes the sample size and n_p denotes the number of parameters. These three metrics are defined by the following equations [89]:

$$AIC = Nlog(V) + 2n_p \tag{3.47}$$

$$BIC = Nlog(V) + log(N)n_p \tag{3.48}$$

$$MDL = V\left(1 + \frac{log(N)n_p}{N}\right) \tag{3.49}$$

$$V = \frac{1}{N}\sum_{1}^{N}\epsilon(t,\hat{\theta}_N)(\epsilon(t,\hat{\theta}_N))^T \tag{3.50}$$

where V is the loss function, N is the number of values in the estimation data set, $\epsilon(t)$ is a vector of prediction errors, $\hat{\theta}_N$ represents the estimated parameters and n_p is the number of estimated parameters. Additionally, the fit value between an estimated model and the measured cell response is calculated as follows:

$$Fit(\%) = \left(1 - \frac{\parallel y - \hat{y} \parallel}{\parallel y - \bar{y} \parallel}\right) \times 100 \tag{3.51}$$

where y is the measured output, $\hat{y}$ is the simulated or predicted model output and $\bar{y}$ is the mean of y.

Chapter 4

Results and Discussion

4.1 Wireless Power Transfer System Experimental Verification

In order to validate the theoretical analysis and the optimization process described in section 3.3.4, we pursue experimental studies on various aspects of the system.

Coil Optimized Geometry

Following the optimization process described in section 3.3.4 (Figure 3.25), the coil system PTE was maximized considering the constraints described in that section (Figure 3.3). First, the Rx coil was designed for maximizing the quality factor, involving the combination of N_{Rx} and p_{Rx} which results in the highest value of Q_{Rx} (Figure 4.1). Rx coil has 9 turns and a pitch of 1.8 mm.

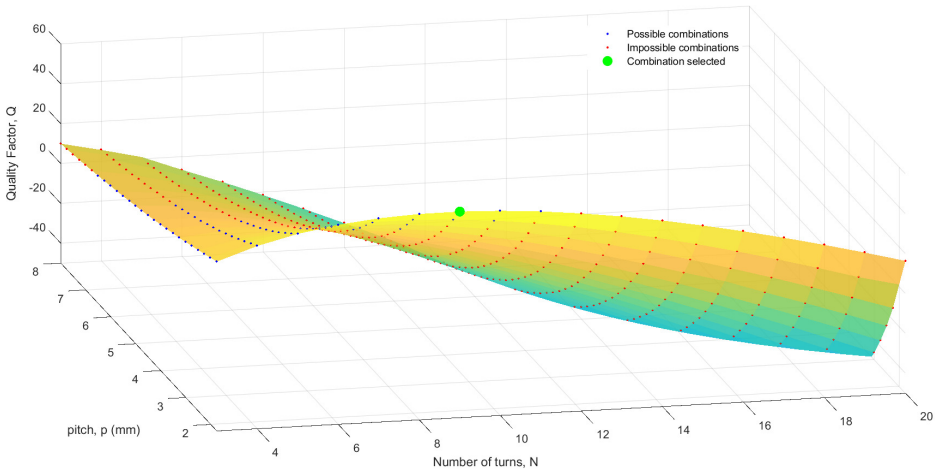

Figure 4.1: Resulting quality factor of Rx coil for different combinations of number of turns and pitch value.

The next step involved designing the TX coil for maximum quality factor, Q_{Tx} (best combination of N_{Tx} and p_{Tx}) for a given outer radius, $R_{Tx_{out}}$ (Figure 4.2). The results of this process were used to calculate the mutual inductance and coupling coefficient (Equations 3.29 to 3.33), after which the PTE was calculated following Equation 3.21 (Figure 4.3 *Left*). This process was repeated for other values

of outer radius until the maximum possible $R_{Tx_{out}}$ was reached. The combination of $R_{Tx_{out}}$, N_{Rx} and p_{Rx} which offered the highest PTE was selected, being 30 mm, 13 turns and 1.8 mm the corresponding optimal values (Figure 4.3 *Right*). Finally, the compensation capacitors were calculated from Equations 3.14 and 3.15, resulting in values of capacitance of 0.43 nF and 1.63 nF for the Tx and Rx circuit, respectively. The resulting geometric sizes and design parameters for each coil are listed in Table 4.1.

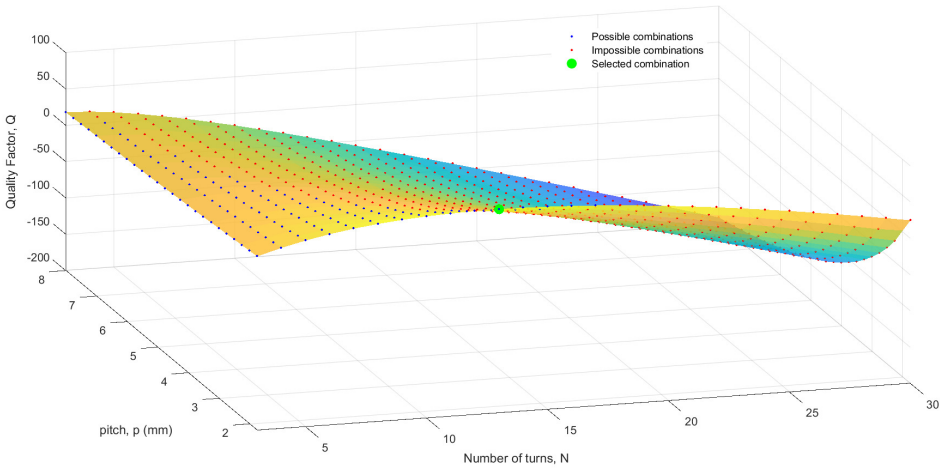

Figure 4.2: Resulting quality factor of Tx coil for different combinations of number of turns and pitch value.

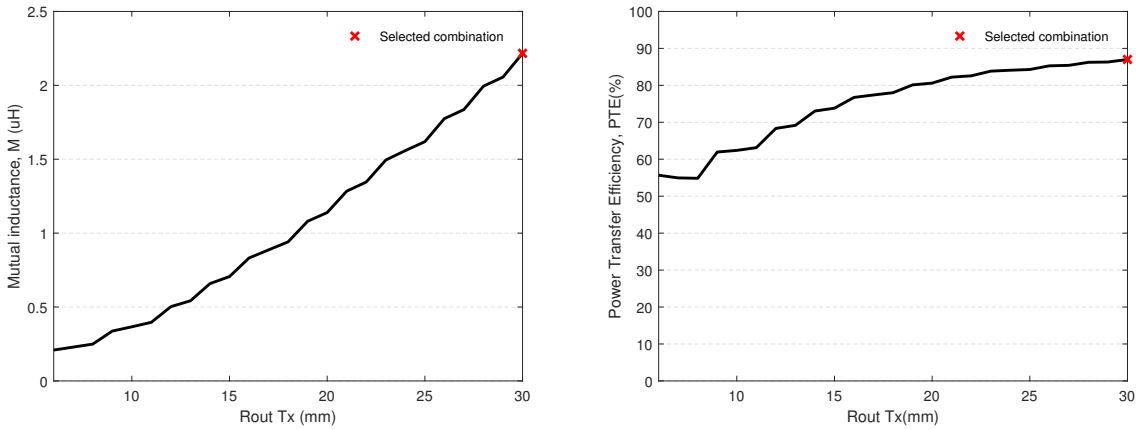

Figure 4.3: *Left:* Mutual Inductance dependence on $R_{out_{Tx}}$. *Right:* Power transfer efficiency dependence on $R_{out_{Tx}}$

Wireless Power Transfer System Performance

After both Rx and Tx coils geometries were optimized, experimental verification of the developed wireless power transfer system was conducted, as described in section 3.3.5. Figure 4.4 shows the simulated and experimentally measured power transfer efficiency of the design presented in Table 4.1 with a separation distance between transmitter and receiver coils of 10 mm. At an operation frequency of 3 MHz, the estimated efficiency is 87.3% and 88.4% for the optimization model and *Simulink*, respectively, while the experimental value measured is 76.6% through air medium and 74.3% through tissue medium. As estimated, the power transfer efficiency of the system decreases as the operation frequency

Parameter	Value
Tx outer radius, $R_{Tx_{out}}$	30 mm
Tx number of turns, , N_{Tx}	13
Rx number of turns, , N_{Rx}	9
Tx pitch, p_{Tx}	1.8 mm
Rx pitch, p_{Rx}	1.8 mm
Tx compensation capacitor, C_{Tx}	0.43 nF
Rx compensation capacitor, C_{Rx}	1.63 nF

Table 4.1: WPT system geometry

is reduced.

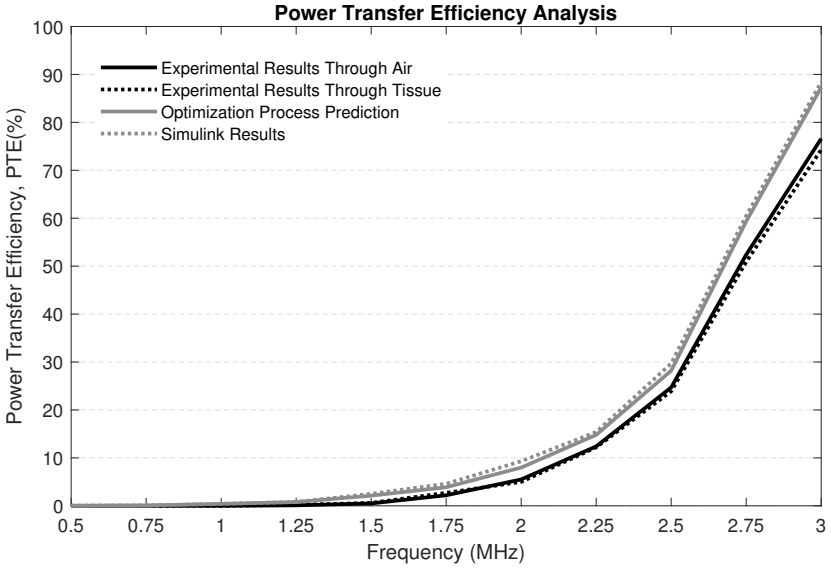

Figure 4.4: Power transfer efficiency values at different operation frequencies.

These results validate the optimization process, as the comparison of simulation and experimental measurements show relatively high levels of similarity along the spectrum of frequency between 0.5 and 3 MHz. The gap between simulated and experimental efficiency values may be explained either by a slight increase in losses in coils due to fabrication defects or due to hidden proximity losses, as the available models used to characterize the latter are only approximations with slight inherent flaws [84]. This last hypothesis is reinforced by the fact that the discrepancy between simulations and measured values increase with the raise of operating frequency (Figure 4.5), factor also associated with increase in proximity losses. From Figure 4.4, it is clear that the use of capacitors for compensation, which create resonant conditions, enhances the efficiency of the transfer system. Substituting these capacitors both in primary and secondary circuits by others adequate to different operating frequency enables the maximization of transfer efficiency.

Furthermore, experimental measurements with body tissue phantom validated the effectiveness of the purposed wireless power transfer system when implanted. The evolution of discrepancy between efficiency levels of experiments through air and through the body tissue phantom along the frequency spectrum (Figure 4.5) demonstrates that the body tissue specific absorption rate (SAR) is, as stated in section 3.3.1, proportional to the operating frequency. Thus, the increase in losses may result in

temperature raise of surrounding body tissues.

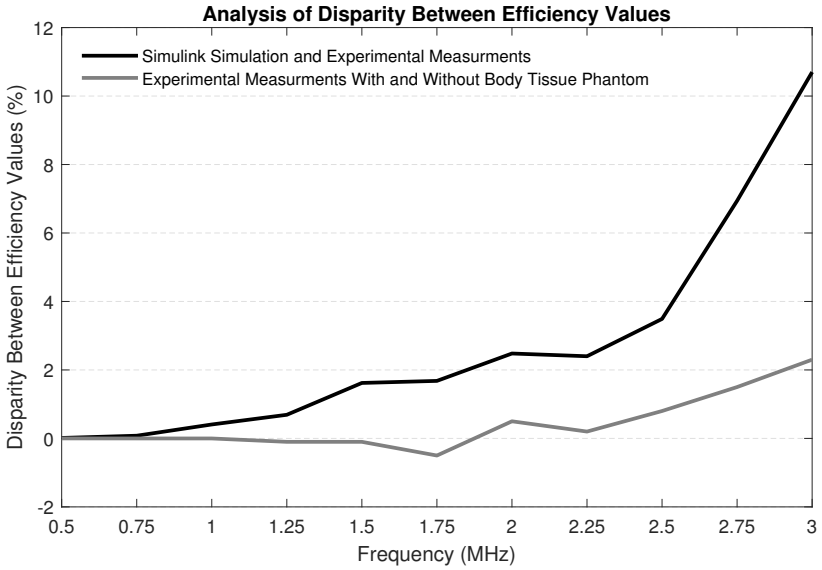

Figure 4.5: Discrepancy between power transfer efficiency results.

The design based on the proposed technique is compared with previously reported wireless power transfer systems applied to implanted devices. Table 4.2 summarizes the results. Efficiency, operation frequency and distance are presented as well as the radius of primary (R_{Rx}) and secondary (R_{Tx}) coils. Based on the results, the proposed wireless transfer system shows improvement with respect to other spiral-shaped and solenoid-shaped coil system, by maintaining relatively high efficiency with low operation frequency.

Ref.	Operation Freq. (MHz)	R_{Tx} (mm)	R_{Rx} (mm)	Distance (mm)	Shape	Efficiency
[90]	13.56	14.25	2.9	10	Spiral	86%
[91]	5	35	10	20	Spiral	20%
[92]	4.5	15	15	10	Solenoid	54%
[93]	18.5	50	25	10	Solenoid	53%

Table 4.2: Comparison with related works

4.2 Behavior Analysis of Living Optogenetically Targeted Cells

As mentioned in section 3.1, *in vitro* experiments aimed at both verifying the functionality of the optical neurostimulation endoprosthesis and analyzing the behaviour of optogenetically targeted cells when activated with the appropriate light. A microscope excitation light with similar light power density and wavelength properties as the LED was used in these experiments due to LED positioning issues (section 3.4.2).

The starting point of the *in vitro* experiments was verifying the existence of transfected cells expressing miniSOG protein. This verification was performed with a light power density of $6mW/mm^2$. Figure 4.6 demonstrates the existence of transfected cells. Even though some debris also showed fluorescence, this unspecific signal was easily identified since it was present for any excitation wavelength. For

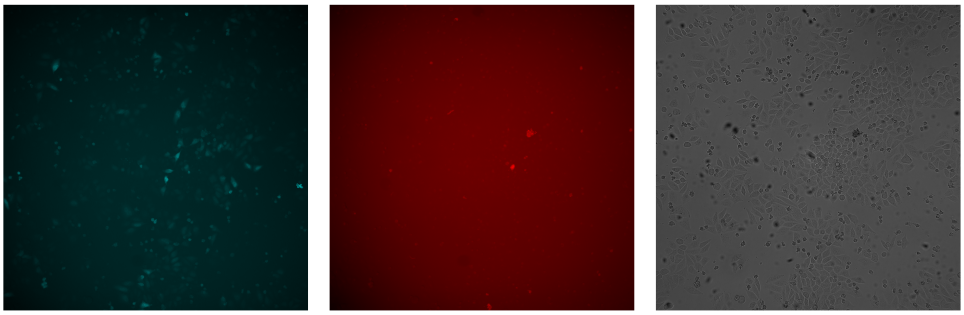

Figure 4.6: *Left:* Fluorescence imaging with 450 nm excitation light of transfected HeLa cells. *Middle:* Fluorescence imaging with 650 nm excitation light of transfected HeLa cells. *Right:* Transmitted light observation of of transfected HeLa cells.

example, this auto-fluorescence was observed in the red and green channels, while miniSOG fluorescence was specifically observed in the green channel (Figure 4.6).

Following this confirmation, a cell culture area expressing a relatively high amount of transfected cells was irradiated with each of the 6 available values of irradiance (section 3.4.2). Fluorescence images were captured and the change in fluorescence levels was analyzed using *Fiji* Software, as described in section 3.4.3. Figure 4.8 shows the normalized fluorescence with respect to the maximum value for each cell represented in Figure 4.7 in response to changes in the power density of blue light.

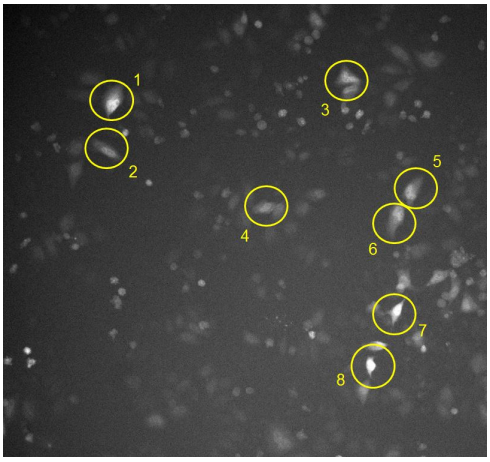

Figure 4.7: Cells analysed regarding fluorescence ratio

A careful interpretation of Figure 4.8 allows us to gather important information on light parameters necessary for inducing miniSOG generation of singlet oxygen, as this is closely related to fluorescence levels. First, the previously minimum reported light power density value used in experiments with miniSOG ($0.5mW/mm^2$) is shown to be enough to cause its activation, as all the observed cells react to the minimum irradiance available ($0.46mW/mm^2$) . The minimum light power density for causing 50% of maximum fluorescence is, therefore, under this value. Secondly, a light power density value between $1.75mW/mm^2$ and $3.3mW/mm^2$ seems enough to evoke the cell's full potential for generating singlet oxygen, as the fluorescence of all observed cells reaches its maximum level between these values (Leica DMI6000B do not allow intensity values between these two).

In addition to this, an experiment was designed in order to capture the fluorescent behaviour of miniSOG-transfected cells upon an input of blue light. Cells were illuminated constantly with blue light

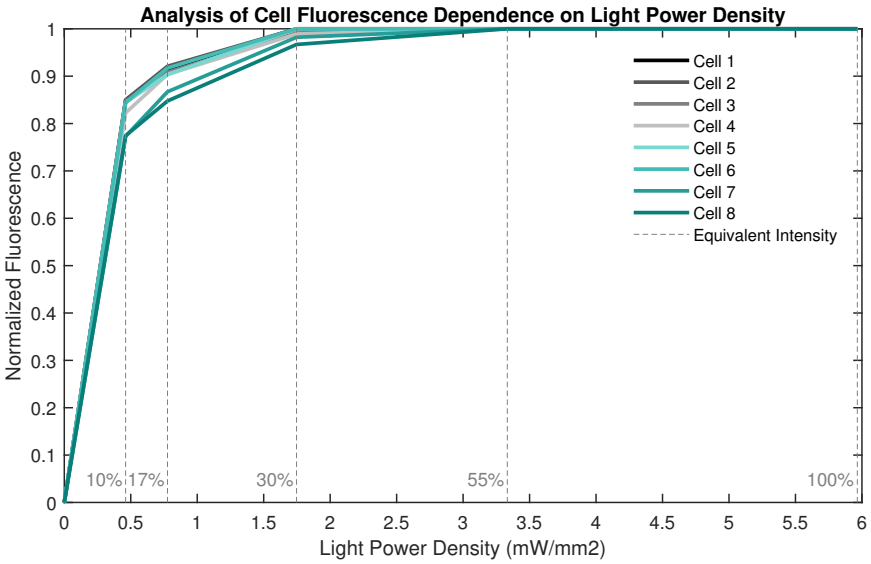

Figure 4.8: Normalized fluorescence of selected cells at different points of light power density.

($6mW/mm^2$ at 450 nm) during a period of 5 minutes. Figure 4.10 shows the normalized fluorescent level throughout time with respect to the maximum value for each cell represented in Figure 4.9, meaning that every cell starts with a fluorescence level of 1. In the systems identification context, this experiment would be equivalent to exposing a certain system (cell) to a step input (5 minutes illumination) of amplitude equal to $6mW/mm^2$. Image capture was processed in intervals of 10 seconds, resulting inn a sample time of the same value.

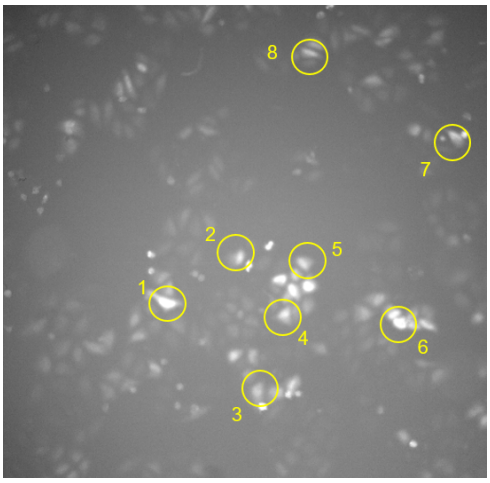

Figure 4.9: Cells analysed regarding fluorescence through time

A process involving the methods and evaluation criteria mentioned in section 3.4.4 was followed aiming at identifying a structure which would correctly model cell response blue light. First, cell 3 was selected randomly among the observed cell from Figure 4.9. Then, using *Matlab*'s System Identification Toolbox as well as the cell response to the 5 minute step input ($6mW/mm^2$ blue light), shown in Figure 4.10, the various model structures (ARX, ARMAX, OE and BJ) were tested with various parameters. Table 4.3 provides the best combination of parameters selected by each metric system (AIC, BIC and MDL) for each model structure for cell 3.

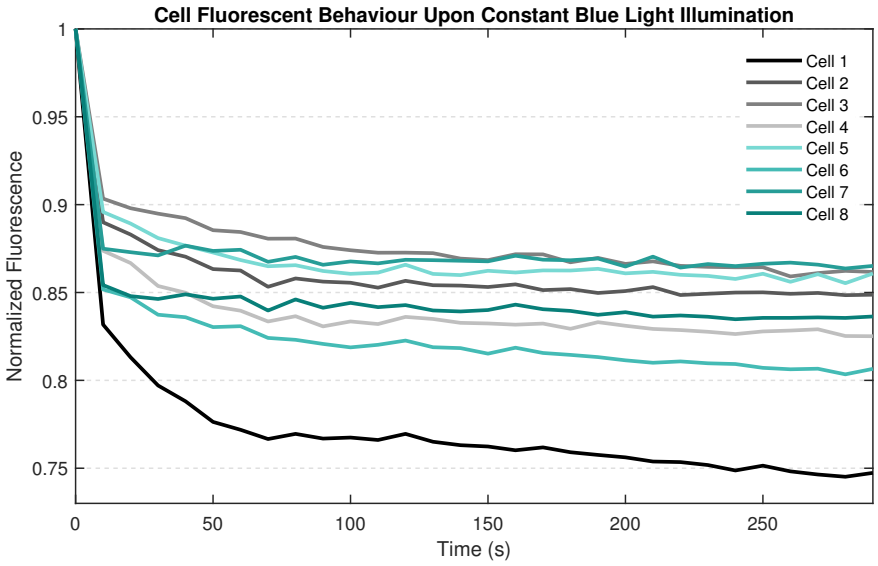

Figure 4.10: Normalized fluorescence of selected cells through time during experiment 2.

	AIC	BIC	MDL
ARX	[211]	[211]	[211]
ARMAX	[2111]	[2111]	[2111]
OE	[211]	[211]	[211]
BJ	[21111]	[21111]	[21111]

Table 4.3: Best combination of parameters selected by the different metric system.

Table 4.3 shows convergence of the three metric used regarding the combination of parameters for ARX, ARMAX, OE and BJ structures. Subsequently, an analysis of stability of each model structure is performed by analysing the position of zeros and poles in z-plane, as shown in Figure 4.11.

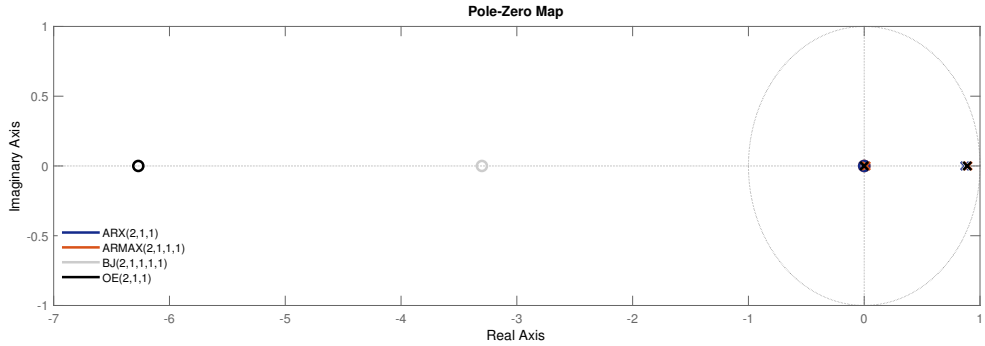

Figure 4.11: Pole-zero plot in z-plane of the different dynamic models

From Figure 4.11, we can observe that both OE and BJ structures have zeros outside the unit circle, creating non minimum phase system models. The response of a non minimum phase system to a step input has an ”undershoot”. This means that, if the output was initially zero and the steady state output is positive, the output becomes first negative before changing direction and converging to its positive steady state value. Looking from the perspective of the cell system, fluorescence value can never increase initially in response to a step input. Thus, both OE and BJ are excluded from the possible set of structures characterizing our system.

An analysis of transient response of the remaining ARX and ARMAX structures, presented in Figure 4.12, indicates very similar behaviour and steady-state value. Therefore, AIC, BIC, MDL and fit values for these two alternatives are compared and shown in Table 4.4.

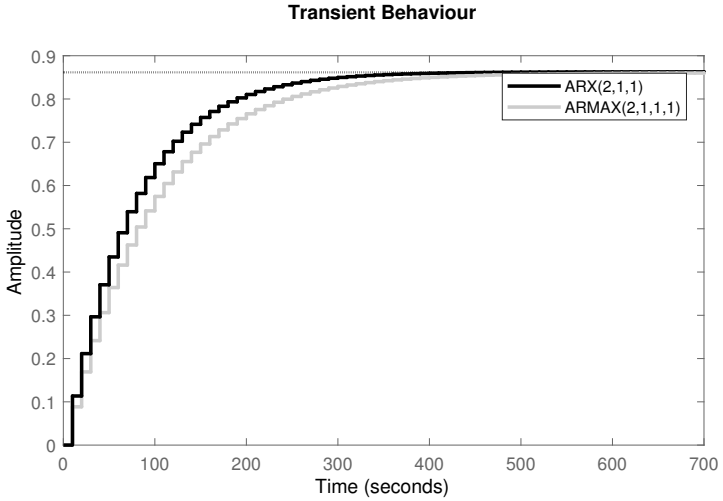

Figure 4.12: Step response of the remaining ARX and ARMAX model structures.

	AIC	BIC	MDL	Fit
ARX	-375.04	-369.43	1.24×10^{-4}	92.44%
ARMAX	-367.59	-363.38	1.57×10^{-4}	93.03%

Table 4.4: Comparison of AIC, BIC, MDL and fit values for ARX and ARMAX models

Even though the ARMAX model presents a better fit value, the three metrics converge into the selection of the ARX alternative, as they all present values slightly lower for this model structure due to its lower number of parameters. Further analysis with respect to the error between the output of these models and cell response were performed ($error = y - \hat{y}$), aiming at finding similarities between this error and white noise. The closest these are, the best the model describes the true dynamic of the cell system. For this purpose, the autocorrelation of the error sample of both model structures was plotted, as shown in Figure 4.13.

Figure 4.13 indicates that autocorrelation of error is very similar in both models, with ARX model showing a little more similarity to white noise (1 at 0 lag and 0 at the remaining lags). The mean value of the error ($E\left[error\right]$) for the ARX model is 1.53×10^{-4} and 1.72×10^{-4} for the ARMAX model, while this value is equal to 0 for white noise. The evaluation processes used until now have shown that both structures represent system response quite well. Because the ARX structure has less parameters and revealed a good performance on the evaluation processes, it is chosen to represent the cell system in further test. Figure 4.14 compares cell 3 and ARX(2,1,1) model response to the step input of 5 minutes and show the percentage of error along time.

Analyzing cell 3 response and identifying the system using black-box models resulted in a possible ARX(2,1,1) structure. Nonetheless, the main aim of this experiment is to identify the best model structure for the general cell system, rather than for single cell. Therefore, ARX(2,1,1) models were tested in the remaining seven cells. Each cell response was compared to the respective ARX(2,1,1) model, and both

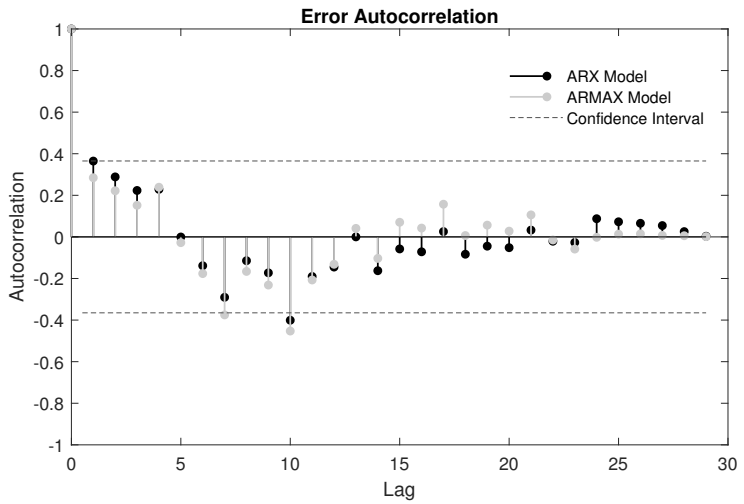

Figure 4.13: Error autocorrelation of error between the output of ARX and ARMAX models and cell response

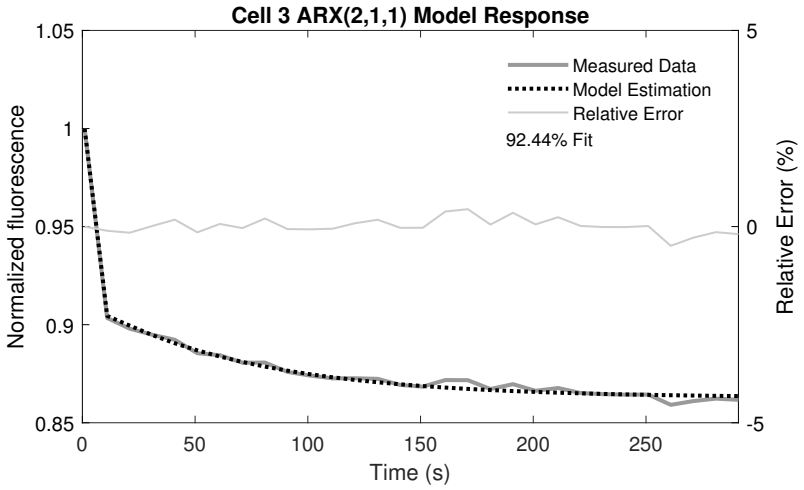

Figure 4.14: ARX(2,1,1) model comparison with cell 3 response.

model fit value and error autocorrelation were analyzed, following a similar process to the one followed with cell 3. Results are shown in Figures A.1 to A.7. Even though error autocorrelation exceeds the confidence interval in a few points in a few cells (particularly in cell 1), in general the results indicate that the tested model structure with one zero and two poles reproduces cell dynamics satisfactorily. Thus, considering the deterministic portion of the polynomial model, coupled to $u(t)$ in Equation 3.43, cell dynamics can be modelled with the following discrete transfer function:

$$sys(z^{-1}) = \frac{a_1 z^{-1}}{1 + b_1 z^{-1} + b_2 z^{-2}} \tag{4.1}$$

where a_1, b_1 and b_2 parameters, which depend on each individual cell, are presented in Table 4.5.

In order to validate this model, data from a third experiment was employed. After the last experiment, the same group of cells was subjected to a cycle of illumination involving 2 seconds of irradiance followed by 30 seconds of darkness during a period of 33 minutes. Image capture was processed during the 2 seconds of illumination (exposure time), resulting in a data set with a sample time of 30 seconds. Figure

	a_1	b_1	b_2
Cell 1	0.1626	-0.7951	-0.0109
Cell 2	0.2661	-0.6317	-0.0558
Cell 3	0.1135	-0.8630	-0.00555
Cell 4	0.2806	-0.5931	-0.0687
Cell 5	0.2969	-0.5934	-0.0623
Cell 6	0.1394	-0.8056	-0.0222
Cell 7	0.4303	-0.4854	-0.0188
Cell 8	0.2205	-0.7466	-0.0112

Table 4.5: ARX(2,1,1) model parameters for each cell.

4.15 shows the normalized fluorescent level throughout time versus to the maximum value for each cell represented in Figure 4.9, which means that every cell starts with a fluorescence level of 1. In the systems identification context, this experiment would be equivalent to exposing a certain system (cell) to a square wave of 32 seconds period and a pulse width of 6.6%. The amplitude of this square wave was, as in experiment 2, equal to $6mW/mm^2$ at 450 nm.

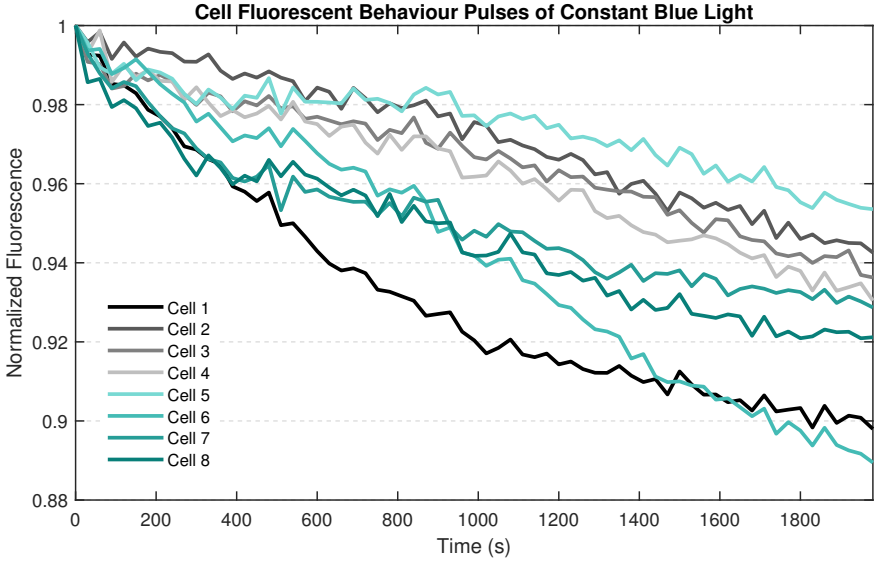

Figure 4.15: Normalized fluorescence of selected cells through time during experiment 3.

We used a process involving the application of the ARX(2,1,1) to estimate cell fluorescence behaviour in experiment 3, for the purpose of validating this model structure as a good representation of the cell system. First, cell 1 was selected randomly among the observed cells from Figure 4.9. Then, using *Simulink* Software, a square wave with similar properties to the one applied on the present experiment was used as input to a transfer function similar to the one on Equation 4.1 ($B(z^{-1})/A(z^{-1})$), with a sample time of 30 seconds. Likewise, a transfer function equal to $1/A(z^{-1})$ was used to characterize noise disturbances, as stated in the ARX structure. The parameters a_1, b_1 and b_2 of Equation 4.1 were modified until the output was sufficiently approximated to cell response in Figure 4.15. This process is illustrated in Figure 4.16.

Figure 4.17 shows the results of the validation process. The ARX(2,1,1) model structure approximated satisfactorily the behavior of cell 1 in the second experiment, with a fit value of 90.1%. The same process was repeated for two other cells, chosen arbitrarily, and the results were similar to those ob-

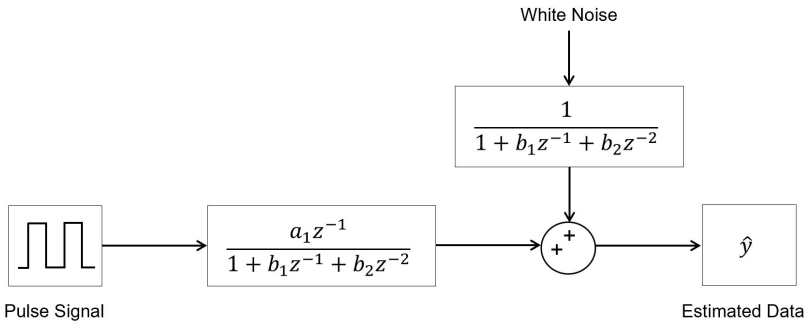

Figure 4.16: Simulink simulation of the ARX(2,1,1) model structure.

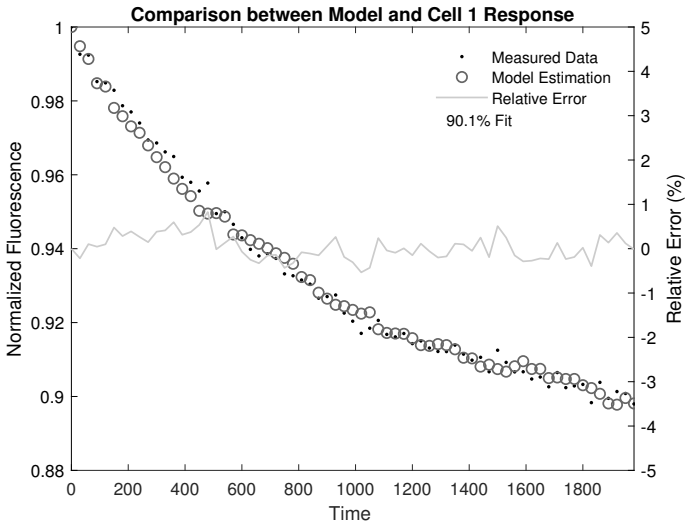

Figure 4.17: ARX(2,1,1) model response comparison with cell 1 response in experiment 3.

tained with cell 1, with fit values of 80.6% and 76.6% for cells 7 and 8, respectively (Figure 4.18). Table 4.6 presents the parameters a_1, b_1 and b_2 for the three analyzed cells.

After using a step signal as the input to the system and selecting ARX(2,1,1) as the best model structure to approximate the resulting data, the system response to a pulse signal was used to validate this model selection. Even though the fit values were slightly lower in the validation process (around 10% lower), this might be consequence of the system identification method, which involved an iterative process of adjusting the combination of three parameters (a_1, b_1 and b_2), using only fit value as a figure of merit. Therefore, after applying the system identification methods presented in this chapter, a deterministic model structure of two poles and one zero fairly describes the behaviour of miniSOG in a living cell system.

	a_1	b_1	b_2
Cell 1	0.0052	-0.5739	-0.3804
Cell 7	0.0041	-0.5639	-0.3804
Cell 8	0.0040	-0.5700	-0.3850

Table 4.6: ARX(2,1,1) model parameters for each cell.

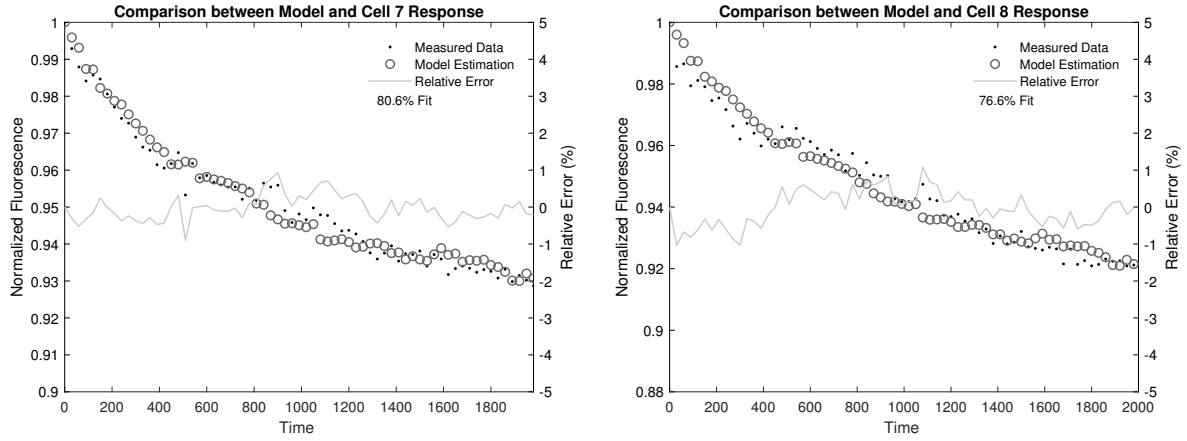

Figure 4.18: ARX(2,1,1) model response comparison with cell 7 and 8 response in experiment 3.

Chapter 5

Conclusion and Recommendations

5.1 Conclusion

Optogenetic technologies and the opportunities they offer for cell modulation suggest that a device capable to delivering optimized optical stimulation to targeted cells could pose a significant advance in therapeutic and regenerative medicine. Therefore, the present work focused on the development of neurostimulation endoprosthesis involving these technologies. Starting from a review of optogenetic tools, methods and results to this moment, specific features considered necessary for the device to meet its requirements at this stage of research were selected. These involved the light delivery system through LED channels and the wireless power supply approach (section 3.1).

Light requirements for such a device were analysed, namely wavelength and power density necessary for activation of two specific optogenetic tools - NpHR and MiniSOG, proteins which may reveal important agents in regenerative medicine. Two LED models available in the market were selected and analyzed, resulting in the acceptance of the blue LED model and the disapproval of the yellow LED model for not meeting the necessary requirements (section 3.2.1). A light delivery control system was implemented to control light properties. This system involved an *Arduino Uno* to control the current supplied to the LED and a current sensor (INA219) to provide feedback and close the loop. Control of light properties was accomplished through a proportional-integral (PI) approach for the blue LED, achieving a stable current value within a ± 0.2 mA margin around the desired value (section 3.2.2).

A wireless power supply system was proposed based on an inductive link between a pair of transceiver and receiver coils. A two-stage voltage multiplier was designed in order to rectify the AC current provided by the WPT system and decrease the amount of energy necessary on the primary circuit (section 3.21). System requirements were set and taken as the starting point of an optimization process designed to achieve maximum power transfer efficiency (section 3.3.4). The resulting inductance coils were compensated by capacitors, creating resonant conditions which were demonstrated to enhance efficiency levels. The efficiency of the designed wireless power transfer system was experimentally measured through air and through a material with similar characteristics of body tissues, showing a power transfer efficiency of 76.6% through air and 74.3% through body tissue phantom (section 4.1). These values were compared

with previously reported works and showed improvement.

In vitro experiments using light properties similar to those of the blue LED model analyzed in this thesis presented useful information on the behaviour of living miniSOG-targeted cells upon blue light activation (section 4.2). Experiments with different values of light intensity demonstrated that a power density value near $0.5mW/mm^2$ results in a fluorescence response of around 80% of the maximum fluorescence potential of the cell, which is achieved with values between $1.75mW/mm^2$ and $3.3mW/mm^2$. Additionally, a miniSOG-targeted cell culture illuminated during 5 minutes at $6mW/mm^2$ in order to observe fluorescence decay and model cell response to light. After testing a number of parametric model structures and evaluation metrics, the ARX(2,1,1) suited the general cell system satisfactorily. A third experiment and process of iteration between parameters values was used to validate this model structure. These experiments reveal a cell behaviour correspondent to a second order system with one zero and two poles.

The methods applied in this thesis as well as the various issues discussed constitute a "Proof-of-Concept" for biomedical devices involving optogenetic technologies and create a solid basis for improvement. The process followed in this work for analyzing the LED models can be followed for any other selected model and/or optogenetic tools, while taking into account their requirements.

5.2 Recommendations

For reasons mentioned in section 3.4.2, the developed LED system could not be used in the *in vitro* experiments to stimulate targeted cells, leaving the effects of the LED light on cells untested. We have considered several options to overcome this issue in future work. MiniSOG expressed in neurons in fusion with proteins from the synaptic terminal was able to interfere with neural transmission, just as NpHR does, but by other means [94], resulting in membrane voltage changes. Thus, substituting optical readouts of neural activity for an electrophysiology technique approach for both miniSOG and NpHR contexts could solve the LED positioning issue. In addition, cell current and membrane voltage readings could supply information about the activation transient with higher resolution than in the present circumstances, allowing better cell behaviour modelling.

Regarding energy supply to the biomedical device, further work must be carried out aiming to reduce the size of coils and improving their efficiency. From the Equations presented in section 3.3.4 it is clear that efficiency is proportional to the operating frequency. Increasing the operating frequency to a higher value but still safe would lead to a decrease in coil and overall system size.

The light delivery control system developed relied on the *Arduino* capabilities to control the power it supplied to the circuit. In order to eliminate tethers and maintain the control of light properties, a close-loop control system should be developed incorporating i) a current sensor reading the current fed to the LED, and ii) a data transmission antenna for enabling communication with the exterior power management section. The controller placed on the interior section of the system would carry a control action which could be communicated to the power management section, thereby controlling the energy provided to the implant and closing the loop.

Additional experiments involving different cell types and light properties, such as pulse frequency and duration and light power density, could contribute to increase available knowledge on miniSOG and NpHR capabilities. Studying transient behaviour of cell response as well as optimizing light actuation for specific objectives could enable the creation of better models and close-loop control systems. Studies of this sort could eventually evolve into *in vivo* experiments, initially in *C.Elegans* and zebra fish, and later in mammals like mice. These experiments are useful tools for studying both desired photosensitive protein applications and issues related to the implant itself, such as its installation in living bodies, energy transfer and light delivery.

References

[1] R. Nieuwenhuys, J. J. Voogd, and C. v. Huijzen. *The human central nervous system*. Springer, 2008. ISBN 9783540346845.

[2] O. Yizhar, L. E. Fenno, T. J. Davidson, M. Mogri, and K. Deisseroth. Optogenetics in Neural Systems, 7 2011. ISSN 08966273.

[3] F. Zhang, J. Vierock, O. Yizhar, L. E. Fenno, S. Tsunoda, A. Kianianmomeni, M. Prigge, A. Berndt, J. Cushman, J. Polle, J. Magnuson, P. Hegemann, and K. Deisseroth. The microbial opsin family of optogenetic tools. *Cell*, 2011. ISSN 00928674. doi: 10.1016/j.cell.2011.12.004.

[4] V. Gradinaru, K. R. Thompson, and K. Deisseroth. eNpHR: A Natronomonas halorhodopsin enhanced for optogenetic applications. *Brain Cell Biology*, 2008. ISSN 15597105. doi: 10.1007/s11068-008-9027-6.

[5] Y. B. Qi, E. J. Garren, X. Shu, R. Y. Tsien, and Y. Jin. Photo-inducible cell ablation in Caenorhabditis elegans using the genetically encoded singlet oxygen generating protein miniSOG. *Proceedings of the National Academy of Sciences of the United States of America*, 109(19):7499–7504, 5 2012. ISSN 00278424. doi: 10.1073/pnas.1204096109.

[6] K. L. Montgomery, S. M. Iyer, A. J. Christensen, K. Deisseroth, and S. L. Delp. Beyond the brain: Optogenetic control in the spinal cord and peripheral nervous system, 2016. ISSN 19466242.

[7] R. P. Kale, A. Z. Kouzani, K. Walder, M. Berk, J. Berk, and S. J. Tye. Wireless Optogenetics: An Exploration of Portable Microdevices for Small Animal Photostimulation. *Procedia Technology*, 2015. ISSN 22120173. doi: 10.1016/j.protcy.2015.07.036.

[8] K. Deisseroth, G. Feng, A. K. Majewska, G. Miesenbock, A. Ting, and M. J. Schnitzer. Next-Generation Optical Technologies for Illuminating Genetically Targeted Brain Circuits. *Journal of Neuroscience*, 26(41): 10380–10386, 10 2006. ISSN 0270-6474. doi: 10.1523/jneurosci.3863-06.2006.

[9] Francis Crick. The impact of molecular biology on neuroscience. *Royal Sociaty*, &NA;(1111):2, 12 1999. doi: 10.2165/00128413-199711110-00002.

[10] B. V. Zemelman, G. A. Lee, M. Ng, and G. M. Ck. Neurotechnique Selective Photostimulation of Genetically ChARGed Neurons. Technical report, 2002.

[11] B. V. Zemelman, N. Nesnas, G. A. Lee, and G. Miesenbock. Photochemical gating of heterologous ion channels: Remote control over genetically designated populations of neurons. *Proceedings of the National Academy of Sciences*, 100(3):1352–1357, 2 2003. ISSN 0027-8424. doi: 10.1073/pnas.242738899.

[12] M. Banghart, K. Borges, E. Isacoff, D. Trauner, and R. H. Kramer. Light-activated ion channels for remote control of neuronal firing. *Nature Neuroscience*, 7(12):1381–1386, 12 2004. ISSN 10976256. doi: 10.1038/nn1356.

[13] M. Volgraf, P. Gorostiza, R. Numano, R. H. Kramer, E. Y. Isacoff, and D. Trauner. Allosteric control of an ionotropic glutamate receptor with an optical switch. *Nature Chemical Biology*, 2(1):47–52, 2006. ISSN 15524469. doi: 10.1038/nchembio756.

[14] S. Q. Lima and G. Miesenböck. Remote control of behavior through genetically targeted photostimulation of neurons. *Cell*, 121(1):141–152, 4 2005. ISSN 00928674. doi: 10.1016/j.cell.2005.02.004.

[15] E. S. Boyden, F. Zhang, E. Bamberg, G. Nagel, and K. Deisseroth. Millisecond-timescale, genetically targeted optical control of neural activity. *Nature Neuroscience*, 8(9):1263–1268, 2005. ISSN 10976256. doi: 10.1038/nn1525.

[16] G. Nagel, T. Szellas, W. Huhn, S. Kateriya, N. Adeishvili, P. Berthold, D. Ollig, P. Hegemann, and E. Bamberg. Channelrhodopsin-2, a directly light-gated cation-selective membrane channel. *Proceedings of the National Academy of Sciences*, 100(24):13940–13945, 11 2003. ISSN 0027-8424. doi: 10.1073/pnas.1936192100.

[17] D. OESTERHELT and W. STOECKENIUS. Rhodopsin-like Protein from the Purple Membrane of Halobacterium halobium. *Nature New Biology*, 233:149, 9 1971. URL `https://doi.org/10.1038/newbio233149a010.1038/newbio233149a0`.

[18] A. Matsuno-Yagi and Y. Mukohata. *Two possible roles of bacteriorhodopsin; a comparative study of strains of Halobacterium halobium differing in pigmentation*, volume 78. 10 1977. doi: 10.1016/0006-291X(77)91245-1.

[19] J. K Lanyi and D. Oesterhelt. *Identification of the retinal-binding protein in halorhodopsin*, volume 257. 4 1982.

[20] G. Nagel, D. Ollig, M. Fuhrmann, S. Kateriya, A. M. Musti, E. Bamberg, and P. Hegemann. Channelrhodopsin-1: A Light-Gated Proton Channel in Green Algae. *Science*, 296(5577):2395–2398, 2002. ISSN 0036-8075. doi: 10.1126/science.1072068. URL `https://science.sciencemag.org/content/296/5577/2395`.

[21] F. Zhang, A. Gottschalk, K. Kay, K. Deisseroth, N. Watzke, L.-P. Wang, G. Nagel, M. Brauner, E. Bamberg, J. F. Liewald, and P. G. Wood. Multimodal fast optical interrogation of neural circuitry. *Nature*, 2007. ISSN 0028-0836. doi: 10.1038/nature05744.

[22] S. S. Srinivasan, B. E. Maimon, M. Diaz, H. Song, and H. M. Herr. Closed-loop functional optogenetic stimulation. *Nature Communications*, 2018. ISSN 20411723. doi: 10.1038/s41467-018-07721-w.

[23] Ádám, A. Hajdu, F. Nagy, and A. Viczián. Optogenetics: past, present and future. Technical report, 2015. URL `http://www.sci.u-szeged.hu/ABS`.

[24] Bruno Camporeze, Bruno Alcântara Manica, Gabriel Alves Bonafé, Jivago Jordão Camargos Ferreira, Aurélio Lourenço Diniz, Carlos Tadeu Parisi de Oliveira, Luis Roberto Mathias Junior, Paulo Henrique Pires de Aguiar, and Manoela Marques Ortega. Optogenetics: the new molecular approach to control functions of neural cells in epilepsy, depression and tumors of the central nervous system.

[25] B. Sijobert, C. Verna, C. Geny, D. Andreu, and C. Azevedo-Coste. Effects of sensitive electrical stimulation based cueing in Parkinson's disease: a preliminary study. *European Journal of Translational Myology*, 26(2), 6 2016. ISSN 2037-7452. doi: 10.4081/ejtm.2016.6018.

[26] J. D. Rolston, S. A. Desai, N. G. Laxpati, and R. E. Gross. Electrical Stimulation for Epilepsy: Experimental Approaches, 10 2011. ISSN 10423680.

[27] P. H. Peckham and G. H. Creasey. Neural prostheses: Clinical applications of functional electrical stimulation in spinal cord injury. *Paraplegia*, 30(2):96–101, 1992. ISSN 00311758. doi: 10.1038/sc.1992.33.

[28] P. H. Peckham and J. S. Knutson. Functional Electrical Stimulation for Neuromuscular Applications. *Annual Review of Biomedical Engineering*, 7(1):327–360, 8 2005. ISSN 1523-9829. doi: 10.1146/annurev.bioeng.6.040803.140103.

[29] M. H. Histed, V. Bonin, and R. C. Reid. Direct Activation of Sparse, Distributed Populations of Cortical Neurons by Electrical Microstimulation. *Neuron*, 63(4):508–522, 8 2009. ISSN 08966273. doi: 10.1016/j.neuron.2009.07.016.

[30] M. E. Llewellyn, K. R. Thompson, K. Deisseroth, and S. L. Delp. Orderly recruitment of motor units under optical control in vivo. *Nature Medicine*, 2010. ISSN 1546170X. doi: 10.1038/nm.2228.

[31] J. M. Sorokin, T. J. Davidson, E. Frechette, A. M. Abramian, K. Deisseroth, J. R. Huguenard, and J. T. Paz. Bidirectional Control of Generalized Epilepsy Networks via Rapid Real-Time Switching of Firing Mode. *Neuron*, 93(1):194–210, 1 2017. ISSN 10974199. doi: 10.1016/j.neuron.2016.11.026.

[32] K. J. Mastro, K. T. Zitelli, A. M. Willard, K. H. Leblanc, A. V. Kravitz, and A. H. Gittis. Cell-specific pallidal intervention induces long-lasting motor recovery in dopamine-depleted mice. *Nature Neuroscience*, 20(6):815–823, 6 2017. ISSN 15461726. doi: 10.1038/nn.4559.

[33] A. M. Aravanis, L. P. Wang, F. Zhang, L. A. Meltzer, M. Z. Mogri, M. B. Schneider, and K. Deisseroth. An optical neural interface: in vivo control of rodent motor cortex with integrated fiberoptic and optogenetic technology. *Journal of neural engineering*, 4(3), 2007. ISSN 17412560. doi: 10.1088/1741-2560/4/3/S02.

[34] M. A. Anderson, Y. Ao, and M. V. Sofroniew. Heterogeneity of reactive astrocytes, 2014. ISSN 18727972.

[35] J. Silver and J. H. Miller. Regeneration beyond the glial scar, 2004. ISSN 1471003X.

[36] S. Xu and A. D. Chisholm. Highly efficient optogenetic cell ablation in C. Elegans using membrane-targeted miniSOG. *Scientific Reports*, 6, 2 2016. ISSN 20452322. doi: 10.1038/srep21271.

[37] C. Gumera, B. Rauck, and Y. Wang. Materials for central nervous system regeneration: Bioactive cues. *Journal of Materials Chemistry*, 21(20):7033–7051, 5 2011. ISSN 09599428. doi: 10.1039/c0jm04335d.

[38] V. Gradinaru, K. Deisseroth, R. Prakash, L. A. Gunaydin, O. Yizhar, M. Hyun, K. M. Tye, C. Ramakrishnan, E. A. Ferenczi, J. Mattis, L. E. Fenno, and D. J. O'Shea. Principles for applying optogenetic tools derived from direct comparative analysis of microbial opsins. *Nature Methods*, 2011. ISSN 1548-7091. doi: 10.1038/nmeth.1808.

[39] X. Han and E. S. Boyden. Multilpe-color optical activation, silencing, and desynchronization of neural activity, with single-spike temporal resolution. *PLoS ONE*, 2(3), 3 2007. ISSN 19326203. doi: 10.1371/journal.pone.0000299.

[40] A. Gharbi-Ayachi, J. C. Labbé, A. Burgess, S. Vigneron, J. M. Strub, E. Brioudes, A. Van-Dorsselaer, A. Castro, and T. Lorca. The substrate of Greatwall kinase, Arpp19, controls mitosis by inhibiting protein phosphatase 2A. *Science*, 330(6011):1673–1677, 12 2010. ISSN 00368075. doi: 10.1126/science.1197048.

[41] K. M. Tye, R. Prakash, S. Y. Kim, L. E. Fenno, L. Grosenick, H. Zarabi, K. R. Thompson, V. Gradinaru, C. Ramakrishnan, and K. Deisseroth. Amygdala circuitry mediating reversible and bidirectional control of anxiety. *Nature*, 471(7338):358–362, 3 2011. ISSN 00280836. doi: 10.1038/nature09820.

[42] I. Goshen, M. Brodsky, R. Prakash, J. Wallace, V. Gradinaru, C. Ramakrishnan, and K. Deisseroth. Dynamics of retrieval strategies for remote memories. *Cell*, 147(3):678–689, 10 2011. ISSN 00928674. doi: 10.1016/j.cell.2011.09.033.

[43] V. Gradinaru, F. Zhang, C. Ramakrishnan, J. Mattis, R. Prakash, I. Diester, I. Goshen, K. R. Thompson, and K. Deisseroth. Molecular and Cellular Approaches for Diversifying and Extending Optogenetics. *Cell*, 141(1): 154–165, 4 2010. ISSN 00928674. doi: 10.1016/j.cell.2010.02.037.

[44] A. Berndt, O. Yizhar, L. A. Gunaydin, P. Hegemann, and K. Deisseroth. Bi-stable neural state switches. *Nature Neuroscience*, 12(2):229–234, 2 2009. ISSN 10976256. doi: 10.1038/nn.2247.

[45] J. Torra, C. Lafaye, L. Signor, S. Aumonier, C. Flors, X. Shu, S. Nonell, G. Gotthard, and A. Royant. Tailing miniSOG: structural bases of the complex photophysics of a flavin-binding singlet oxygen photosensitizing protein. *Scientific Reports*, 9(1), 12 2019. ISSN 20452322. doi: 10.1038/s41598-019-38955-3.

[46] X. Shu, V. Lev-Ram, T. J. Deerinck, Y. Qi, E. B. Ramko, M. W. Davidson, Y. Jin, M. H. Ellisman, and R. Y. Tsien. A genetically encoded tag for correlated light and electron microscopy of intact cells, tissues, and organisms. *PLoS Biology*, 9(4), 4 2011. ISSN 15449173. doi: 10.1371/journal.pbio.1001041.

[47] J. Wang, F. Wagner, D. A. Borton, J. Zhang, I. Ozden, R. D. Burwell, A. V. Nurmikko, R. Van Wagenen, I. Diester, and K. Deisseroth. Integrated device for combined optical neuromodulation and electrical recording for chronic in vivo applications. *Journal of Neural Engineering*, 9(1), 2 2012. ISSN 17412560. doi: 10.1088/1741-2560/9/1/016001.

[48] P. Anikeeva, A. S. Andalman, I. Witten, M. Warden, I. Goshen, L. Grosenick, L. A. Gunaydin, L. M. Frank, and K. Deisseroth. Optetrode: A multichannel readout for optogenetic control in freely moving mice. *Nature Neuroscience*, 15(1):163–170, 1 2012. ISSN 10976256. doi: 10.1038/nn.2992.

[49] I. Clements, A. G. Gnade, A. Rush, C. Patten, M. C. Twomey, and A. Kravitz. *Miniaturized LED sources for in vivo optogenetic experimentation*, volume 8586. 2 2013. doi: 10.1117/12.2008080.

[50] D. C. Klorig and D. W. Godwin. A magnetic rotary optical fiber connector for optogenetic experiments in freely moving animals. *Journal of Neuroscience Methods*, 227:132–139, 4 2014. ISSN 1872678X. doi: 10.1016/j.jneumeth.2014.02.013.

[51] R. Ameli, A. Mirbozorgi, J. L. Neron, Y. Lechasseur, and B. Gosselin. A wireless and batteryless neural headstage with optical stimulation and electrophysiological recording. In *Proceedings of the Annual International Conference of the IEEE Engineering in Medicine and Biology Society, EMBS*, 2013. ISBN 9781457702167. doi: 10.1109/EMBC.2013.6610835.

[52] C. T. Wentz, J. G. Bernstein, P. Monahan, A. Guerra, A. Rodriguez, and E. S. Boyden. A wirelessly powered and controlled device for optical neural control of freely-behaving animals. In *Journal of Neural Engineering*, volume 8, 8 2011. doi: 10.1088/1741-2560/8/4/046021.

[53] K. Y. Kwon, H.-M. Lee, M. Ghovanloo, A. Weber, and W. Li. Design, fabrication, and packaging of an integrated, wirelessly-powered optrode array for optogenetics application. *Frontiers in Systems Neuroscience*, 9, 5 2015. doi: 10.3389/fnsys.2015.00069.

[54] A. J. Yeh, J. S. Ho, Y. Tanabe, E. Neofytou, R. E. Beygui, and A. S. Y. Poon. Wirelessly powering miniature implants for optogenetic stimulation. *Applied Physics Letters*, 103(16):163701, 10 2013. ISSN 0003-6951. doi: 10.1063/1.4825272. URL `http://aip.scitation.org/doi/10.1063/1.4825272`.

[55] K. L. Montgomery, A. J. Yeh, J. S. Ho, V. Tsao, S. M. Iyer, L. Grosenick, and E. A. Ferenczi. Wirelessly powered, fully internal optogenetics for brain, spinal and peripheral circuits in mice. *Nature Methods*, 2015. doi: 10.1038/nmeth.3536.

[56] Y. Iwai, S. Honda, H. Ozeki, M. Hashimoto, and H. Hirase. A simple head-mountable LED device for chronic stimulation of optogenetic molecules in freely moving mice. *Neuroscience Research*, 70(1):124–127, 5 2011. ISSN 01680102. doi: 10.1016/j.neures.2011.01.007.

[57] M. Hashimoto, A. Hata, T. Miyata, and H. Hirase. Programmable wireless light-emitting diode stimulator for chronic stimulation of optogenetic molecules in freely moving mice. *Neurophotonics*, 1(1):011002, 5 2014. ISSN 2329-423X. doi: 10.1117/1.nph.1.1.011002.

[58] S. T. Lee, P. A. Williams, C. E. Braine, D. T. Lin, S. W. John, and P. P. Irazoqui. A Miniature, Fiber-Coupled, Wireless, Deep-Brain Optogenetic Stimulator. *IEEE Transactions on Neural Systems and Rehabilitation Engineering*, 23(4):655–664, 7 2015. ISSN 15344320. doi: 10.1109/TNSRE.2015.2391282.

[59] T. I. Kim, J. G. McCall, Y. H. Jung, X. Huang, E. R. Siuda, Y. Li, J. Song, Y. M. Song, H. A. Pao, R. H. Kim, C. Lu, S. D. Lee, I. S. Song, G. Shin, R. Al-Hasani, S. Kim, M. P. Tan, Y. Huang, F. G. Omenetto, J. A. Rogers, and M. R. Bruchas. Injectable, cellular-scale optoelectronics with applications for wireless optogenetics. *Science*, 340(6129):211–216, 4 2013. ISSN 10959203. doi: 10.1126/science.1232437.

[60] J. G. McCall, T. I. Kim, G. Shin, X. Huang, Y. H. Jung, R. Al-Hasani, F. G. Omenetto, M. R. Bruchas, and J. A. Rogers. Fabrication and application of flexible, multimodal light-emitting devices for wireless optogenetics. *Nature Protocols*, 8(12):2413–2428, 2013. ISSN 17502799. doi: 10.1038/nprot.2013.158.

[61] R. P. Kale, A. Z. Kouzani, K. Walder, M. Berk, and S. J. Tye. Evolution of optogenetic microdevices. 2015. doi: 10.1117/1.

[62] A. B. Arrenberg, F. Del Bene, and H. Baier. Optical control of zebrafish behavior with halorhodopsin. *Proceedings of the National Academy of Sciences*, 2009. ISSN 0027-8424. doi: 10.1073/pnas.0906252106.

[63] V. Gradinaru, K. R. Thompson, F. Zhang, M. Mogri, K. Kay, M. B. Schneider, and K. Deisseroth. Targeting and Readout Strategies for Fast Optical Neural Control In Vitro and In Vivo. *Journal of Neuroscience*, 27 (52):14231–14238, 12 2007. ISSN 0270-6474. doi: 10.1523/JNEUROSCI.3578-07.2007. URL `http://www.jneurosci.org/cgi/doi/10.1523/JNEUROSCI.3578-07.2007`.

[64] V. Gradinaru, M. Mogri, K. R. Thompson, J. M. Henderson, and K. Deisseroth. Optical deconstruction of parkinsonian neural circuitry. *Science*, 2009. ISSN 00368075. doi: 10.1126/science.1167093.

[65] J. Zhang, F. Laiwalla, J. A. Kim, H. Urabe, R. Van Wagenen, Y. K. Song, B. W. Connors, F. Zhang, K. Deisseroth, and A. V. Nurmikko. Integrated device for optical stimulation and spatiotemporal electrical recording of neural

activity in light-sensitized brain tissue. *Journal of Neural Engineering*, 6(5), 2009. ISSN 17412560. doi: 10.1088/1741-2560/6/5/055007.

[66] S. Royer, B. V. Zemelman, M. Barbic, A. Losonczy, G. Buzsáki, and J. C. Magee. Multi-array silicon probes with integrated optical fibers: Light-assisted perturbation and recording of local neural circuits in the behaving animal. *European Journal of Neuroscience*, 31(12):2279–2291, 6 2010. ISSN 0953816X. doi: 10.1111/j.1460-9568.2010.07250.x.

[67] A. R. Adamantidis, F. Zhang, A. M. Aravanis, K. Deisseroth, and L. De Lecea. Neural substrates of awakening probed with optogenetic control of hypocretin neurons. *Nature*, 450(7168):420–424, 11 2007. ISSN 14764687. doi: 10.1038/nature06310.

[68] Y. P. Zhang and T. G. Oertner. Optical induction of synaptic plasticity using a light-sensitive channel. *Nature Methods*, 4(2):139–141, 2 2007. ISSN 15487091. doi: 10.1038/nmeth988.

[69] F. Zhang, V. Gradinaru, A. R. Adamantidis, R. Durand, R. D. Airan, L. de Lecea, and K. Deisseroth. Optogenetic interrogation of neural circuits: technology for probing mammalian brain structures. *Nature Protocols*, 5:439, 2 2010. URL `https://doi.org/10.1038/nprot.2009.22610.1038/nprot.2009.226`.

[70] J. H. Lee, R. Durand, V. Gradinaru, F. Zhang, I. Goshen, D.-S. Kim, L. E. Fenno, C. Ramakrishnan, and K. Deisseroth. Global and local fMRI signals driven by neurons defined optogenetically by type and wiring. *Nature*, 465(7299):788–792, 2010. ISSN 1476-4687. doi: 10.1038/nature09108. URL `https://doi.org/10.1038/nature09108`.

[71] A. Fleischmann, B. M. Shykind, D. L. Sosulski, K. M. Franks, M. E. Glinka, D. F. Mei, Y. Sun, J. Kirkland, M. Mendelsohn, M. W. Albers, and R. Axel. Mice with a "Monoclonal Nose": Perturbations in an Olfactory Map Impair Odor Discrimination. *Neuron*, 60(6):1068–1081, 12 2008. ISSN 08966273. doi: 10.1016/j.neuron.2008.10.046.

[72] V. S. Sohal, F. Zhang, O. Yizhar, and K. Deisseroth. Parvalbumin neurons and gamma rhythms enhance cortical circuit performance. *Nature*, 459(7247):698–702, 6 2009. ISSN 00280836. doi: 10.1038/nature07991.

[73] J. T. Paz, T. J. Davidson, E. S. Frechette, B. Delord, I. Parada, K. Peng, K. Deisseroth, and J. R. Huguenard. Closed-loop optogenetic control of thalamus as a tool for interrupting seizures after cortical injury. *Nature Neuroscience*, 16(1):64–70, 1 2013. ISSN 10976256. doi: 10.1038/nn.3269.

[74] E. Krook-Magnuson, G. G. Szabo, C. Armstrong, M. Oijala, and I. Soltesz. Cerebellar Directed Optogenetic Intervention Inhibits Spontaneous Hippocampal Seizures in a Mouse Model of Temporal Lobe Epilepsy. *eNeuro*, 1(1), 11 2014. ISSN 2373-2822. doi: 10.1523/ENEURO.0005-14.2014. URL `http://eneuro.org/cgi/doi/10.1523/ENEURO.0005-14.2014`.

[75] E. Krook-Magnuson, C. Armstrong, A. Bui, S. Lew, M. Oijala, and I. Soltesz. In vivo evaluation of the dentate gate theory in epilepsy. *Journal of Physiology*, 593(10):2379–2388, 5 2015. ISSN 14697793. doi: 10.1113/JP270056.

[76] J. H. Siegle and M. A. Wilson. Enhancement of encoding and retrieval functions through theta phase-specific manipulation of hippocampus. *eLife*, 3, 7 2014. doi: 10.7554/elife.03061.

[77] E. Stark, L. Roux, R. Eichler, Y. Senzai, S. Royer, and G. Buzsáki. Pyramidal cell-interneuron interactions underlie hippocampal ripple oscillations. *Neuron*, 83(2):467–480, 7 2014. ISSN 10974199. doi: 10.1016/j.neuron.2014.06.023.

[78] D. H. O'Connor, S. A. Hires, Z. V. Guo, N. Li, J. Yu, Q. Q. Sun, D. Huber, and K. Svoboda. Neural coding during active somatosensation revealed using illusory touch. *Nature Neuroscience*, 16(7):958–965, 7 2013. ISSN 10976256. doi: 10.1038/nn.3419.

[79] L. Grosenick, J. H. Marshel, and K. Deisseroth. Closed-Loop and Activity-Guided Optogenetic Control. Technical report.

[80] Feedback systems: an introduction for scientists and engineers. *Choice Reviews Online*, 46(04):46–2107, 1 2013. ISSN 0009-4978. doi: 10.5860/choice.46-2107.

[81] Y. Katz, O. Yizhar, J. Staiger, and I. Lampl. *Optopatcher—An electrode holder for simultaneous intracellular patch-clamp recording and optical manipulation*, volume 214. 1 2013. doi: 10.1016/j.jneumeth.2013.01.017.

[82] H. Cao, L. Gu, S. K. Mohanty, and J. C. Chiao. An integrated ??IED optrode for optogenetic stimulation and electrical recording. *IEEE Transactions on Biomedical Engineering*, 60(1):225–229, 2013. ISSN 00189294. doi: 10.1109/TBME.2012.2217395.

[83] J. Fraytag, M. F. Da Silva, N. B. Chagas, R. N. Do Prado, and M. A. Costa. Lighting systems energy efficiency based on different human visual conditions. In *2010 9th IEEE/IAS International Conference on Industry Applications, INDUSCON 2010*, 2010. ISBN 9781424480104. doi: 10.1109/INDUSCON.2010.5739986.

[84] Y. Zeng, D. Qiu, X. Meng, B. Zhang, and S. C. Tang. Optimized design of coils for wireless power transfer in implanted medical devices. *IEEE Journal of Electromagnetics, RF and Microwaves in Medicine and Biology*, 2 (4):277–285, 12 2018. ISSN 24697249. doi: 10.1109/JERM.2018.2863955.

[85] B. H. Waters, B. J. Mahoney, G. Lee, and J. R. Smith. Optimal coil size ratios for wireless power transfer applications. In *Proceedings - IEEE International Symposium on Circuits and Systems*, pages 2045–2048. Institute of Electrical and Electronics Engineers Inc., 2014. ISBN 9781479934324. doi: 10.1109/ISCAS.2014.6865567.

[86] Polyplus. Polyplus-transfection S.A. - Bioparc - 850 Bd S. Brant - 67400 Illkirch - France Polyplus-transfection Inc. - 1251 Ave of the Americas - 34th fl. - New-York - NY 10020 - USA www.polyplus-transfection.com jetPRIME® in vitro DNA & siRNA transfection reagent PROTOCOL.

[87] J. Schindelin, I. Arganda-Carreras, E. Frise, V. Kaynig, M. Longair, T. Pietzsch, S. Preibisch, C. Rueden, S. Saalfeld, B. Schmid, J.-Y. Tinevez, D. J. White, V. Hartenstein, K. Eliceiri, P. Tomancak, and A. Cardona. Fiji: an open-source platform for biological-image analysis. *Nature Methods*, 9(7):676–682, 2012. ISSN 1548-7105. doi: 10.1038/nmeth.2019. URL `https://doi.org/10.1038/nmeth.2019`.

[88] K. Ogata. *Discrete-time Control Systems (2Nd Ed.)*. Prentice-Hall, Inc., Upper Saddle River, NJ, USA, 1995. ISBN 0-13-034281-5.

[89] K. P. Burnham and D. Anderson. Model Selection and Multimodel Inference: A Practical Information-theoretic Approach. Technical report.

[90] Institute of Electrical and Electronics Engineers and IEEE Circuits and Systems Society. *Circuits and Systems (ISCAS), 2014 IEEE International Symposium on : Date 1-5 June 2014 : [Melbourne, Australia]*. ISBN 9781479934324.

[91] U.-M. Jow and M. Ghovanloo. Design and Optimization of Printed Spiral Coils for Efficient Transcutaneous Inductive Power Transmission. *IEEE Transactions on Biomedical Circuits and Systems*, 1(3):193–202, 9 2007. ISSN 1932-4545. doi: 10.1109/TBCAS.2007.913130. URL `http://ieeexplore.ieee.org/document/4432391/`.

[92] M. W. Baker and R. Sarpeshkar. Feedback analysis and design of RF power links for low-power bionic systems. *IEEE Transactions on Biomedical Circuits and Systems*, 1(1):28–38, 3 2007. ISSN 19324545. doi: 10.1109/TBCAS.2007.893180.

[93] F. Jolani, J. Mehta, Y. Yu, and Z. David Chen. Design of wireless power transfer systems using magnetic resonance coupling for implantable medical devices. *Progress in Electromagnetics Research Letters*, 40:141–151, 2013. ISSN 19376480. doi: 10.2528/PIERL13020509.

[94] J. S. Wiegert, M. Mahn, M. Prigge, Y. Printz, and O. Yizhar. Silencing Neurons: Tools, Applications, and Experimental Constraints, 8 2017. ISSN 10974199.

Appendix A

Model Structure Analysis for Cell System Identification

As stated in section 4.2, ARX(2,1,1) model structure was tested in each of the remaining cells to be analyzed. Apart from cell 3, an ARX(2,1,1) model was constructed for each cell using *Matlab*'s System Identification Toolbox, as down previously with cell 3. The following figure illustrates the error auto-correlation for each cell as well as a comparison of the cell response to a 5 minutes step input to the respective model.

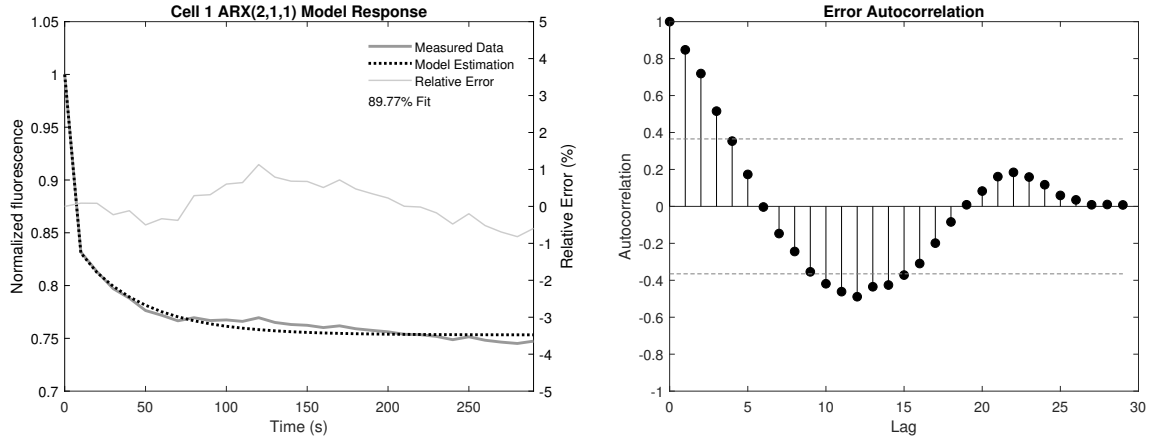

Figure A.1: ARX(2,1,1) model structure applicability analysis to cell 1.

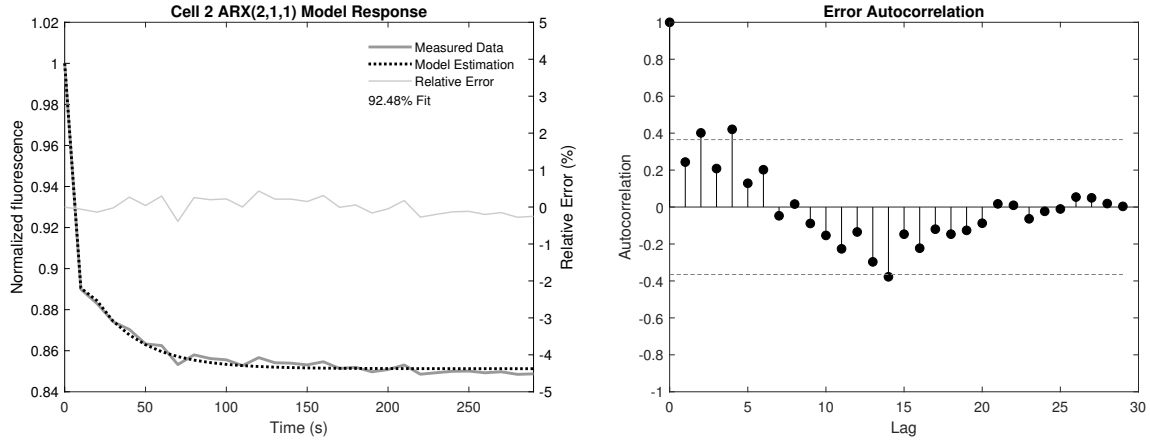

Figure A.2: ARX(2,1,1) model structure applicability analysis to cell 2.

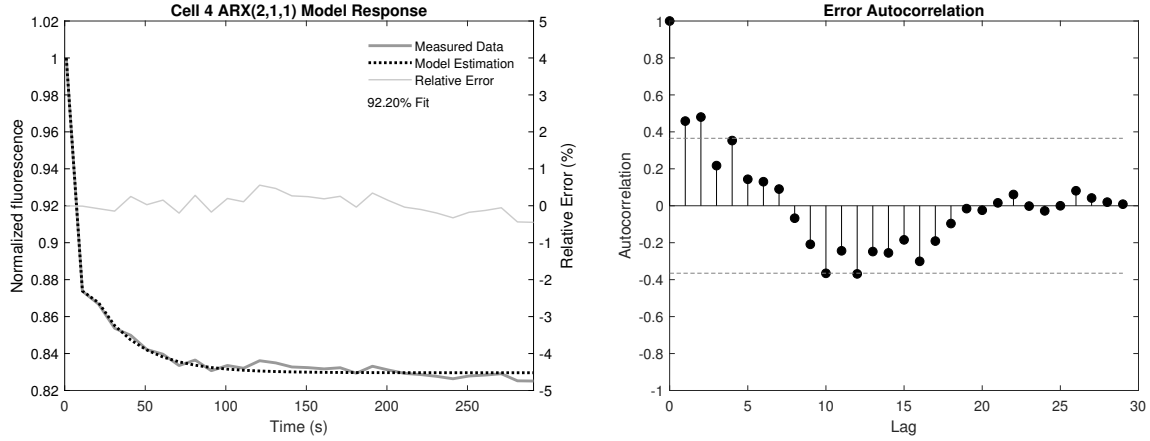

Figure A.3: ARX(2,1,1) model structure applicability analysis to cell 4.

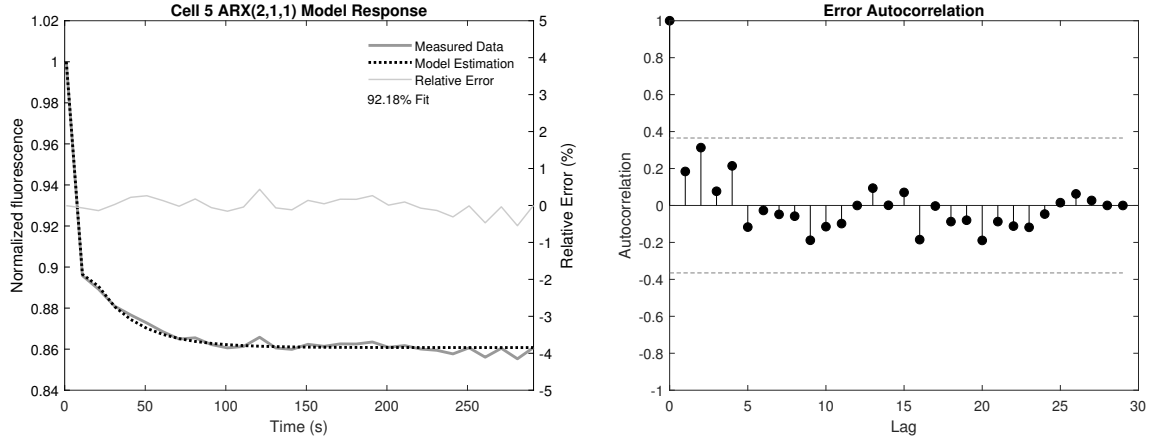

Figure A.4: ARX(2,1,1) model structure applicability analysis to cell 5.

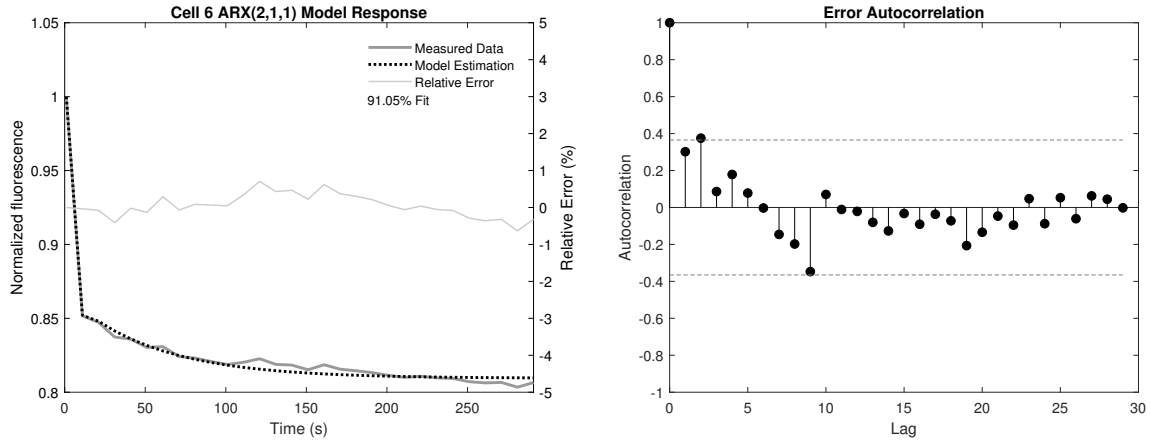

Figure A.5: ARX(2,1,1) model structure applicability analysis to cell 6.

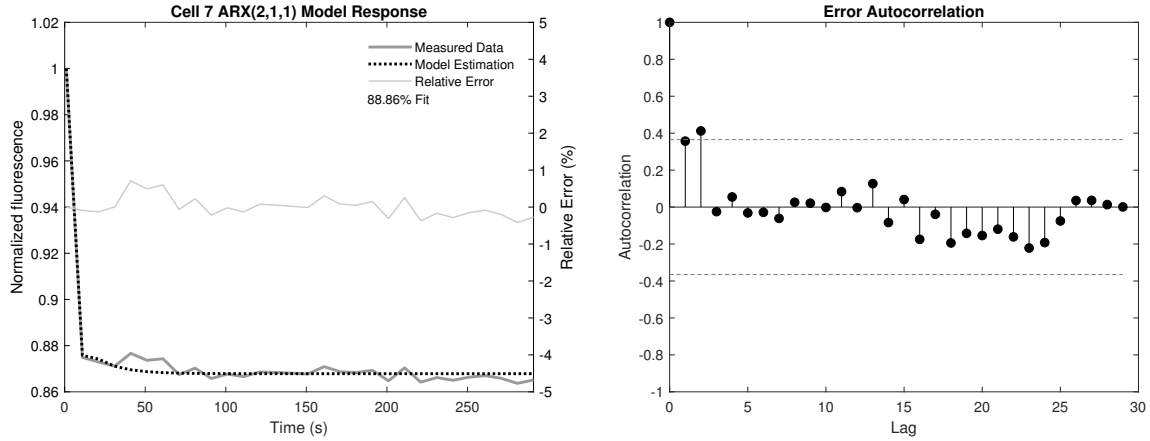

Figure A.6: ARX(2,1,1) model structure applicability analysis to cell 7.

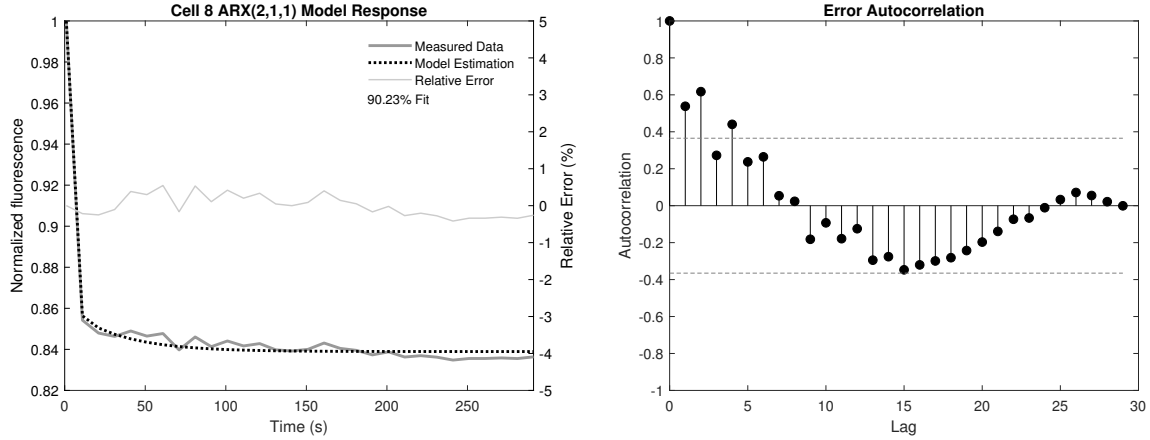

Figure A.7: ARX(2,1,1) model structure applicability analysis to cell 8.